Polarization Manipulation in Silicon Photonics

by

Zhan Su

Submitted to the Department of Electrical Engineering and Computer Science
in partial fulfillment of the requirements for the degree of

Master of Science in Computer Science and Engineering

at the

MASSACHUSETTS INSTITUTE OF TECHNOLOGY

September 2013

Author ....
Department of Electrical Engineering and Computer Science
August 22, 2013

Certified by........................
Michael R. Watts
Associate Professor
Thesis Supervisor

Accepted by ....
Leslie A. Kolodziejski
Chairman, Department Committee on Graduate Theses

Polarization Manipulation in Silicon Photonics

by

Zhan Su

Submitted to the Department of Electrical Engineering and Computer Science
on August 22, 2013, in partial fulfillment of the
requirements for the degree of
Master of Science in Computer Science and Engineering

Abstract

Silicon photonics is moving fast toward industrialization. It satisfies the increasing demand for higher speed, larger bandwidth communication. Thus it has a wide range of applications including high-performance computing, data center, telecom etc.. However, the on-chip (waveguide) and off-chip (fiber) components for silicon photonics have quite different characteristics for the polarizations of light. The polarization dependence of on-chip silicon photonics components still remains a bottleneck for the real application of it. Efficient devices for manipulating polarizations are highly demanded.

Herein, we present the designs of adiabatic polarization rotator (PR) and polarization splitter and rotator (PSR) to deal with this issue. With their adiabatic nature, larger bandwidth (>100 nm) and better fabrication tolerance have been achieved.

Besides, the effort toward the realization of a full-functional two-input two-output PBS, which is an exact correspondent of the traditional cube PBS in free space is presented. The structure was fabricated in a commercial state-of-art CMOS foundry and has a bandwidth of over 150 nm and less than -10dB crosstalk level. Though its application in traditional communication can be replaced by PS, PR or PSR, its application in more accurate systems such as polarization-entangled states generation and manipulation in quantum optics or on-chip heterodyne interferometers.

Moreover, original compact-ring resonator based even-dropping optical bus system is proposed and analyzed in detail. Large free-spectral range offered by small radius micro-ring gives more communication channels to fully utilize the power of wavelength division multiplexing (WDM). Furthermore, a multi-channel WDM broadcasting system is proposed using the optical bus design. We have demonstrated a two-channel broadcasting system, which can be further increased to more than 16 channels.

Thesis Supervisor: Michael R. Watts
Title: Associate Professor

Acknowledgments

This work can never be done without the help of those people around me.

The first person I want to thank is my advisor, Professor Michael Watts. He is always nice to me and guiding me to the right way of doing research. The first time I saw him was during the time I was looking for a research advisor. At that time, I almost knew nothing about silicon photonics. But Mike did not turn back on me, instead he got me involved in the group activity and exposed me to those interesting projects he had, giving me the freedom to decide what I want to do. The first project I worked on was a thermal photon detector. After several months of trial, I found myself not interested in that project. I told Mike about changing project and felt really sorry for my incompetence. However, Mike did not blame me for this. On contrary, he found out my potential in doing simulations and rigorous designs and let me handle some new idea following up his PHD thesis. This is the topic what I will talk about over this thesis. Talking with him about research is always helpful. His unique insight and great experience can always solve my problems in a quick manner.

Secondly, I want to thank Erman Timurdogan for his considerate help on almost every part of my life. In research part, he is a good co-worker and has a great intuition in getting new ideas. Through talking with him over coffee break, I gradually start changing from a dumb to a guy who has his own ideas about research. The simulation methods, the experimental skill and the guidance he gave me on research are becoming part of my life resources. Life is not easy for PHD student. Everyone has his temper and his down time. Every time I am in bad mood, Erman will be the man who helps me figure out the problem inside of my mind and gives me the solution to deal with it. I feel really grateful to have an officemate and friend like him. Without him, I might have to take a long roundabout course before getting used to the PHD life at MIT.

Dr. Jie Sun is another guy I want to thank. We are both Chinese students in this group. It was him who first recommended me to Mike to join this group. He helped me understand the uniqueness of our group and choose the right way when facing choices. During those days when I could not figure out the source of loss on my device, Jie was the guy who helped me take the SEM picture and analyze the device. It is always helpful to talk with him and I always get the answer that I want.

It is great to be a member of photonic microsystems group in MIT and to be the officemate of Dr. Aleksander (Sasha) Biberman, Dr. Michele Moresco. I am really grateful to their patience in teaching me the experiment skills. It was Sasha who helped me start the designs on optical switches and Michele who got me into the optical bus designs. I also enjoyed those time spent with Ami Yaacobi, Brad G. Cordova, Cheryl Sorace-Agaskar, David B. Cole and Christos Samolis on mode solver design and FDTD simulations. Thank Dr. Ehsan S. Hosseini and Purnawirman for helping me understand the design of on-chip laser structures. Besides, I want to thank Dr. Jonathan D. B. Bradley for his trust in having me involved in his great work. He is always nice and reliable. Hope he will enjoy his professorship in Canada.

Apart from our own group, Duo Li and Hung-Wen Chen from Professor Franz Kärtner's group also helped me a lot in terms of building up new setups. They are always nice and patient no matter how many times I have bugged them. The equipment I borrowed from them greatly helped my experiment. At last, I want to give thanks to my friends Huaiyu Meng and Tao Yu for their great help in simulation tools and SEM imaging. They are fantastic researchers who always stimulate me to move on.

Contents

List of Figures

List of Tables

Chapter 1

Introduction

Optics have long been used as a measurement tool for basic science. Lens, gratings have been widely used in imaging field. In early 1800s, double-slit experiment revealed the interference property of light to the world, which opened a new era for utilizing light for extremely accurate experiments such as Michelson-Morley experiment. Later on, optics found its application in medical imaging such as X-ray imaging [1], optical coherence tomography (OCT) [2]. However, in data communication and processing field, the electronics dominate in a way that it can benefit from the very large scale integration (VLSI) technique. Optics, to some degree, was put aside due to its cumbersome size and less reliability in carrying the signal (optical propagation loss) and lack of techniques on amplifying the optical signal before the emergence of optical fiber. Optical fiber came out as a loss-less system ($<$ 20dB/km). The rise of optical fiber showed the powerful ability on carrying signal with ultra-high reliability over long distance and proved it to be a much better information channel compared to traditional copper based channel. However lacking of direct optical amplifier made it annoying that signals need to be transformed to electrical signals, amplified and changed back to optical signals for every 100 km. Especially for cross-ocean communication, building thousands of relay stations would make a lot of troubles. The invention of Erbium Doped Fiber Amplifier [3] bridged the gap and achieved the direct amplification of optical signal. Thus far, optical fibers almost replaced all copper wires in the long-distance communication. However, for short distance communication, copper wires still find its position in low speed communications. But, as the demand of speed and capacity of the communication lines and links increase wildly over recent years, metal wires start suffering from the communication cost due to their poor high speed performance [4]. Thus new technologies for solving this bottleneck need to come up.

1.1 Development of CMOS technology

Invented 50 years ago, CMOS technology has immersed into almost every field of our daily life. Computer, cellphone, television etc. have been upgraded from their cumbersome prototypes to thin and elegant new versions with the pace of CMOS technology. The number of transistors integrated on chip is being doubled every two years following the famous Moore's Law [5]. Taking Intel corporation for example, the CPU development of Intel is shown in Fig. 1-1. The trend shows a saturation of the clock speed around year 2004. And after that, multi-core architecture started to rule the CPU world.

The main issue with the increase of the clock speed comes from power consumption and cooling method available. According to International Technology Roadmap for Semiconductors (ITRS), the power which current affordable cooling method can dissipated is around 260 W on chip level[1]. If the clock speed keeps on scaling like what happened during 1990-2000, it will arrive at more than 10GHz which will lead to huge amount of power consumption and instability of the CPU performance due to current leakage. Fig. 1-2 shows the data I extracted from ITRS reports on the prediction on the clock speed. It is apparent that the newest prediction now is modified to a pretty slow pace compared to the guess made during 2008.

After clock speed got saturated around 4GHz, the CPU architecture started moving to multi-core directions. The number of transistors on chip still follows its pace according to Moore's law. The boost of performance for the computer now mainly comes from parallel computing (including hyperthreading and multi-core manage-

---

[1] See http://www.itrs.net/Links/2012ITRS/Home2012.htm

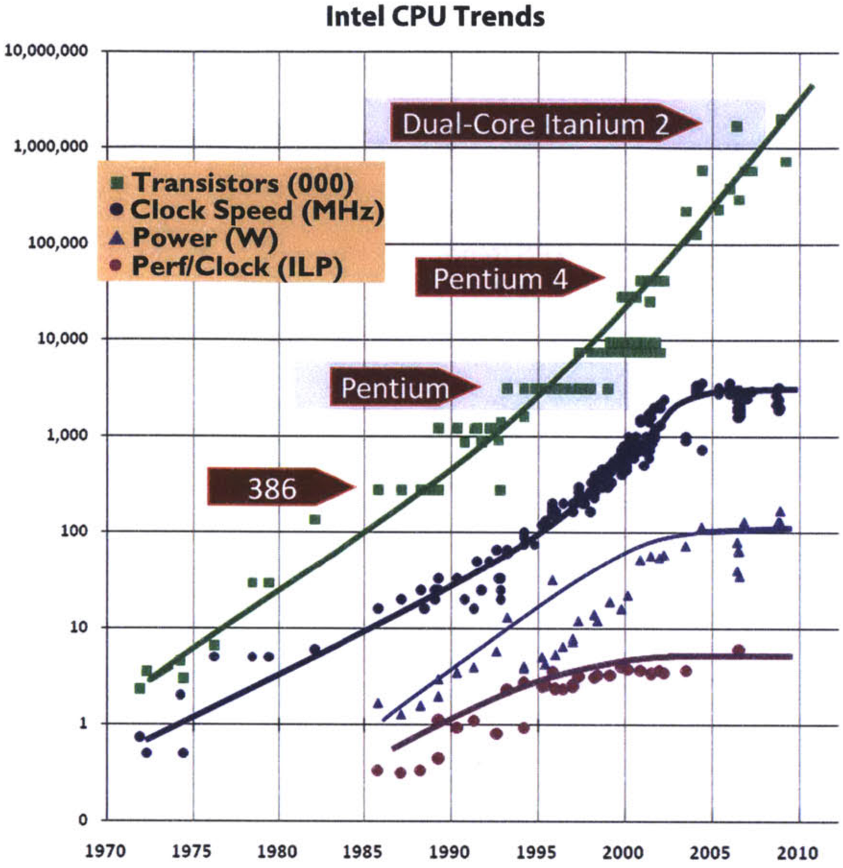

Figure 1-1: The CPU development trend of Intel corporation[2].

ment) and SRAM or cache on chip. In terms of speed, CPU is far faster than other components of a computing system. During a computation process, the speed between data communication between CPU and memory slow down the overall speed of CPU because CPU needs to wait for memories to feed data to it. By bridging the gap with cache which is closer to CPU and faster than memories and expanding size of it, the computer can thus gain better performance. For example, 80486DX issued by Intel in 1989 has only Level 1 (L1) cache of 8KB on chip. But when Pentium Pro was issued in 1995, it already had 16KB L1 cache and 256KB L2 cache. At present, CPUs like quad-core i7 using Ivy Bridge technology issued in 2012 have 64KB L1 cache and 256KB L2 cache per core and 8MB shared L3 cache. However, cache is relatively

---

[2] http://www.gotw.ca/publications/concurrency-ddj.htm

expensive compared to memory or DRAM. And since it shares the size of the CPU chip, it cannot be too large to limit the area of available logic gate components.

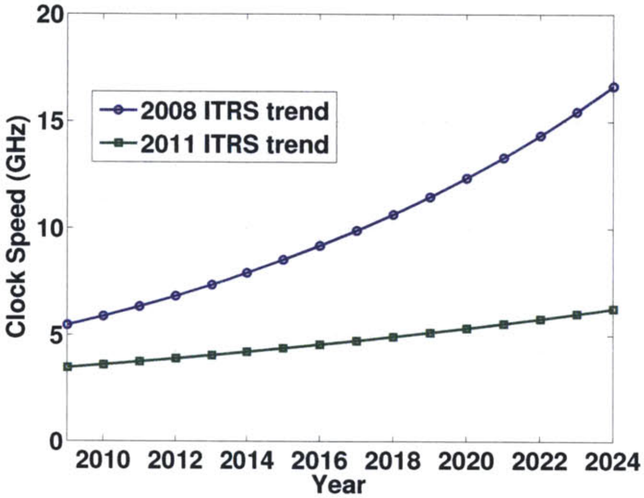

Figure 1-2: Clock speed prediction for year 2008 and year 2011 from ITRS Roadmap 2012.

Parallel computing on boosting the overall performance of computer is another hot topic. It is usually used for large-scale computing, where the tasks can be separated into multiple threads to multiple cores. Each core runs its own process with little data shared among the cores. In this way, as long as the communication traffic between multiple cores is not the limiting factor, the overall performance can be boosted. However, for single thread process normally used in daily life, it gains little benefit from parallel computing.

1.2 Problems and Solutions

The greatness of CMOS technology gives us the power to manipulate large amount of data within short time. But at the same time, the demand for faster access to information and larger computation capacity has never ended. Technology, in itself, cannot follow a pace all the time for upgrade if nothing new enters the technology. As shown in Fig. 1-3, since the invention of CMOS technology, the demand for network

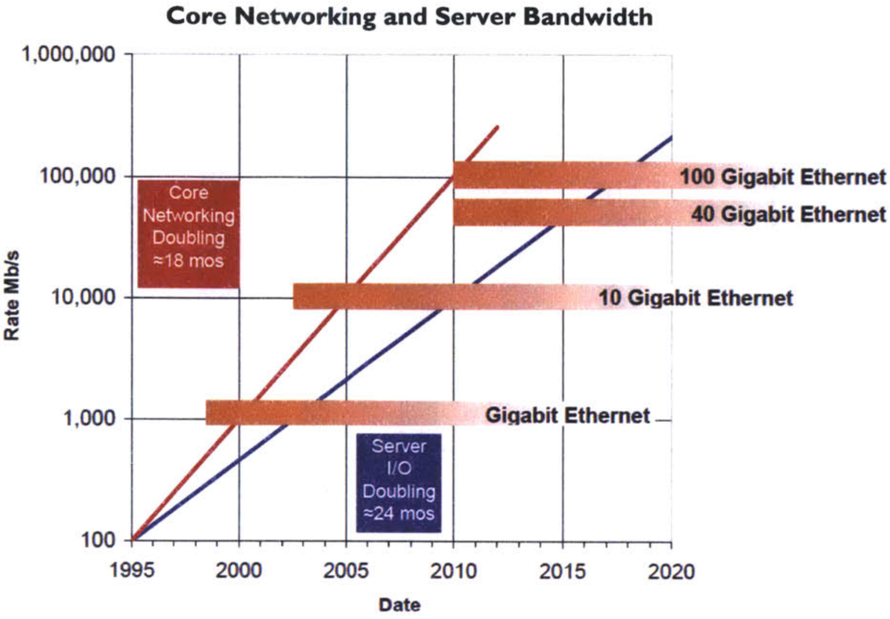

Figure 1-3: The trend of bandwidth of core network and server I/O[3].

bandwidth is increasing at an astonishing speed, with demand doubled every 18 month while the server capacity available to deal with the information is doubled every 2 years. The gap between the network demand and the server would become larger and larger over the time according to prediction. New methods to boost the capacity of server need to come up.

Besides, the data storage is increasing at an even higher speed. Large amount of data needs to be taken care of. The hard disk drive (HDD) storage capacity trend is shown in Fig. 1-4. The speed of increase of the storage is tremendous in this era, where accessing and sharing data are important to people at any time and anywhere. Correspondingly, large amount of computing power is needed to handle the creation and searching tasks for certain data and huge bandwidth need to be devoted to uploading and downloading data.

Before solving the bottleneck between the inequality between server capability and ethernet bandwidth demand and the fast scaling of data storage, another problem needs to be first solved. The speed of CPU is moving on its regular path. However,

---

[3] http://www.theregister.co.uk/2011/10/10/network_architecture

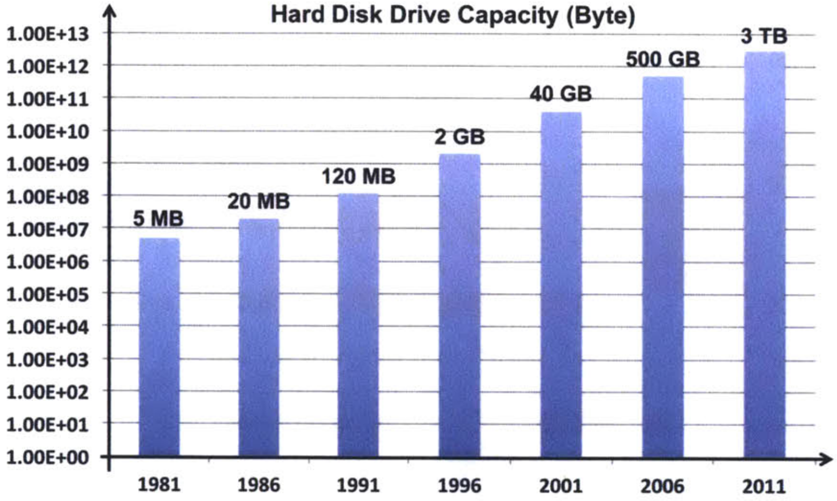

Figure 1-4: The trend for the capacity of hard disk drive (HDD) over years[4].

the increase of speed of memory (every 10 years) is far lower than the pace of CPU (every 18 months). (shown in Fig. 1-5). Though, we now have cache as a bridge between memory and CPU, its size is limited by the size the chip. Nowadays, a huge amount of power (20%) has been devoted to different kind of communication such as on-/off-chip, namely chip-to-chip communication, chip-to-memory communication and memory-to-memory communication. And the overall performance is dragged down by the interconnect bottleneck, termed as "Memory wall" by Wulf and McKee in 1995 [6]. The situation is getting worse and worse over the time.

The bottleneck of the speed comes from the bus speed limitation between the memory and CPU. Since memory chip and CPU chip are separate chips, the resistance and capacitance associated with the bus set a limit for the speed achievable along the bus. To solve this bottleneck, the 3D integration method comes as a solution. It includes using ball grid array (BGA) (Fig. 1-6(a)) and through-silicon-VIA (TSV) technique (shown in Fig. 1-6(b)).

BGA is a type of surface-mount packaging for integrated circuits. It has the advantage of low cost, excellent electrical and thermal properties and minimal size.

---

[4] http://arstechnica.com/business/2011/09/information-explosion-how-rapidly-expanding-storage-spurs-innovation/

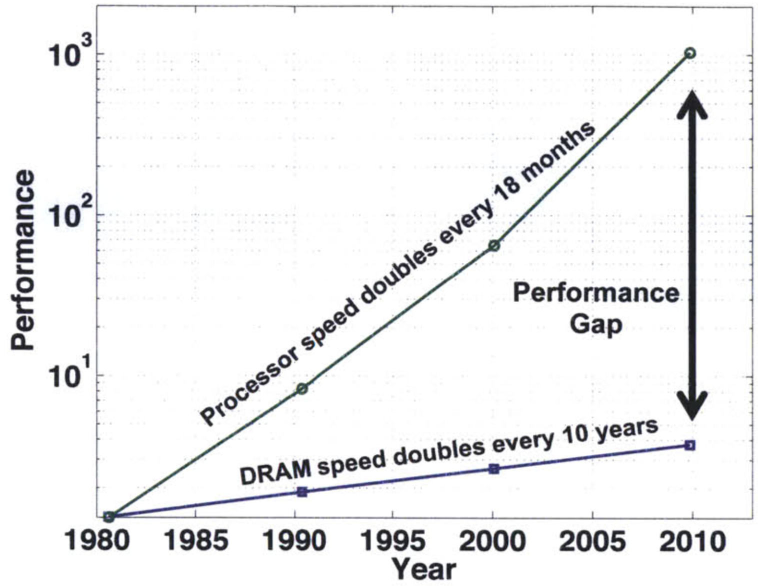

Figure 1-5: The trend of CPU performance and memory performance. The CPU shows a performance doubling every 18 months while memory shows a doubling of every ten year[5].

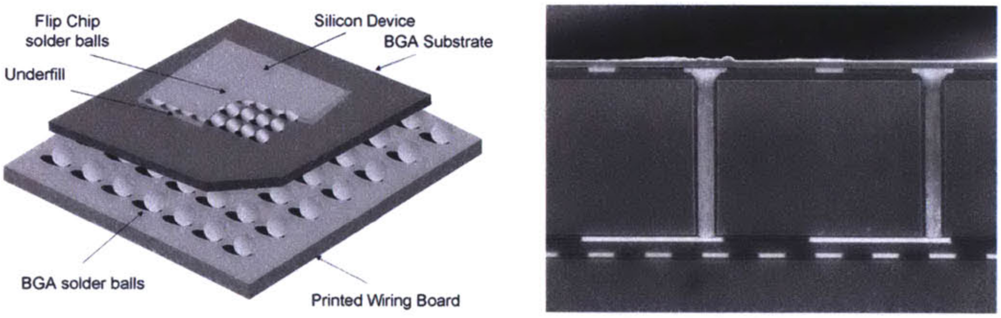

(a) (b)

Figure 1-6: (a) Ball grid array (BGA)[6]. (b) Through-silicon-VIA (TSV)[7].

Since it utilizes the surface of the chip instead of the periphery of the chip, more spaces for interconnect routing are created. For TSV, two methods are proposed as possible solution. The first is combining DRAM to CPU through wafer bonding by

---

[5] http://www.getfilings.com/sec-filings/100202/MoSys-Inc_8-K/a6163828ex99_2.htm#b

[6] http://www.thomasnet.com/articles/custom-manufacturing-fabricating/pcb-ball-grid-arrays

[7] http://javier.esilicon.com/2011/01/30/thru-silicon-vias-current-state-of-the-technology/

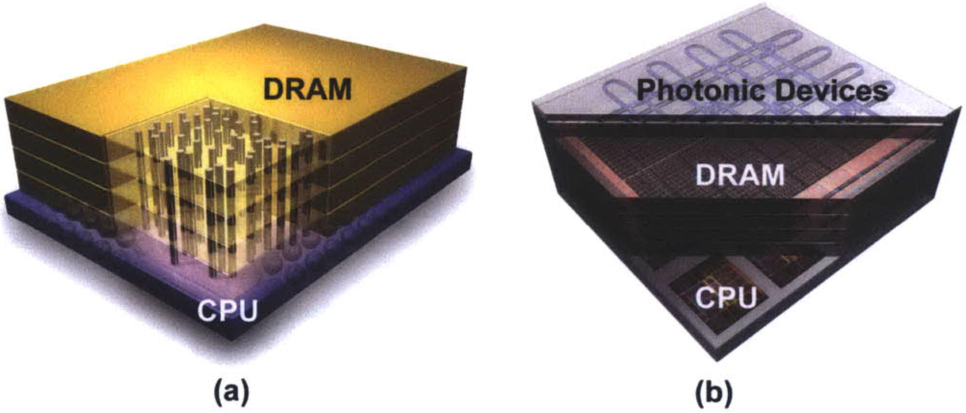

Figure 1-7: (a) CPU and DRAM integrated with TSV[8]. (b) CPU, DRAM and photonic devices integrated by TSV[9].

TSV (shown in Fig. 1-7(a)). The second is using silicon photonics method (shown in Fig. 1-7(b), including integrated silicon photonic devices to handle the interconnect. However, there are still some issues to be solved for TSV such as heat dissipation and threshold voltage shift of the MOSFET.

In current data center, vertical-cavity surface-emitting lasers (VCSELs) are widely used for high speed data transmission for on-/off-chip communication. But it, in itself, is not a scalable method and each of the VCSELs can only carry one wavelength. For example, assuming the relation between floating-point operation per second (FLOPs) and memory communication speed as bit per second (bit/s) is 1.6 bit/FLOP, for achieving a goal of 20 TFLOPs on a single microprocessor, 640 VCSELs of which each carries a signal of 50Gb/s are required. However, by using silicon photonics WDM system in C and L communication band, around 75 wavelength channels can be used simultaneously. Since the silicon photonics modulator is possible to achieve speed more than 50Gb/s, the number of output channels to couple out of the chip will be greatly reduced by an order of 2.

---

[8] http://www-03.ibm.com/press/us/en/pressrelease/36125.wss

[9] http://lightwave.ee.columbia.edu/?s=research&p=multi-processor_interconnection_networks

1.3 Motivations for Silicon Photonics

To take full advantage of wavelength division multiplexing (WDM), silicon photonics arises as an alternative to solve the short distance communication bottleneck. The waveguide structures can be regarded as a minimized fiber, with the capacity to carry high speed data rate up to 1.28Tb/s [7] (consist of 32 wavelengths with 40Gbit/s) while keep the loss negligible. Compared to III-V materials which are generally used in traditional communication systems, silicon has the advantages of high refractive index which makes devices smaller in size and compatibility with current CMOS process. From the view point of industry, it will cost too much to build a totally new system devoted to photonics. Besides, with the compatibility with state-of-art CMOS process, the integration of silicon CMOS technology and silicon on-chip photonics technology will open a new era for large-scale computation, data center etc. However, unlike III-V materials which are easier to make a laser, silicon is, in itself, an indirect band gap material which makes it hard to lase. Though several works has shown the demonstration of the silicon Raman laser [8, 9], the low efficiency and less of tenability of wavelength make it impractical for a real product. Recently, big achievements have been achieved on other silicon compatible materials such as stressed germanium based structure [10], erbium doped Al_2O_3 glass structures [11, 12]. With the help of silicon photonics, huge amount of fibers inside the data center for core-to-core, core-to-memory and memory-to-memory communications can be saved which can reduce a lot of the management cost. Besides, integrated photonics will also benefit from the large amount of demands which will lower its cost to be acceptable like the history which happened to VLSI CMOS years ago. Currently, both industry and academia research groups have devoted a significant effort to the development of silicon photonics. Fig. 1-8 shows the current research distributions in the field of silicon photonics.

The future of silicon photonics industry is predicted in Fig. 1-9. Nowadays, the business mainly focuses on high performance computing, data center and military and scientific research. There are some products such as Kotura high speed modulator

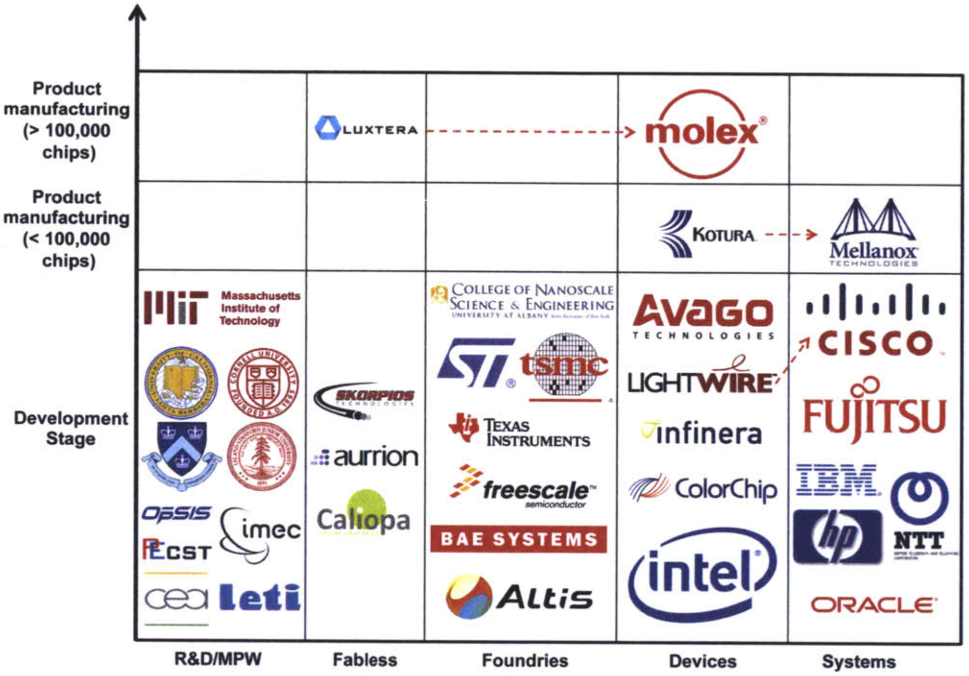

Figure 1-8: The research efforts of silicon photonics in both industry and academia. This figure is regenerated from online figure[11] and updated with current data.

module[10]. Further extension of silicon photonics will go to the areas of telecom when the cost and energy consumption become more interesting to telecom carriers. Besides, the compactness of silicon photonic active devices has the potential to combine structures such as interferometers on chip, which may open a whole new area in medical instrument implementation. The last stage of silicon photonics which has the largest market is the board-to-board, chip-to-chip communication. CMOS technology totally changed the way we live in this world. Silicon photonics, while still in its infant stage, may make another huge upgrade to the current CMOS technology.

However promising, silicon photonics suffers from the chip thickness and thermal distribution variation on chip [13]. This imposes a big problem for achieving low power device because part of the power needs to be used for thermal tuning which contributes to the total power consumption of the device. This can be potentially solved by the automatic wavelength recovery on chip [14].

---

[10] See http://www.kotura.com/products-apps/index.html

[11] http://www.semiconductor-today.com/news_items/2012/SEP/YOLE_270912.html

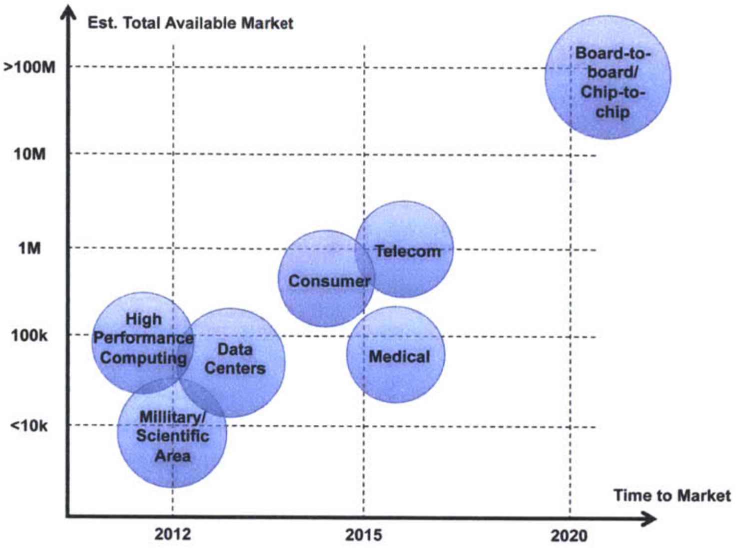

Figure 1-9: The prediction of the future areas and its associated market value of silicon photonics industry^{11}.

1.4 Components of Silicon Photonics

To build a computing or communication system using silicon photonics, several components need to be demonstrated. A list of fiber communication components and their corresponding on-chip components of silicon photonics is shown in Fig. 1-10. It consists of communication channel, modulator [15], isolator [16], detector [17], delay line [18], filter [19], laser [11], polarization rotator (PR) [20], polarization splitter (PS) [21], wavelength division multiplexer (WDM) [22], polarizer [23] and power splitter [24]. Most of the structures listed here are single devices that have been demonstrated to have relatively similar performance to that of the fiber-based correspondents. The compactness of the waveguide structure is definitely the biggest advantage compared to fiber optics. Besides, the capacity to carry large amount of data through the structure makes it a suitable platform for interconnect. With the progress of on-chip lasers (source) and high speed modulators (signal generation), a compact and complete on-chip interconnect system is ready to go.

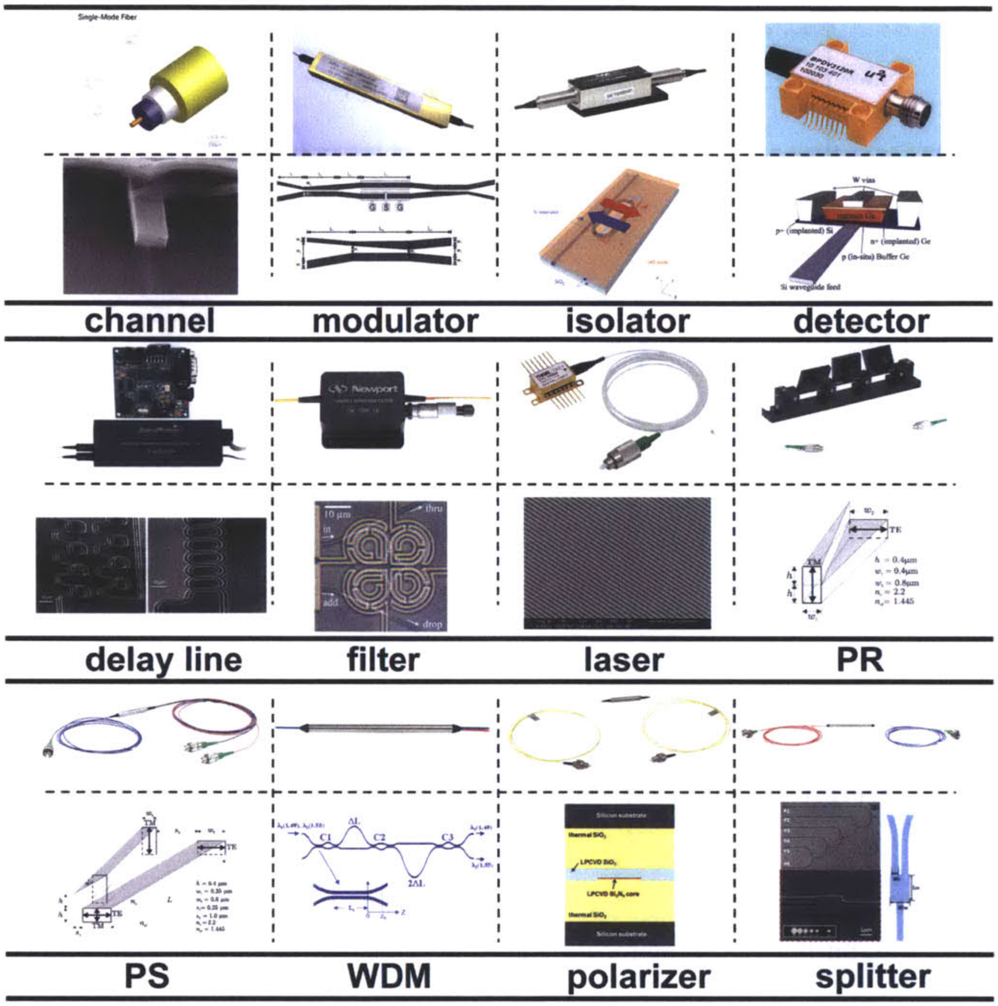

Figure 1-10: List of fiber communication components and their correspondents in on-chip silicon photonics. The top part of each row is the fiber based structure while the bottom part is the integrated photonic correspondent. *Image sources are mentioned in the main text.*

1.5 Demand for Handling Polarization of Light On-Chip

For traditional long distance signal transmission, the polarization of the light inside the fiber is not used and does not need to be dealt with specifically. The polarization is not fixed and the output light is randomly polarized. This will not harm the quality of the signal. However, on-chip silicon photonics use high index materials such as silicon and Si_3N_4 for guiding light and the rectangular shape is normally used for waveguide structure. This will generate a large birefringence for TE and TM modes. In this case, the two polarizations of light will behave quite differently and will not couple to each other if the symmetry of the structure is not broken. The difference in polarization behaviors between fiber and waveguide requires further polarization control on chip, namely separating, combining and rotating the polarization. Besides, polarizations of light provide us with another degree of freedom for doubling the data rate for transmission. Traditional techniques such as dual-polarization modulation can be used to make full use of the transmission channel. Though most on-chip polarization manipulation devices such as polarization rotators (PRs), polarization splitters (PSs) and polarization splitter and rotators (PSRs) have been demonstrated, there are still more spaces for improvements such as fabrication tolerance, bandwidth. Besides, silicon photonics can also be a promising platform for on-chip quantum information processing (QIP). This, in turn, requires structures such as polarization beam splitter (PBS) as a basic component for generating polarization entangled states. Among all the "PBS" demonstrated so far, none of them are true PBS which requires two inputs and two outputs. Thus, one of the tasks of this thesis is on realizing this device in silicon platform. The main topic of this thesis is on polarization manipulation for on-chip silicon photonics, addressing the problem with thickness and thermal variations and trying to present a reliable way to design insensitive device under those variations. Apart from the traditional communication benefits, on-chip quantum computing is gaining more and more attention with the possibility to integrate entangled photon source on-chip and different kinds of on-chip optical devices available for quantum state manipulation. This is an interesting topic which may benefit from the development of silicon photonics.

1.6 Summary

In this chapter, a brief introduction of the development of CMOS technology and its bottlenecks are presented. Different methods on dealing with the problems are discussed. Among them, silicon photonics is given as new and promising method. The current status of silicon photonics is discussed and polarization issues for on-chip device is further analyzed.

Chapter 2

Polarization Rotator (PR) and Polarization Splitter and Rotator (PSR)

For on-chip rectangular waveguide, two polarization modes (transverse electric (TE) and transverse magnetic (TM)) exist at the same time. Since TE and TM modes have quite different properties, to achieve a polarization independent photonic circuits, an efficient way to split and rotate the polarization of the modes need to be implemented. In this section, I will focus on the design techniques on PR and PSR. Though, most of the structures proposed in this chapter have not been fabricated, the Eigen Mode Expansion (EME) and FDTD simulations are sufficient to show the robustness of those designs.

2.1 Background

Since most of the structures in silicon photonics, for example, on-chip lasers [12], modulators [25], filters [26] requires a certain polarization, to deal with the variety of the input polarizations, TE and TM modes should be separated and one of the polarization needs to be rotated to another polarization to ensure identical processing. The splitting of the TE and TM modes can be achieved by using polarization splitters (PSs). The rotation of the waveguide mode polarization can be achieved by using polarization rotators (PRs). Since advanced CMOS nodes are continuously shrinking the height of the active silicon layer in order to satisfy Moores law scaling in computation capacity, which in turn favors high-confinement wide and thin waveguide cross-section and TE mode, an efficient way to transform TM mode to TE mode becomes highly demanded. In this chapter, I will focus mainly on using TE modes as the output after polarization manipulation. Sometimes, both polarizations need to be manipulated simultaneously. In that case, instead of using a PS followed by PR in the TM port, simple design that combines these two functions together is proposed (polarization splitter and rotator), leading to a smaller footprint for the device.

In terms of PRs, several designs have been demonstrated such as adiabatic structures [27, 28, 20, 29], and directional couplers [30, 31, 32, 33]. For PRs using directional couplers, they can be classified further as air cladding [30], high-order mode assisted [31], top etch [33] and top overlay of the other layers [32]. The idea behind them is creating the anti-symmetry for the modes with different polarizations to hybrid with each other. In that way, a coupling between the modes is induced which can possibly leads to fully rotation after certain length of the structure. For example, for directional coupler, if the silicon waveguide is immersed inside of SiO_2 cladding material, then the top-down and left-right symmetries of the structure are maintained. When the two waveguides start approaching each other, due to differences in symmetry between TE and TM modes, no coupling exists between the two modes. However, when the top SiO_2 is removed, the symmetry is broken, a small amount coupling is induced between TE and TM modes which gives the possibility of TM mode to evolve to TE mode. PRs based on directional coupler are generally not fabrication tolerant. The variations of the thickness of the core material (silicon in this case) have a relatively large effect on the performance of the device, leading to a low device yield in wafer level fabrication.

Compared to mode-beating based structures, adiabatic structures are more robust in wafer level fabrication. But the drawback of the adiabatic structures is that they are normally longer compared to mode-beating based structures. Thinking from large-scale communication or computing systems prospect, reliability and accuracy are more important to the performance. Thus, adiabatic structures might be the right way to go in future large-scale systems. Moreover, the size of the integrated adiabatic structures can still be much smaller than their fiber-optical or free-space counterparts. The structures shown before all used multi-layer materials, such as Si_3N_4 on Si [27], Si on Si [28, 29], Si_3N_4 on Si_3N_4 [20]. Besides, layers of materials used in those structures are quite thick which may not be used in current state-of-art CMOS foundries. Confronted with this problem, a PR implemented on 220nm silicon thickness or smaller should be created. And to rule out problems associated with multi-layer materials, single layer silicon with two different etch depths can be used to simplify the process.

PSRs are also quire useful when the photonic circuits are coupled from outside using SMF fibers which do not have a certain polarization and the chip only operates on one of the polarizations (TE or TM). Several nice works have been done in the past few years, including designs based on multi-mode interference (MMI) [34], directional couplers (DCs) [35, 36, 37, 38], and polarization splitter followed by rotator (SFR) structures [39]. Usually, the structures have one-input and two-output ports. Specifically for DC based PSRs, they involve symmetry breaking from cladding materials [35, 38] or high order order mode assistance [36, 37] in mode evolution. The performances of those designed PSRs are already pretty good, both in terms of bandwidth and cross-talk levels. The designs on PSR talked in this chapter are more like an optimization of the adiabatic structure based PSR, using two mask layers for different etch depths of silicon.

2.2 Design Basic Information

2.2.1 Thin-Layer Quandary

For normal size rectangular waveguide, for example, 400 nm in width and 220 nm in height, TE mode is usually the fundamental mode. For adiabatic polarization rotators, one critical point is to achieve indices inversion of TE and TM modes, making TM mode the fundamental mode instead of TE mode. Take 220 nm thickness silicon waveguide for example, to achieve indices inversion, the width of the waveguide needs to be less than 220 nm, making the mode less confined. Since current CMOS foundry favors thin layer silicon structure. Using similar design as shown in ref. [20], as the thickness of silicon layer gets thinner and thinner, etching the waveguide to break symmetry while maintaining a good confinement of the modes becomes a problem. The mode of the etched waveguide becomes less confined, causing extra loss due to coupling to the lossy silicon substrate. Besides, since the mode is large in size, the distance between the waveguide to other structures nearby needs to be large enough, which in turn limits the density of integrated structures.

2.2.2 Multi-Segment

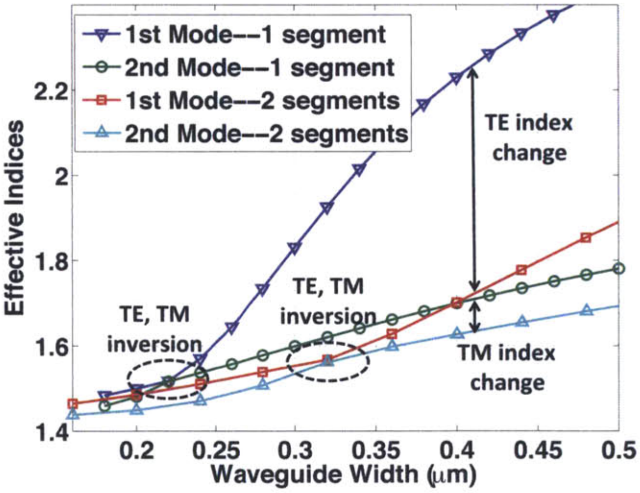

Figure 2-1: Effective indices difference for TE and TM modes for rectangular waveguide and two-segment waveguide. The waveguide width of two-segment represents the addition of both of the waveguide which is twice of the width of the single component. The gap chosen here is 80 nm.

Multi-segment structures come as a rescue for the quandary. The idea comes from the slot mode waveguide structure [40]. The TE modes of the waveguide will see a large difference in index change while TM modes stay similar in cases when the slot exists or not. The Fig. 2-1 shows a typical single piece waveguide effective indices curve with respect to the width of the waveguide and two-segment waveguide with a gap of 80 nm with different widths. The waveguide width of the two-segment stands for summation of the widths of the two segments.

It is shown that the inversion point where TM becomes the fundamental mode gets shifted to large waveguide width and has relative higher effective index which indicates a higher confinement. Besides, from the indices change for TE modes and TM modes by putting a slot in between the waveguides, the effective index of TE mode changed by a huge amount than that of TM mode. This means that the slot waveguide is a powerful structure for engineering TE effective index when less effect on TM index is required.

2.2.3 Basic Structures for Index Engineering

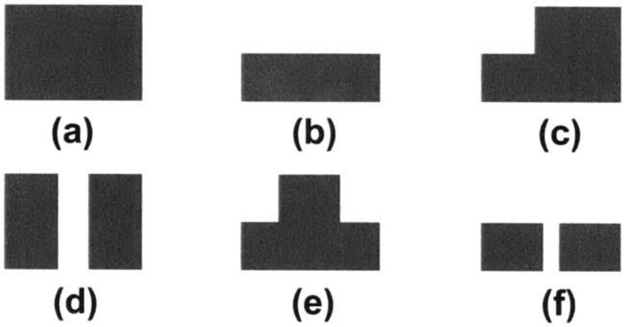

Figure 2-2: Basic shapes of waveguide for polarization manipulation design. (a) Full thickness waveguide. (b) Half thickness waveguide. (c) Ridge etched waveguide. (d) Full thickness slot waveguide. (e) Inversed-T-Shaped waveguide. (f) Half thickness slot waveguide.

The basic structures for effective indices engineering are shown in Fig. 2-2. From left to right and top to bottom are (a) full thickness waveguide, (b) half thickness waveguide, (c) ridge etched waveguide, (d) full thickness slot waveguide, (e) inversed-T-shaped waveguide, (f) half thickness slot waveguide. These six basic shapes have different effective indices relations between first order and second order mode. For (a) and (b), only one degree of freedom (width) can be used. But for (c), (d), (e) and (f), two degrees can be used, giving more flexibility for designs.

Ridge waveguide (Fig. 2-2(c)), in itself, breaks both the vertical and horizontal symmetries. Thus, it has the possibility of hybridizing TE and TM modes and achieving rotation between the modes. It is a critical component in designing polarization rotation related structures.

The polarization beam splitter (PBS) talked in the next chapter uses the inverse-T-shaped waveguide (shown in Fig. 2-2(e)) and full thickness rectangular waveguide (shown in Fig. 2-2(a)) as its basic components. The inverse-T-shaped structure has the capacity of having different TE and TM effective indices gaps compared to full thickness rectangular waveguide while still maintaining a good confinement of both of the modes.

2.3 Multi-Segment Polarization Rotator

2.3.1 Schematic

From the discussion of last section on two-segment waveguide, it is clear that the TE and TM inversion point is moved to large waveguide width and larger effective index. From Fig. 2-1, by setting the total width of the two-segment waveguide to be less than 0.32 μm, the inversion of TE and TM modes can be achieved. To have a relatively large effective indices gap between TE and TM modes while maintaining a relative large effective indices numbers, the width selected here is 0.28 μm, corresponding to 0.14 μm for each segment. The TE and TM modes of the structure are shown in Fig. 2-3. The effective indices difference is $\Delta n_{eff} = 0.0297$.

The initial structure is then ridge-etched to break the symmetry of the waveguide to hybrid the TE and TM modes using the same method as discussed in [20]. It is shown in Fig. 2-4. The differences of current design from the design in ref. [20] are the material difference and rotation scheme difference. We are using thin-layer silicon waveguide which is compatible with CMOS process while ref. [20] use silicon rich silicon nitride as the basic material. Besides, the rotation scheme used in ref. [20]

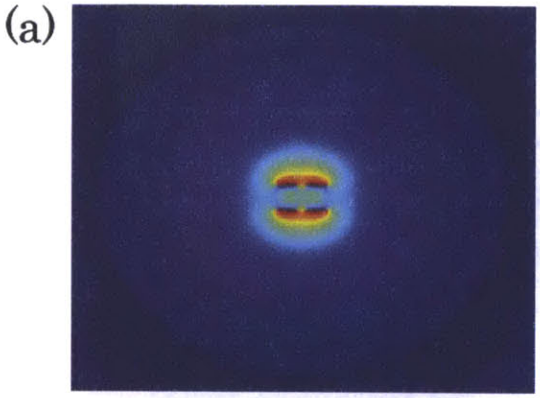

TM mode (n_{eff} = 1.5386)

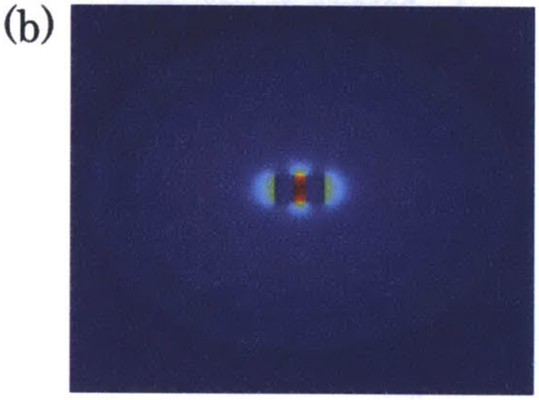

TE mode (n_{eff} = 1.5071)

Figure 2-3: Modes profiles of two-segment waveguide of wavelength 1.55 μm. (a) TM modes, n_{eff} = 1.5360; (b) TE modes, n_{eff} = 1.5063. The width of each waveguide is 140 nm and the gap between them is 80 nm.

can be viewed as a global rotation of the modes while in this case, the rotation can be thought as local rotations of each part of the mode. To determine the width size of the final half thickness waveguide and the length of the transition, more scans on effective indices need to be done to ensure a large indices gap between first two modes to avoid cross-talk between TE and TM modes along the transition. By changing the end width of the final two-segment waveguide, the change of the effective indices curve can be extracted. Here, two factors need to be taken care of. One is the effective indices gap between the first order mode and second order mode. The other one is the size of the end width which is related to the speed of the width change. The criteria

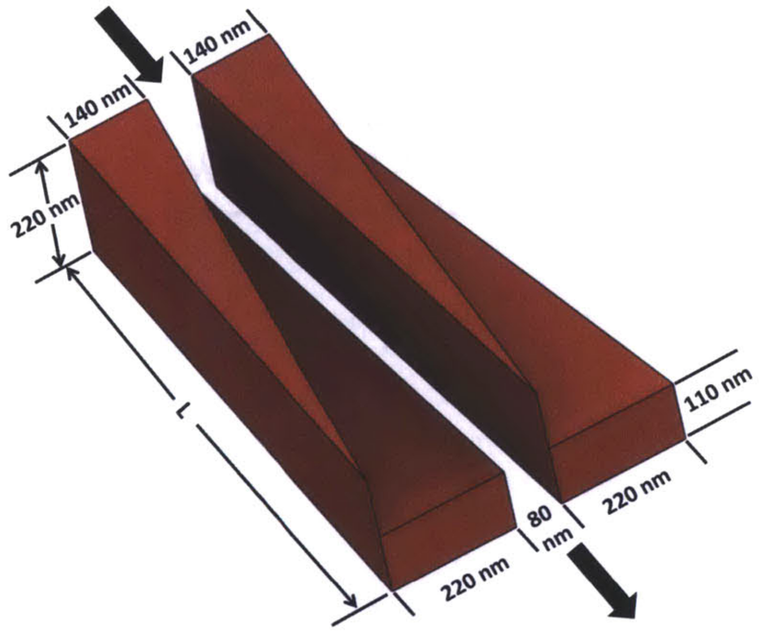

Figure 2-4: Schematic of two-segment polarization rotator.

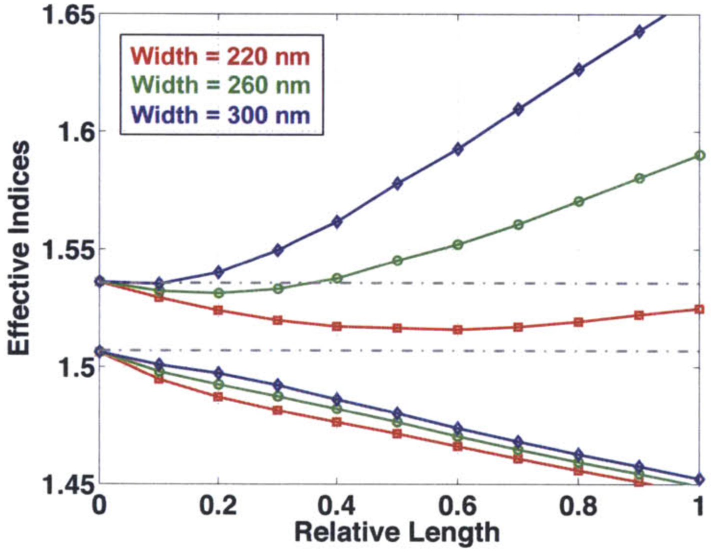

Figure 2-5: Effective indices curve along the structure for different end width size.

set here is maintaining a large enough index gap while having a minimal end width to slow down the speed of width change. The indices curve along the structure for different end width is shown in Fig. 2-5. Combining these factors, the end width of each half thickness segment is selected to be 220 nm. By looking at the indices curve, the mode confinement factor can be approximately determined. Since the effective index of the second order mode is quite small, the mode is quite large which introduce extra loss to the substrate. In that case, the second order mode can be quite lossy. Thus, from top to down in Fig. 2-4, the structure can be used as a TM to TE rotator while from down to up, it can be used as a TE to TM rotator.

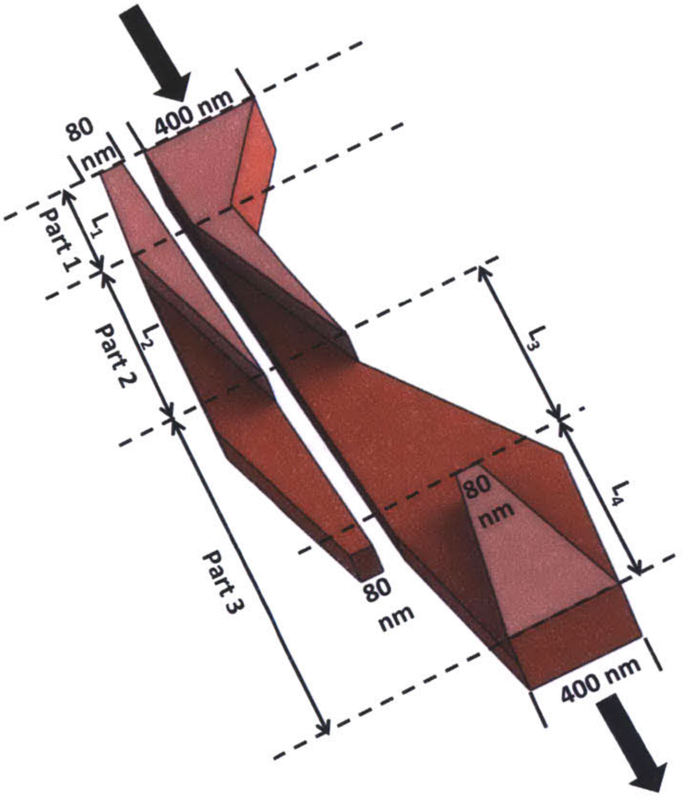

Figure 2-6: Full schematic of the two-segment polarization rotators.

The full schematic of the design is shown in Fig. 2-6. It consists of three parts. The first part is used as an adaptor to convert straight waveguide mode to two-segment slot mode. At first, for 400 nm width waveguide, the effect from an 80 nm width waveguide at an distance of 80 nm is negligible. Then the 400 nm width waveguide is tapered down to 140 nm and 80 nm width waveguide is tapered up to 140 nm. The TE mode will stay as TE mode and TM mode will also stay as TM mode by the symmetry constraint. The fundamental mode of the structure is changed to TM mode after this part. Transition length of 100 μm is chosen as a conservative number. The second part acts as the convertor to convert two-segment TM mode to two-segment TE mode. That is the critical part of the design. The symmetry of the structure is broken by the ridge etch of the waveguide. The third part is another mode adaptor to change the two-segment TE mode back to full thickness straight waveguide TE mode. It consists of two structures, one for changing the mode of half-thickness segmented waveguide to half-thickness regular waveguide and the other one for convert the half-thickness waveguide mode to full-thickness waveguide mode. The transition lengths are picked to be 100 μm for both L_3 and L_4.

2.3.2 Simulation

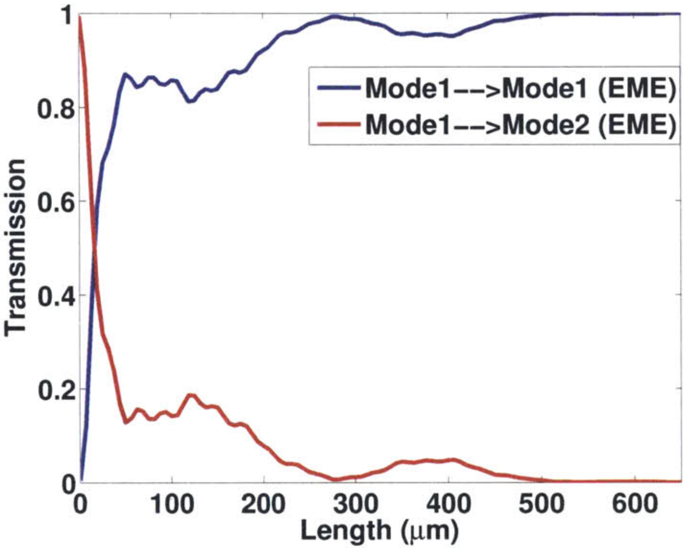

Figure 2-7: Eigen Mode Expansion (EME) simulation result of the part 2 of the overall structure with gap size of 80 nm

To determine the length of Part 2 of the structure in Fig. 2-6, EME method using FIMMPROP[1] is utilized and the responses of it is shown in Fig. 2-7. The length determined for L_2 is 600 μm. The device designed uses adiabatic transition as the main design rule, which indicates an intrinsic wide-band property. To justify the wide-band property of the device, wavelength scan is performed in FIMMPROP.

---

[1] FIMMPROP is a software designed by Photon Design, Oxford, UK.

Fig. 2-8 shows the wavelength dependence of the structure. From that, crosstalk level of less than -15dB and negligible propagation loss for wavelength range from 1.50 to 1.60 μm are observed.

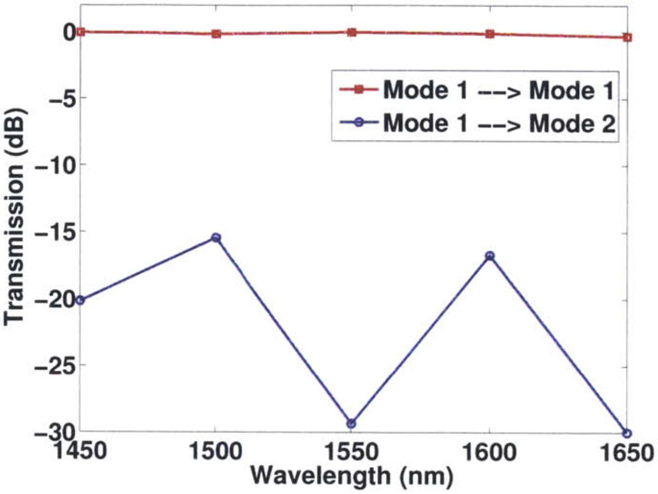

Figure 2-8: Wavelength dependence of the Part 2 of the overall structure with gap size of 80 nm and length of 600 μm.

2.4 Polarization Splitter and Rotator

2.4.1 Schematic

The schematic of the PSR is shown in Fig. 2-9. The structure starts with normal two input rectangular waveguides with width of 400 nm and 2 μm separation between them. The waveguides then get tapered and ridge etched on one side of the two waveguides. The fundamental mode of the top waveguide then has an effective index which is smaller than the second order mode of the waveguide below. The two waveguides are then brought near to each other through an adiabatic transition. Because the indices for different modes are quite different, the modes stay in the same order and do not couple to each other. In the middle part of the structure, the top waveguide is broadened so that at the end of this section, the second order mode of the overall structure becomes concentrated in the top waveguide. The waveguides

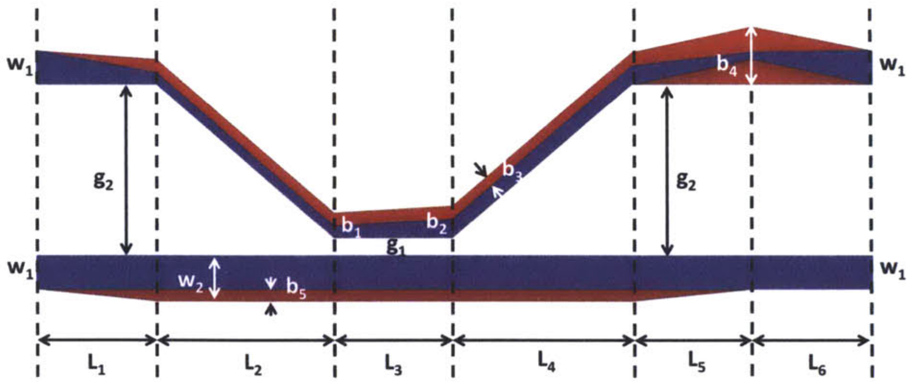

Figure 2-9: Schematic of the PSR structure designed. In the structure, the associated size of each part of the structure are listed as following: w_1 = 400 nm, w_2 = 540 nm, b_1 = 300 nm, b_2 = 380 nm, b_3 = 160 nm, b_4 = 680 nm, b_5 = 140 nm, g_1 = 100 nm, g_2 = 2.0 μm, L_1 = 100 μm, L_2 = 500 μm, L_3 = 200μm, L_4 = 500μm, L_5 = 100μm and L_6 = 150μm.

get separated again in L_4 region until they are far apart by 2 μm. Now, the initial second order mode sent from the left side of the whole structure evolves to a mode concentrated in the top waveguide. The next step is a mode adapter which changes the ridge waveguide mode to a full thickness rectangular waveguide mode.

For part L_1, L_2, L_4, L_5 and L_6, they are just simple structure for mode evolution which does not include mutual coupling between waveguide. So the analysis of those parts is neglected. For optimization on the total size of the structure, further simulation needs to be performed on those parts to get the minimum length to make the device more compact. So, from now on, I will focus on the analysis of the L_3 part of the device.

2.4.2 Simulation

The effective index curves of the L_3 part are shown in Fig. 2-10. The arrow shown in the figure indicate the hybrid of modes. There is a wide gap between the effective indices of the second order and third order, which indicates a strong mode coupling between second order and third order modes. The idea associated with this design is breaking symmetry. Normally, TE and TM modes will not couple to each other if the

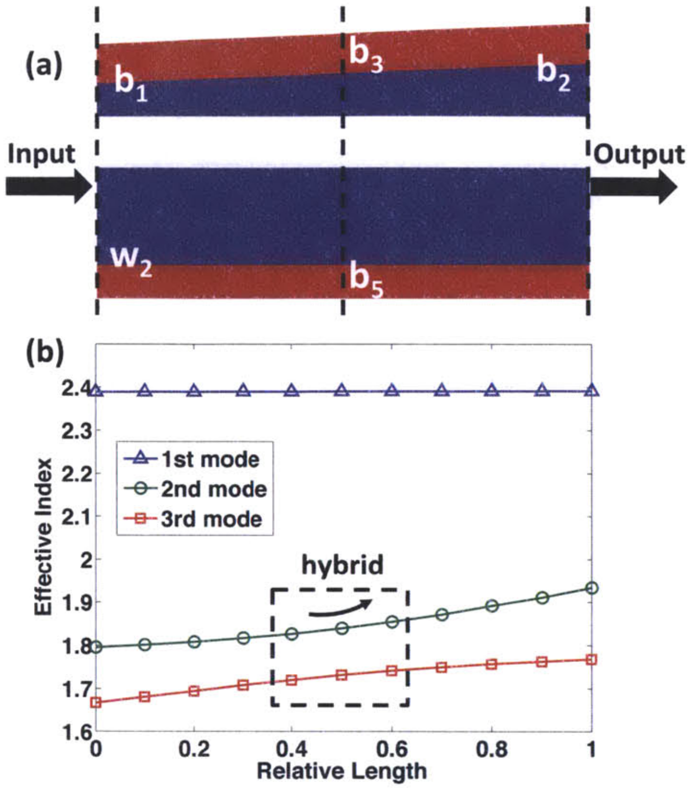

Figure 2-10: (a) Middle part of the designed polarization splitter and rotator. (b) Effective indices curves of the first three modes along the structure. The dotted rectangle indicates the region where the second and third mode get hybrid and create index gap between them.

horizontal and vertical symmetries are not broken. In that case, the effective indices curves will only cross each other without creating an anti-crossing gap.

Using Eigen Mode Expansion method, the mode evolution results are shown in Fig. 2-11. By selecting a length of 100 μm for the structure, the eigenmode will mostly stay in the same order of mode. Since the initial second order mode for input from L_2 is the TM mode of the waveguide downside and the initial third mode is the TE mode of the waveguide upside, the TM mode will evolute to the TE mode at the output of the left side, thus making the structure a polarization rotator. Beside, the initial fundamental TE mode of structure will stay as the fundamental mode along the structure. In that case, the TE mode will exit at the output port downside without getting interfered by other order of modes. Since different input polarizations exit at different output ports and the TM input mode is changed to TE mode, the structure will function as a PSR in general.

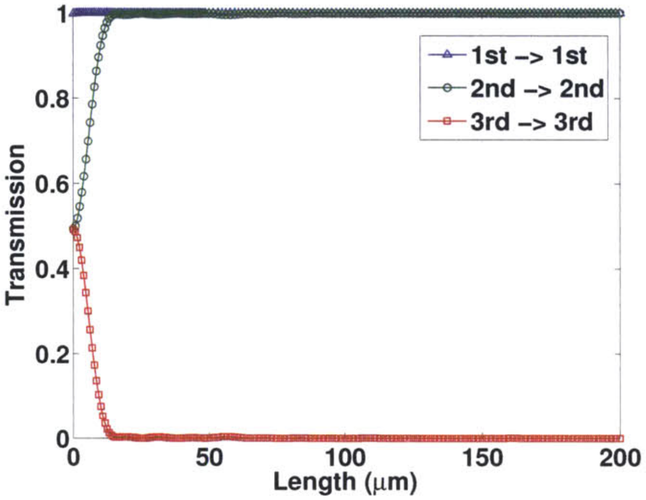

Figure 2-11: Eigenmode Expansion simulation on PSR designed. The transmission change with respect to length of the structure.

To get a view of the wavelength dependence of the structure, EME method for different wavelengths is used for structure length of 100 μm. By scanning the wavelength, the wavelength dependence of the structure can be extracted and is shown in Fig. 2-12. From the figure, we can tell that the PSR designed is almost wavelength independent and has an extinction ratio of more than 25dB over a range of 1400 nm to 1700nm. This proves it to be a useful device in real application.

2.4.3 Future Application

Besides the application as a polarization splitter and rotator (PSR) for on-chip polarization manipulation, the PSR can also be used as a critical component for on-chip interferometer. By connecting the two outputs of the PSR together, TE input can be reflected back and becomes TM polarized. This function is similar to a quarter wave plate in the free space interferometer setup and may pave the way for on-chip interferometer realization.

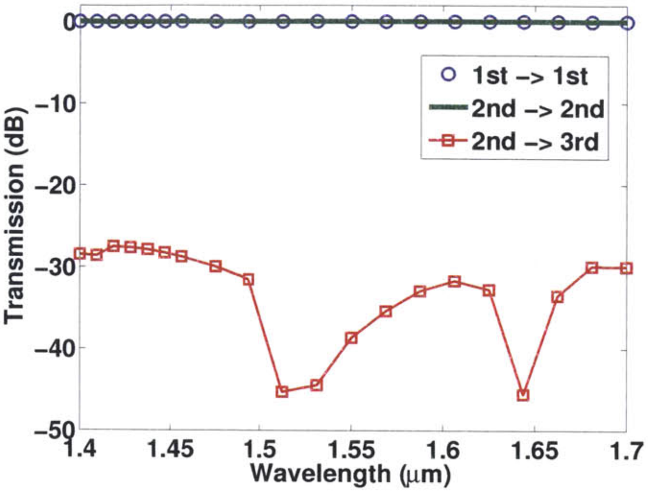

Figure 2-12: Wavelength dependence on the performance of the polarization splitter and rotator designed.

2.5 Summary

In this chapter, design techniques and simulation results for polarization rotator (PR) and polarization splitter and rotator (PSR) are discussed. Multiple structures for index engineering are analyzed and further used in the polarization manipulation system. The difficulty of current adiabatic rotator design on thin layer materials is solved by the multi-segment structure proposed here.

Chapter 3

Polarization Beam Splitter

Photonic components are being integrated within CMOS-compatible platforms as opposed to discrete components, widely used for data-com within high performance computing and telecommunication applications. Integrated silicon photonics [41] offer single-mode operation, unprecedented bandwidth density and compactness that can leverage the Moores law scaling [42] for off-chip communications and even within the chip (e.g. intra-chip) communications. Silicon and Si_3N_4 are widely used materials of choice due to their inherent CMOS-compatibility and high index contrast to cladding materials such as SiO_2. However, both suffer from geometrical polarization birefringence except for polarization insensitive square waveguide cross-section. Further, the square cross-section requires sub-nm control over waveguide features (width and height), which is still not available for a wafer-scale fabrication. Additionally, advanced CMOS nodes are continuously shrinking the height of the active silicon layer in order to satisfy Moores law scaling in computations, which in turn favors high-confinement wide and thin waveguide cross-section and transverse-electric (TE) fundamental mode. Although, polarization-maintaining fiber (PMF) can be utilized to maintain polarization between chip-to-chip, rack-to-rack and blade-to-blade communications within high performance computers, the cost of the PMFs far exceeds the benefits of integrated silicon photonics. The single-mode-fiber (SMF) cannot preserve the polarization state and for a wavelength-division-multiplexed (WDM) system, the polarization state will also be dependent on wavelength. Therefore, on-chip polarization diversifying or insensitive networks are required.

3.1 Motivation on PBS

The robust way to achieve polarization insensitive networks is to have an on-chip polarization splitter to separate input polarization into two orthogonal states and rotate the transverse-magnetic (TM) mode into TE mode. Then, identical photonic networks can be used and both ports can be combined into an off-chip SMF using the reverse of the polarization splitter as a combiner. Various polarization splitters have been demonstrated over 100 nm, ~70 nm, 55 nm, 20 nm, 40 nm, 115 nm bandwidth using an adiabatic Si_3N_4 polarization splitter [39, 21], silicon bent directional couplers (DCs) [43], silicon cascaded asymmetrical DCs [44], a silicon two-dimensional photonic crystal [45], double-layer silicon grating couplers [46] and a silicon arrayed waveguide grating (AWG) [47], respectively. Although, directional couplers can be demonstrated with a bandwidth similar to adiabatic couplers, the wafer-scale variations in width and height of the waveguide cross-section still maintain as a major limiting factor for them.

While components such as polarization splitter (PS) [44, 43], polarization rotator (PR) [27] and polarization splitter and rotator (PSR) [34, 36] have been demonstrated on silicon platform, an on-chip correspondent of free-space polarization beam splitter (PBS) has not been demonstrated yet. All the PBSs demonstrated so far are in themselves PSs, which have only one-input and two-output, while a full-functional PBS requires a two-input two-output configuration. Applications for on-chip insensitive photonic circuits and polarization multiplexing scheme such as dual-polarization differential quadrature phase shift keying (DP-DQPSK) [48] only require the use of the PSs and PRs. However, for more accurate systems such as polarization-entangled states generation and manipulation in quantum optics [49] or heterodyne sagnac interferometers [50], a full-functional two-input two-output PBS is required.

3.2 Design on PBS

In this section, the theory and design techniques on the broad-band PBS are discussed. In terms of highly-confined guided modes (e.g. TE and TM modes mentioned above), they are hard to couple to leaky modes due to large differences in the propagation constants. Thus, the loss due to coupling to leaky modes of the confined modes can be negligible. In this case, assuming weak coupling between the confined modes, the coupling coefficient κ_{mn} (z) between mode m and mode n can be expressed as [21],

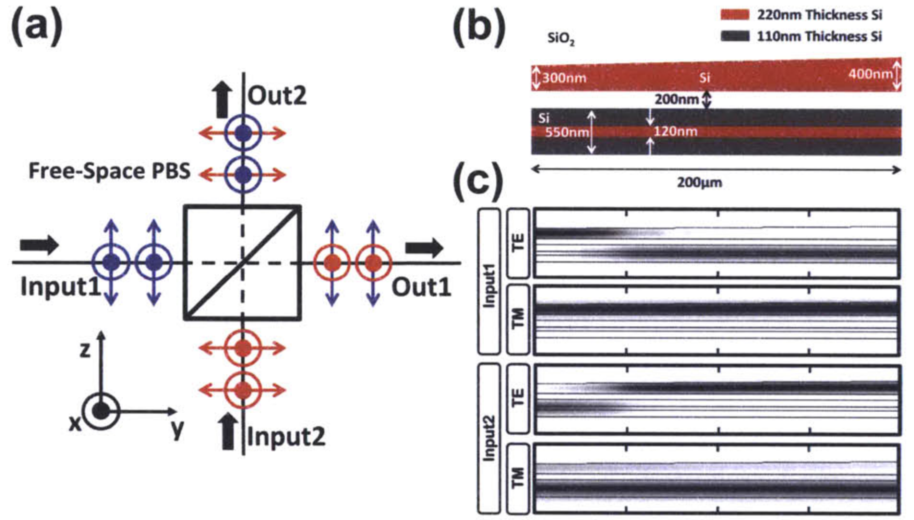

Figure 3-1: (a) The function of traditional free-space polarization beam splitter cube. (b) Transition region of the proposed structure for on-chip polarization splitting. (c) Modes evolutions using eigen-mode expansion method by FIMMPROP[1]. It consists of TE and TM modes of which most of the power is in the T-shaped waveguide and TE and TM modes of which most of the power is in the rectangular waveguide.

$$\kappa_{mn}(z) = \frac{\omega}{4\delta\beta(z)} \int_A \mathbf{e}_m^*(x, y, z) \cdot \mathbf{e}_n^*(x, y, z) \frac{\mathrm{d}}{\mathrm{d}z} \varepsilon(z) \mathrm{d}A \tag{3.1}$$

where $\mathbf{e}_k(x, y, z)$ stands for normalized vector electric field of mode k, $\delta\beta(z)$ is the difference in the propagation constants as a function of length z, ω is the angular frequency of the input light, $\varepsilon(z)$ is the electric permittivity as a function of length,

---

[1] FIMMPROP is a software designed by Photon Design, Oxford, UK.

A is the perturbed area. Then, the power transferred to mode m (P_m) from mode n can be written as,

$$P_m(z) = 2|\frac{\bar{\kappa}}{\delta\bar{\beta}}|^2 \left[1 - \cos(\delta\bar{\beta} z)\right] \tag{3.2}$$

where $\bar{\kappa}$ is the average coupling coefficient and $\delta\bar{\beta}$ is the average difference in the propagation constants. They can be expressed as $\bar{\kappa} = (1/z)\int_0^z \kappa(z')\mathrm{d}z'$ and $\delta\bar{\beta} = (1/z)\int_0^z \delta\beta(z')\mathrm{d}z'$. In general, for an adiabatic transition, ratio between $\bar{\kappa}$ and $\delta\bar{\beta}$ needs to be much smaller than 1 to ensure negligible coupling to unwanted modes. $\delta\bar{\beta}$ is determined by the waveguide shape and relative length ratio for each part of the device. For a given $\delta\bar{\beta}$, the ratio can be reduced by introducing a slowly varying permittivity function $\varepsilon(z)$, which minimized $\mathrm{d}\varepsilon(z)/\mathrm{d}z$. If the condition is also satisfied for a broad wavelength range, the modes will evolve along the effective index curve as a function of device length and enable a broadband operation.

The function of traditional free-space polarization beam splitter cube is illustrated in Fig. 3-1-a. It has two input ports and two output ports. The input states can be split into two orthogonal states, namely within y-z plane and orthogonal to y-z plane. The in-plane states of both input ports will pass through while the orthogonal-to-plane states will be reflected.

For device on chip, the input states will have TE and TM modes as two orthogonal states. In order to form an on-chip PBS, one of the polarization states need to switch output ports (e.g. input port 1 or 2 to output port 2 or 1) and the orthogonal polarization state will pass through the ports (e.g. input port 1 or 2 to output port 1 or 2). This requires an anti-crossing curve of the effective indices in both waveguides within the transition region for the crossing polarization states and large effective indices difference for the passing-through states. Therefore, a inverse-T-shaped (ITS) and a rectangular waveguide cross-section, shown in Fig. 3-1-b, are chosen to achieve an anti-crossing curve for TE modes while preserving the confined TM modes that pass through the transition with minimum crosstalk. The transition region is adiabatically tapered in order to preserve mode-evolution for an ultra-broad wavelength range. For a 220nm full and 110nm ridge thickness, waveguide critical

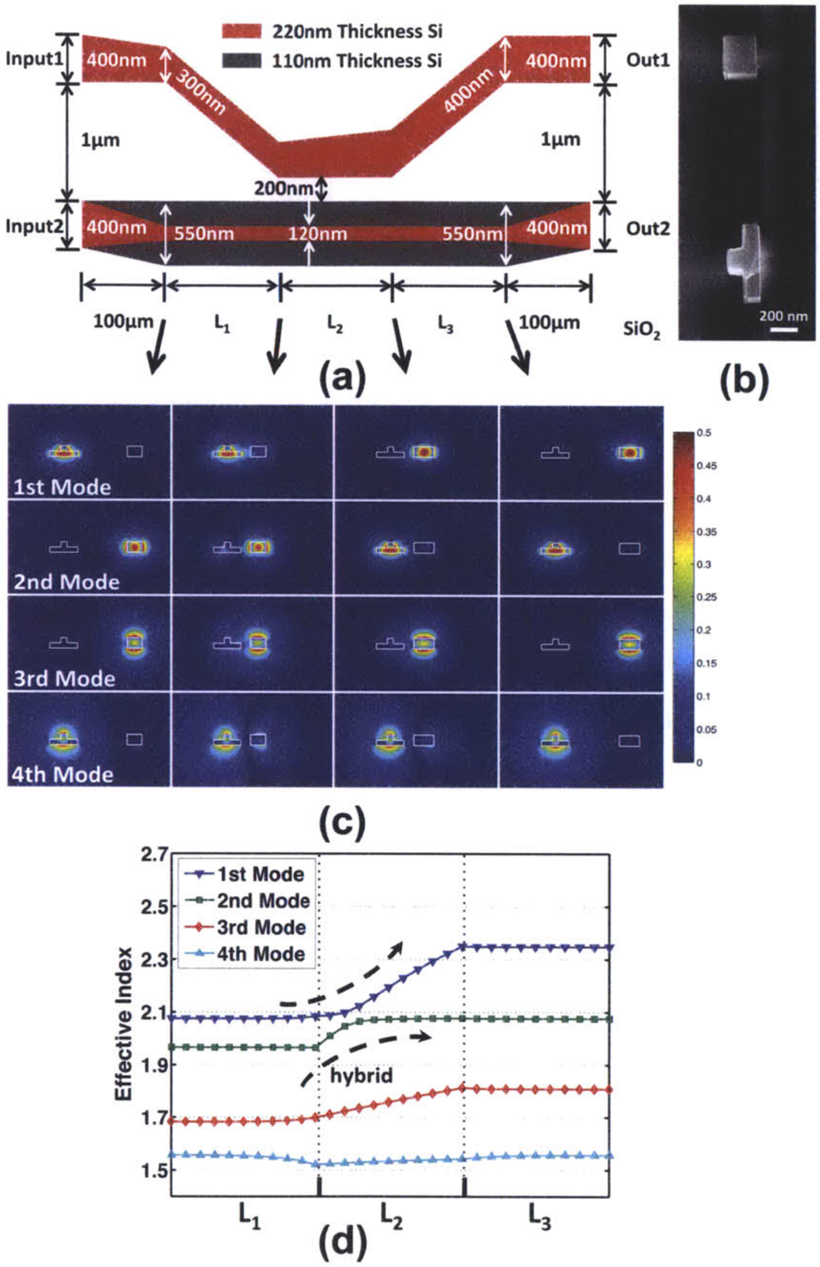

Figure 3-2: (a) Schematic of the full PBS. $L_1 = 500\mu m$, $L_2 = 200\mu m$, $L_3 = 500\mu m$. (b) Cross-section SEM of the device. (c) Eigen-modes profile for corresponding cross-section of the device in order of effective indices. (d) Mode effective indices evolutions from the beginning of the second part to the end of the fourth part.

dimensions (e.g. width), shown in Fig. 3-1-b, are optimized for broadband operation from λ=1350 nm to λ=1500 nm. The transition region is also simulated using an eigen-mode expansion (EME) software and mode-evolutions within the transition region for 2-inputs and 2-polarizations states are shown in Fig. 3-1-c for wavelength 1460nm. It is clear that the input TE modes will switch ports while the TM modes passing through.

The adiabatic transition region is attached to input and output couplers to ensure broadband operation. The resultant PBS structure is depicted in Fig. 2-a. The input waveguides are 400 nm in width to ensure high confinement and minimize substrate leakage. The initial separation of 1μm is chosen to minimize crosstalk between 2-inputs and 2-polarizations. Then, the top waveguide is shrunk down to 300 nm with a linear 100 μm-long taper and the top-half of the bottom waveguide is linearly tapered down to form an ITS waveguide with 120nm wide top-half and 550nm wide bottom-half (Fig. 3-2-a). This part acted as a mode adaptor to separate effective indices of each port for TE and TM polarization states. Further, the waveguides are brought close to each other and smoothly interacted (e.g. 500 μm-long) and the transition region, shown in Fig. 3-1-b, is attached after the interaction region with a length of 200 μm. A similar but reverse interaction region is used after the transition region to separate ports and a reverse mode adapter is used to achieve two separate output ports with 1 μm separation. The design ensured low crosstalk and smooth interaction and adiabatic mode-evolution based transition regions for broadband operation. The eigen-mode profiles of each section and the effective indices curve along the device are shown in Fig. 3-2-c and Fig. 3-2-d. Since the modes evolve along the effective indices curve under adiabatic limit, after the transition region, the power of the TE modes switches from rectangular waveguide (ITS waveguide) to ITS waveguide (rectangular waveguide).

3.3 Simulations

The design was given in the last chapter, without talking about the simulations which determine the lengths of each part of the structure. The critical part of the structure is L_2 part where the power of the TE mode concentrates at one waveguide at the

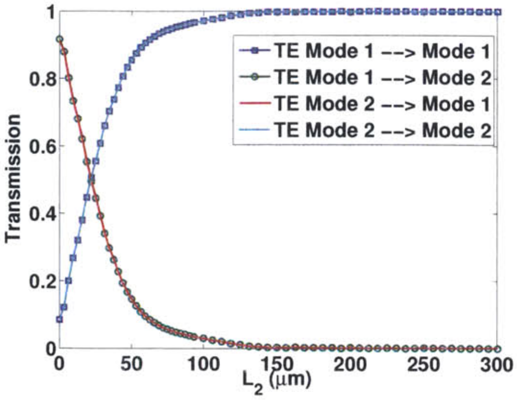

(a) TE response

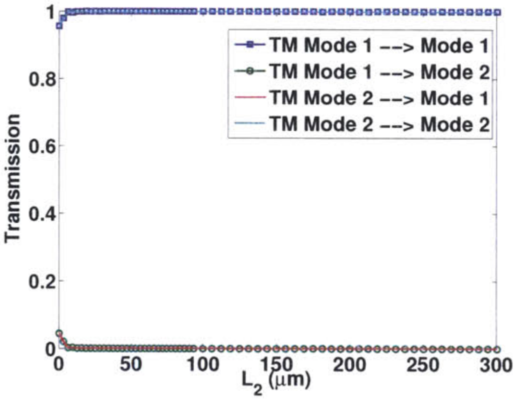

(b) TM response

Figure 3-3: (a) EME simulation of TE response of the PBS for different lengths of L_2. (b) EME simulation of TM response of the PBS for different lengths of L_2.

beginning and gets transferred to another waveguide at the end of the structure while TM modes powers stay mostly in the same waveguides. To analyze the structure, EME simulations are performed using FIMMPROP software. The result for L_2 part at wavelength 1460 nm with respect to the length of L_2 is shown in Fig. 3-3. From that, we can see a length of 200 μm in the L_2 part is enough to ensure a reasonable extinction. Furthermore, by scanning the wavelength, wavelength dependence of the structure can be extracted. Fig. 3-4 and Fig. 3-5 show the responses of TE and TM modes. Since the design is based on adiabatic transition, broad-band operation is expected. The EME simulation shows a quite broad-band operation of around 200 nm for both polarizations. However, there are some factors that have not been taken

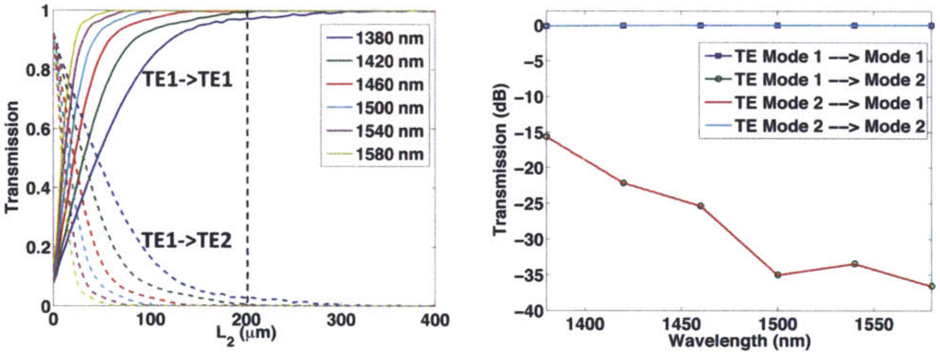

(a) **(b)**

Figure 3-4: (a) Length scan response for different wavelengths for the transition between TE mode 1 in the beginning to the TE mode 1 and TE mode 2 at the end. (b) Plot of the wavelength scan for $L_2 = 200$ μm (indicated in the dotted line in (a)).

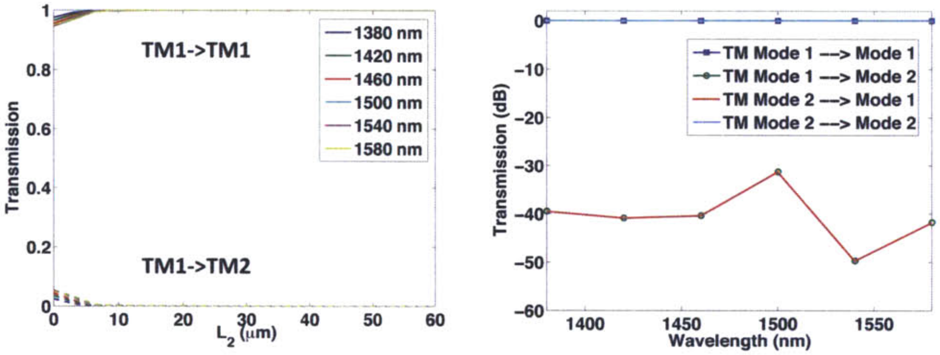

(a) **(b)**

Figure 3-5: (a) Length scan response for different wavelengths for the transition between TM mode 1 in the beginning to the TM mode 1 and TM mode 2 at the end. (b) Plot of the wavelength scan for $L_2 = 200$ μm (indicated in the dotted line in (a)).

into consideration when performing the EME simulation such as the loss to lossy substrate and dispersion of the materials.

3.4 Fabrication and Measurement

The proposed structure was fabricated on a CMOS-compatible SOI 12" wafer with silicon thickness of 220 nm and top and bottom oxide thickness of about 3.3 μm and 2.0 μm separately. The cross-section SEM figure of the fabricated device within the input coupler region is shown in Fig. 3-2-b. The T-shaped waveguide has 110 nm ridge thickness and 120nm wide top-half and 550 nm wide bottom-half. To analyze the device from fabrication prospect, cut on different positions on the chips was done and the chips were dipped into hydrogen fluoride (HF) to remove the cladding SiO_2 to increase contrast for viewing in SEM. The figures of SEM on several different cut position are shown in Fig. 3-6. The figures showed a reliable fabrication technique and good mask alignment.

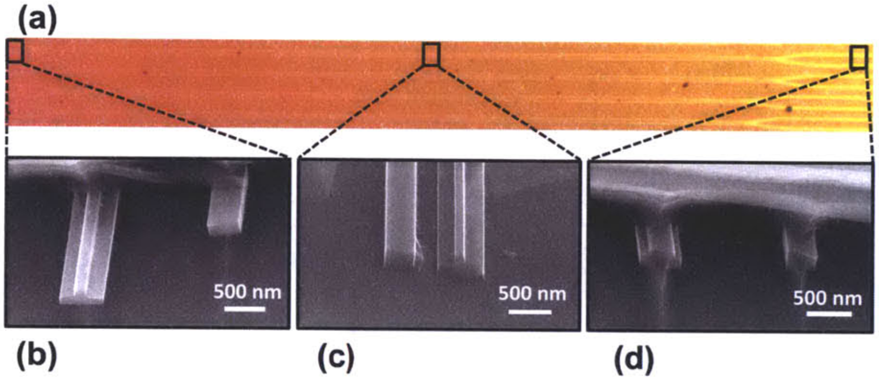

Figure 3-6: (a) Optical microscope figure of the device. (b)(c)(d) SEM images for different positions marked by the rectangles on the (a).

The fabricated device was coupled by using an off-chip lensed SMF and cross and through responses are observed through identical lensed SMF. At the both ends of the chip, inversely tapered waveguides were used to maximize the coupling from the fiber to the chip. An external polarization controller was used to manipulate the input polarization states and a nearby integrated micro-ring resonator was used to identify polarization states for a given wavelength range. Additionally, the coupling for each polarization is normalized to a nearby straight waveguide with identical coupling regions and waveguide width. The TE mode from both input ports are excited separately, both output ports are measured to identify crosstalk and the results from λ=1350 nm to λ=1520 nm are depicted in Fig. 3-7-a. The TE mode, excited from any of the 2-inputs, have achieved >170 nm bandwidth operation and <-10 dB crosstalk and negligible insertion-loss. Similarly, the TM mode from both input ports are excited separately, both output ports are measured to identify crosstalk

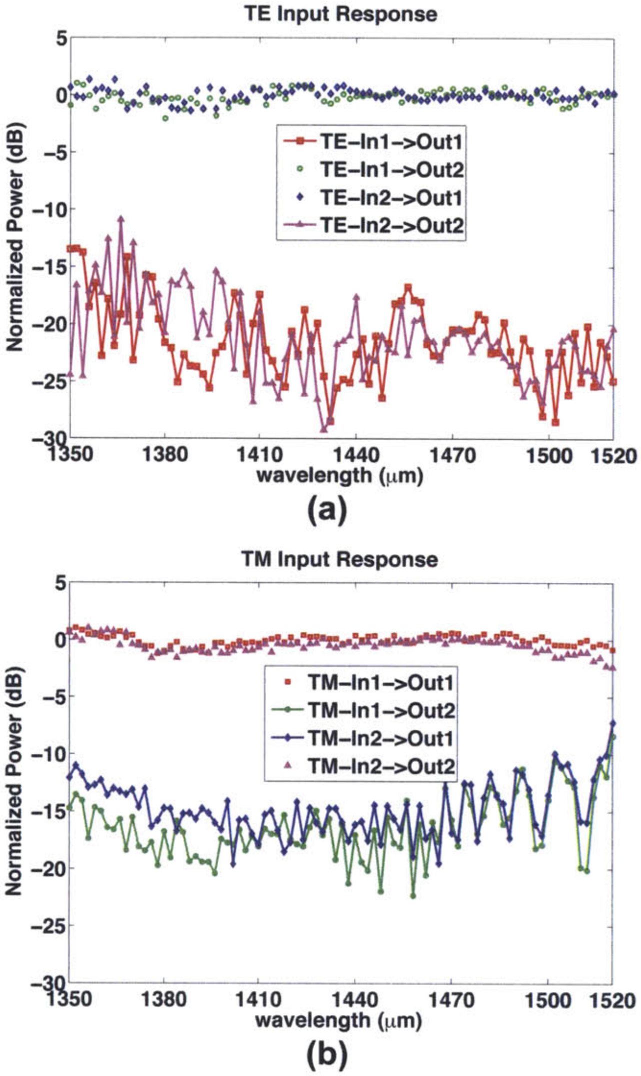

Figure 3-7: Insertion loss measurement response of PBS for (a) TE input (b) TM input at different output ports. The results are normalized to a nearby waveguide structure.

and the results from λ=1350 nm and λ=1520 nm are depicted in Fig. 3-7-b. The TM mode, excited from any of the 2-inputs, have achieved >150 nm bandwidth from λ=1350 nm and λ=1500 nm operation and <-10 dB crosstalk and negligible insertion-loss. The crosstalk for TM can be further minimized by simply separating the input and output mode adapters by >2 μm instead of 1μm and extending the coupler region length to minimize TM crosstalk for λ <1500 nm. The bandwidth is limited by multi-mode operation of TE mode and insufficient transition length for λ <1350 nm and substrate leakage of TM mode for λ >1500 nm. Further, slightly increasing the overall dimensions of the device will lead to highly confined TM mode and the PBS can have better performance in C and L band as well.

3.5 Design Improvements and Further Discussions

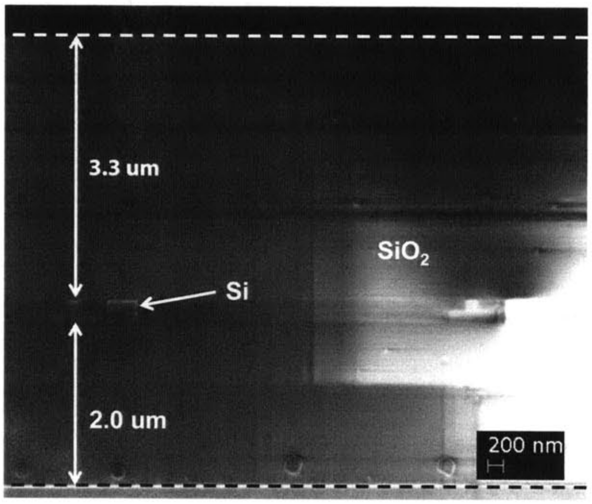

Figure 3-8: SEM picture of the cross section of the PBS. Top cladding is 3.3 μm and bottom cladding is 2.0 μm.

The explanation for TM modes not working above λ =1510 nm is expressed as substrate leakage. This can be simulated using mode solver. The SEM figure for the size of cladding is shown in Fig. 3-8. The thickness of top and bottom cladding of SiO$_2$ are measured as 3.3 μm and 2.0 μm separately. The simulation structure is shown in Fig. 3-9 with index values labeled for each part of the structure. By solving the complex effective index of the structure for the TM modes, the loss value of the mode can be easily extracted. The simulation results are shown in Fig. 3-10. It is clear that the substrate effects on TE modes are negligible while it becomes significant for the fourth order modes (second order TM modes) for longer wavelength. That explains why the TM mode response of the PBS fabricated has larger loss for longer wavelengths. Thus, the substrate leakage sets a limit for the longest wavelength on

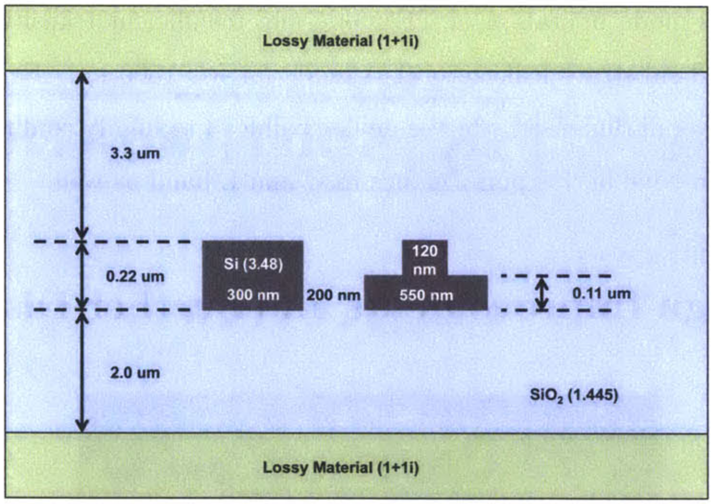

Figure 3-9: Structure for measuring the loss of the mode. Material with complex index of 1+1i is used to extract the loss.

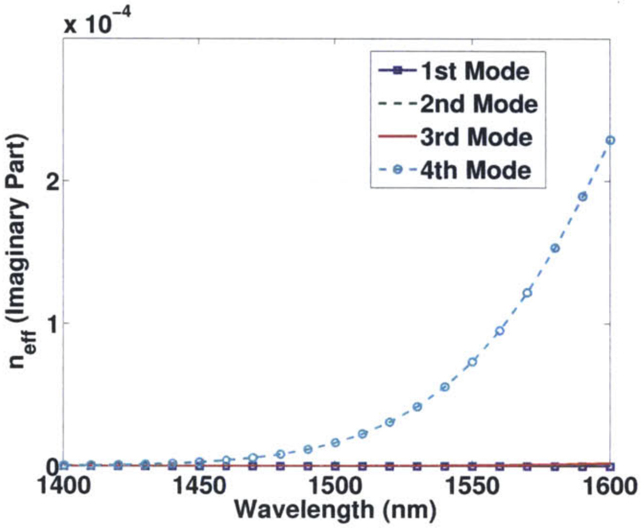

Figure 3-10: Imaginary part of effective index of the first 4 modes versus the change of wavelength for the structure shown in Fig. 3-9.

which the device can work.

To improve the design and make it suitable for working in C (1530 - 1565 nm) and L (1565 nm - 1625 nm) band, the structure can be slightly enlarged so that the TM modes become more confined for longer wavelengths while the indices relations of the modes stay the same. Besides, there are more alternative ways to achieve PBS. The structures discussed before manipulate the TE modes of the waveguides for shifting ports while keep TM modes staying in the same waveguides. Another scheme on keeping TE modes staying the same while shifting the TM modes is also possible. To look into the possibility to achieve such structures, the following shape (shown in Fig. 3-11) is created and the effective indices curves (shown in Fig. 3-12) match with the requirement of PBS structures.

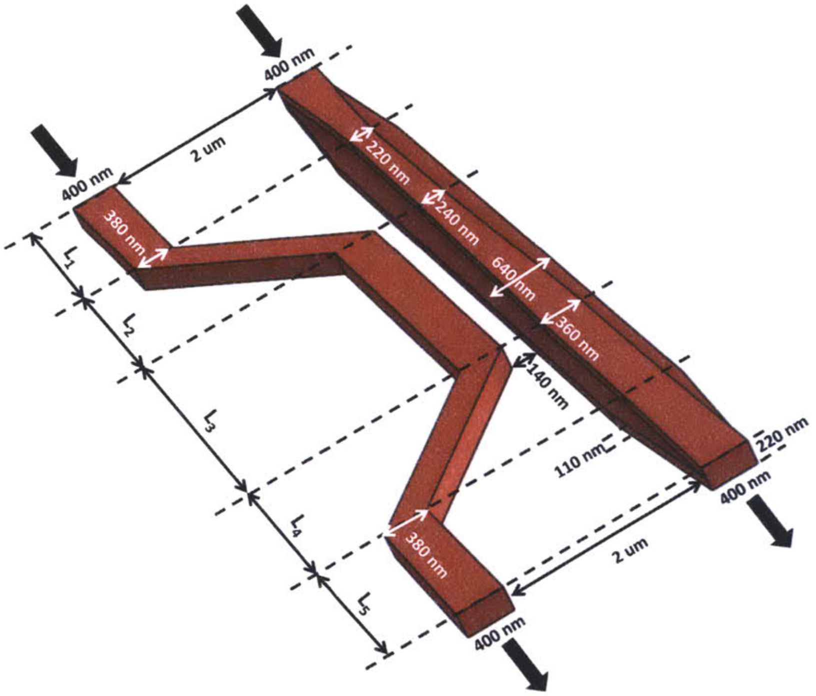

Figure 3-11: Alternative PBS design. TM modes of the input waveguides change ports while TE modes stay in the same ports.

The advantage of manipulating the modes in this way is the improvement of the confinement for the TM modes, which makes it suitable for working in longer wavelengths.

The EME simulation result for L_3 part of this new design is shown in Fig. 3-13 and great reduction of the taper length is achieved which will potentially make PBS more compact. Besides, wavelength scans on that structure are included in Fig. 3-14 which solidifies the wide-band property of the design.

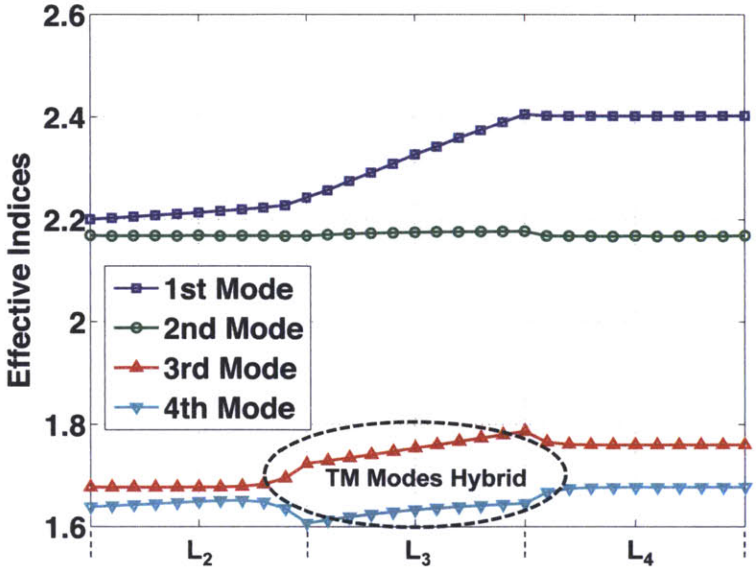

Figure 3-12: Effective indices curves for L_2, L_3 and L_4 parts of the structure designed in Fig. 3-11.

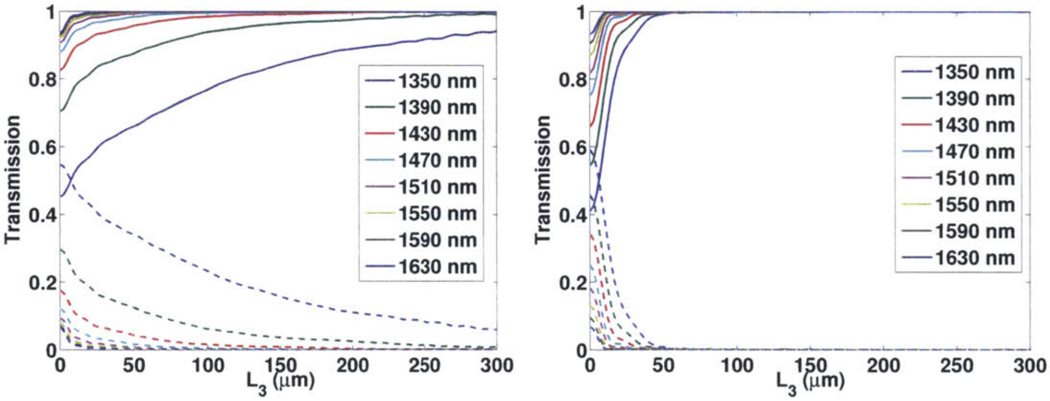

(a) TE response

(b) TM response

Figure 3-13: (a) EME simulation of TE responses of the PBS shown in Fig. 3-11 for different lengths of L_3 at wavelength of 1550 nm. (b) EME simulation of TM responses of the PBS shown in Fig. 3-11 for different lengths of L_3 at wavelength of 1550 nm.

3.6 Summary

In conclusion, a 2-input 2-output integrated silicon PBS has been demonstrated for the first time with a record bandwidth of over 150 nm and less than -10 dB crosstalk

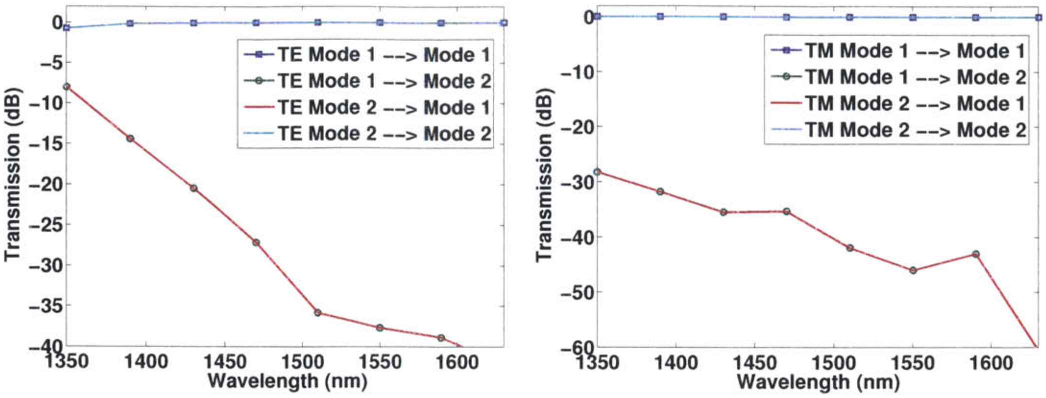

(a) TE response

(b) TM response

Figure 3-14: (a) EME simulation of TE responses of the PBS shown in Fig. 3-11 for different wavelengths with L_3 = 150 *mu*m. (b) EME simulation of TM response of the PBS shown in Fig. 3-11 for different wavelengths with L_3 = 150 *mu*m.

for both TE and TM modes. The design was fabricated on a CMOS-compatible SOI platform. The PBS has also achieved a compact footprint of ~2520 μm^2, which is still many orders smaller than the off-chip counterparts of PBS. Although the compact PBS represents a single component within an on-chip system, it can be used to form on-chip polarization diversity or insensitive networks, interferometers, spectrometers, optical coherence tomography, microscopy and imaging systems. Besides, improvements and further designs were discussed which may potentially increase the bandwidth of working wavelength, shorten the structure and improve extinction ratio.

Chapter 4

Waveguide Crossing

Planar fabrication has a unavoidable problem as the crossing between waveguide. Without suitable waveguide crossing, the design is limited to a certain topology that impairs the scalability of an optical system. Two factors are quite important to the performance of the waveguide crossing, namely insertion loss and cross-talk level. For a waveguide crossing to work in practical optical systems, negligible insertion loss and low cross-talk level are required. Different designs have been demonstrated using different methods such as micro-ring assisted crossing [51], 3D or vertical coupling assisted crossing [52, 53], multi-mode interference crossing [54, 55] or adiabatic crossing [56] which combines two adiabatic 3dB coupler to achieve the goal. Devices such as micro-ring assisted crossing have the problem associated with narrow bandwidth and limited FSR of the ring. Beside, the fabrication variations of the micro-ring also make the wavelength working range unfixed. But with thermal tuning and active fast speed control, they can be utilized as wavelength selective switches. Options like 3D or vertical coupling assisted crossing require additional mask layer of other materials which add more complexity to the fabrication process. In that case, more accurate control on mask alignment is required. Multi-mode interference crossing structure is a good choice for current silicon photonics. It has a small insertion loss number and cross-talk level. System level implementation [39] has used it as the basic component and it performed well in that demonstration. However, for systems that require smaller cross-talk level, the structure lacks a way to further improve the performance.

The last option, the adiabatic waveguide crossing is the topic of this chapter. Since it is an adiabatic structure, with suitable dimension of the waveguide cross sections, by slowly varying the size of the structures along the device, higher performance crossing can be achieved in this way at the cost of large device size.

4.1 Design

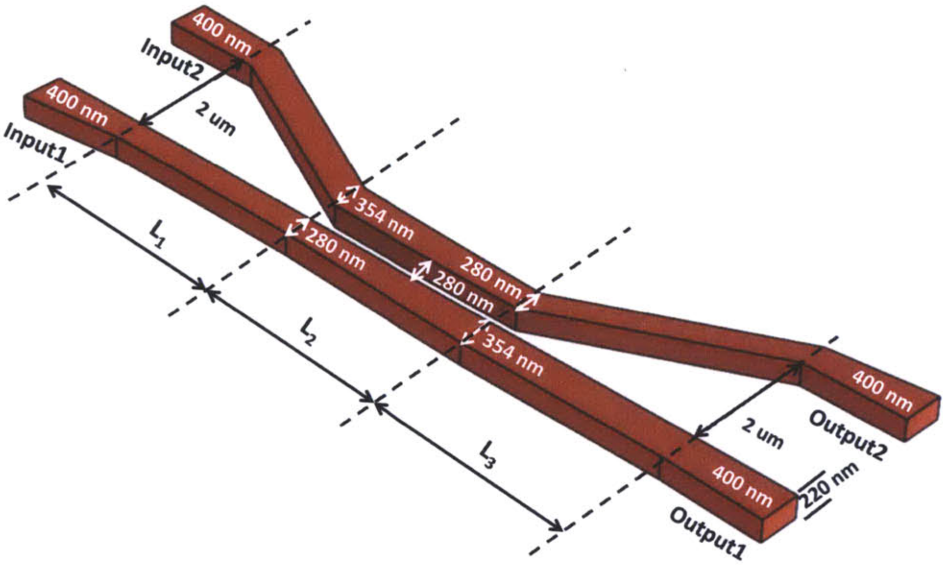

Figure 4-1: Full schematic of the crossing designed. It consists of the adaptor part and the center mode evolution part.

Fig. 4-1 shows the full schematic of the crossing structure designed. The sizes of the waveguides are 354 nm (big) and 280 nm (small) respectively. This ensures a well-separated effective indices for the first two TE modes. The structure starts with two waveguides of width 400 nm and a separation of 2 μm to ensure negligible coupling between the two waveguides before they get tapered down to other sizes. The two waveguides then get tapered to 354 nm and 280 nm separately while maintaining the gap size of 2 μm. After that, the two waveguides start approaching each other and stop with a gap of 280 nm. Then the main part of the crossing starts. The waveguide with width 354 nm is tapered to 280 nm while the 280 nm one gets tapered to 354 nm. The gap between the two waveguides stays the same during this transition. After this step, two waveguides get separated again and tapered to normal single mode waveguides of width 400 nm.

4.2 Simulation

The lengths of L_1 and L_3 are chosen to be 200 *mu*m as a conservative number for preparing the eigenmodes input for L_2 part. The critical part of the device is the L_2 part of the structure, where the eigenmodes of the structure evolve so that the main power of the modes exchange in between the waveguides. To determine the length of L_2 part, simulation tools such as eigen mode expansion and FDTD method are used.

4.2.1 Mode Solver Method

The TE modes profiles and effective indices curve along the L_1, L_2 and L_3 parts are shown in Fig. 4-2. From the eigenmode point of view, the two TE modes first hybrid with each other through adiabatic change and when they are separated again, the main power of the modes shifts ports so as to achieve the function as a crossing. It can also be explained by the effective indices curve (shown in Fig. 4-2(c). Under adiabatic limit, the modes will evolve along the effective indices curve. Since the structure we designed is quite long, it satisfies the adiabatic limit. In that sense, the first order mode will stay as the first order mode along the structure. So the mode concentrated in Input1 (Input2) will successfully evolve to mode concentrated in Output2 (Output1) (shown in Fig. 4-2(b)).

4.2.2 Eigenmode Expansion (EME) Method

So far, the way to choose the right length to achieve adiabatic limit has not been discussed yet. The method used here is EME method. By setting a certain extinction ratio, the lower limit of the length of the structure can be fixed.

For certain wavelength, by scanning the length of the structure, the cross-talk

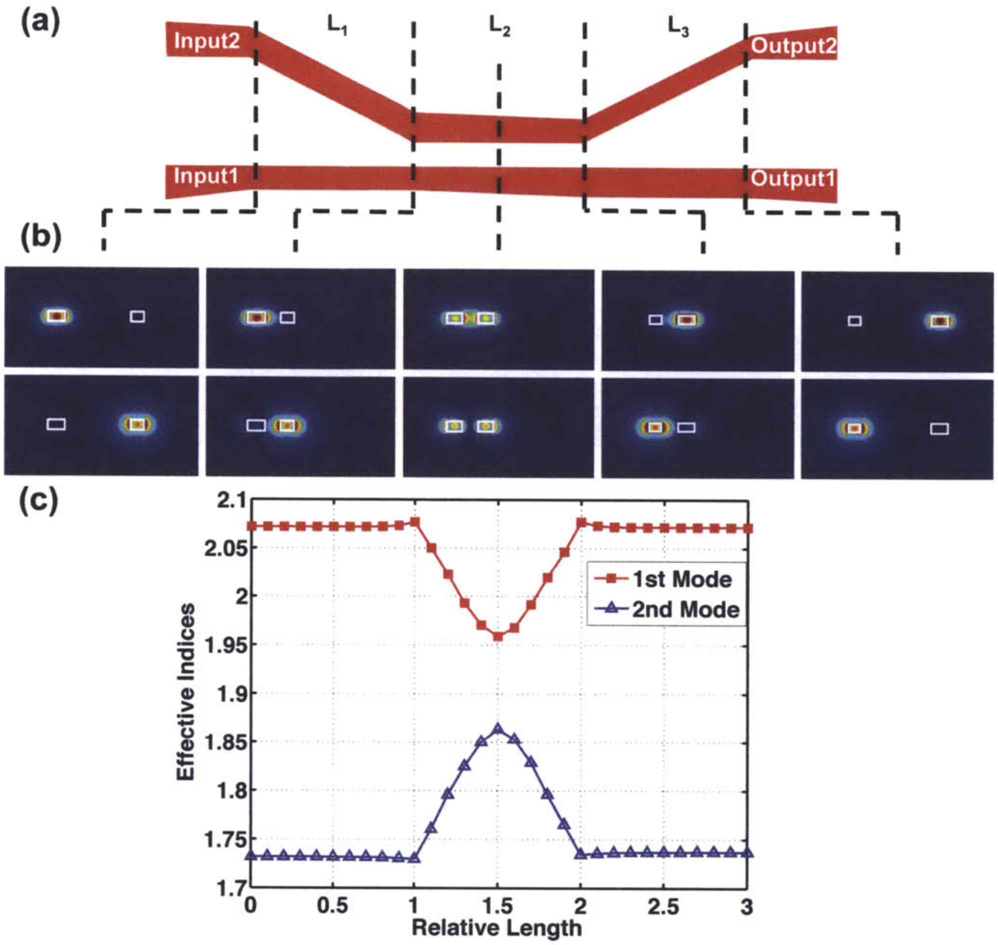

Figure 4-2: (a) Top view of the schematic of the waveguide crossing structure. $L_1 = 200\mu m$, $L_2 = 200\mu m$ and $L_3 = 200\mu m$. (b) Eigenmodes of the cross sections marked by the dotted lines. The top figures are the first order modes and the bottom figures correspond to second order modes. (c) The effective indices curves of the eigenmodes from the beginning of L_1 part to the end of the L_3 part.

can be extracted which helps us select the right length of the structure to meet the adiabatic limit. The EME simulation results are shown in Fig. 4-3 for wavelength of 1550 nm. Since for different wavelengths, the eigenmode profiles are different, which in turn, changes the property of the modes. By sweeping the wavelength and calculating the response, the bandwidth of the structure can be extracted. Normally, wavelengths around 1550 nm are the wavelength range we are interested in. So calculation for 1550 nm is first performed. Then, by doubling the length of the taper

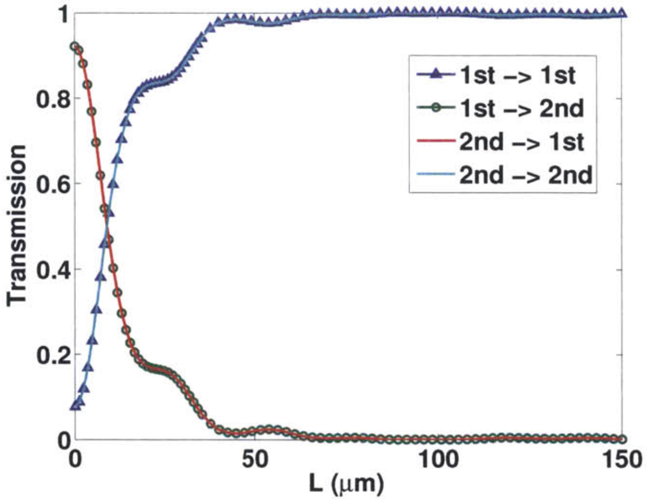

Figure 4-3: EME result of the L_2 part of the waveguide crossing designed in the previous section for wavelength 1550 nm for different kinds of length.

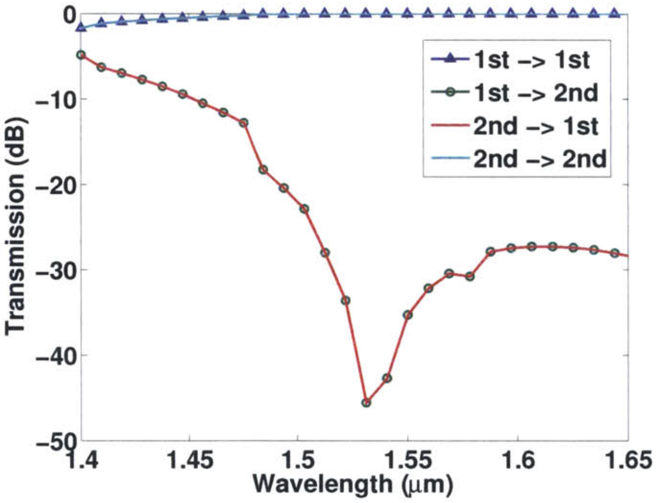

Figure 4-4: Mode conversions versus wavelength for a middle part of 100 μm.

structure or more, the performance of the structure can be ensured and it will have a pretty broad bandwidth. For here, we select a L_2 length of 100 μm and scan the wavelength. The result is shown in Fig. 4-4. By setting -20dB cross-talk level as the criteria for good performance, the device designed has a working region from 1.5 μm to 1.65 μm, covering C band (1530-1565 nm), L band (1565-1625), and part of S band (1460-1530 nm) and U band (1625-1675 nm). This proves that it has a high performance and is suitable for using in the realistic communications.

4.2.3 FDTD Method

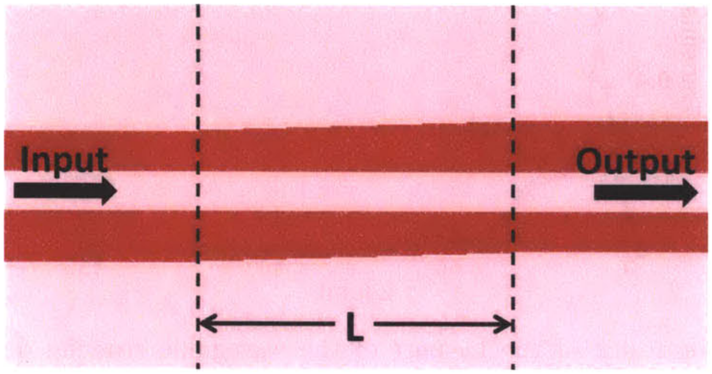

Figure 4-5: Waveguide crossing structure for FDTD simulation.

To further justify the above results got from effective index calculation and EME method, a rigorous Finite Difference Time Domain (FDTD) method is performed on the design. The FDTD simulation structure is shown in Fig. 4-5. The grid size used for FDTD is 10 nm in the lateral direction of the cross section of the structure while the vertical and the direction along the propagation are using 20 nm grid size. For numerical simulation, the input widths of the waveguides are rounded to be 360 nm and 280 nm separately. Eigenmodes of the structure are sent in from the left side of the device and propagate from left to right. By putting a flux monitor at the end of the transition region, the flux is recorded and fourier transform is used to extract the response in frequency domain. The output mode is then compared to the eigenmodes of the output cross-section using mode overlap method. In this way, the mode conversion coefficients can be extracted. The FDTD results are shown in Fig. 4-6.

The FDTD results show good agreement with the EME simulation, which solidifies the EME method. Usually, the FDTD simulation takes longer time compared to EME method. The advantage of the EME method is that it is easy to calculate different length of the structure after finishing one round of simulation of a set of modes.

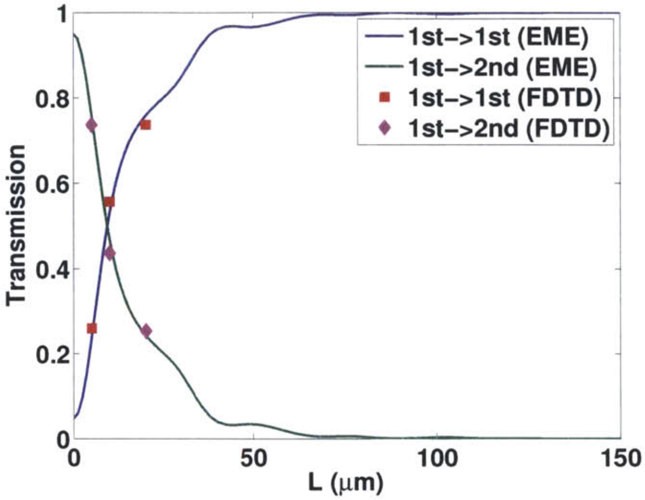

Figure 4-6: FDTD and EME simulation comparison.

Both FDTD and EME methods have their own numerical errors which limit the accuracy of the results. The simulation result of the FDTD simulation used in our group can be quite accurate down to 0.01% or -40dB and becomes less accurate below that. The weakness of EME method is that it cannot include all the modes of a structure, which will require infinite amount of computation resources. Thus, it may not give a right loss number.

4.3 Experimental Characterization

The fabricated device was coupled to laser source and power meter by lensed fiber on both ends. A polarization controller was used for manipulating the input polarization to the waveguide. The input polarization was tested by a nearby micro-ring resonator structure to make sure it is TE polarized for certain wavelength range.

Fig. 4-7 showed the experimental results measured for the waveguide crossing designed. The extinction ratio maintained more than 10 dB for a wide range of wavelength. However, the input polarization is not pure TE for all of the wavelength measured. Due to that, the extinction ratio became quite bad for smaller wavelengths. By adjusting the polarization accurately, the working range of the device can be

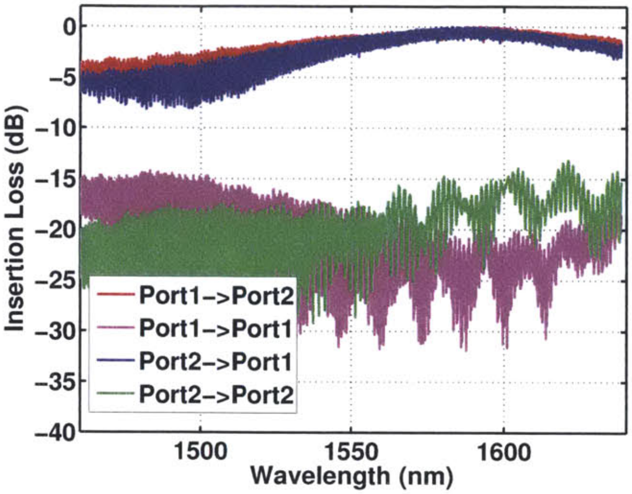

Figure 4-7: The insertion loss response for the waveguide crossing structure designed. The input polarization of the light is set to be TE mode.

further extended.

4.4 Summary

In this chapter, a silicon based adiabatic waveguide crossing is demonstrated which has a bandwidth of over 100nm with the cross-talk level less than -10dB. Both simulation and experiments results are presented. The EME method is justified using rigorous FDTD simulation. Though the experimental results does not agree well with simulation results which indicates a rather lower cross-talk level, the performance is still acceptable for certain usage. The cross-talk level can be improved by setting larger gap size between the two input waveguides and two output waveguides. Besides, extending the length of the whole structure will also help the extinction ratio. Further optimization can be done to reduce the overall size by selecting different widths of the structure.

Chapter 5

Even Dropping Optical Bus System

Bus structure has been employed widely in the electronic communication. However, a robust optical bus configuration has not been proposed or realized. In this chapter, a robust optical bus configuration is proposed which is easy to be incorporated into large communication systems.

5.1 Background information

For on-chip devices, from communication channel prospect, a low loss, high uniform power splitter is desirable. Many efforts have been devoted to the splitter designs [57, 58, 59]. It can be classified as multi-mode interference (MMI) device [59], Y-junction device [57, 58, 24] or adiabatic device [60]. The performance of the device is getting better over the time. However, since those devices designed are all broadband devices, it will require additional filters to make it work for wavelength division multiplexing applications. Wavelength selective power splitter has been proposed and demonstrated in large ring systems with multiple drop ports [61, 62]. But the drawback of single large ring structure is that the ring needs to be big enough in size to sustain a useful number of drop ports, which in turn, shrink the free spectral range (FSR) of the device, making it hard to support large amount of channels. Besides, the number of ports of this kind of structure needs to balance both FSR and bandwidth of each channel to avoid cross-talk. In that case, each channel may not have the capacity to carry high speed data rate. Thus a new structure needs to be implemented to take the advantage WDM of optical systems. Small micro-ring is a suitable candidate. By shrinking the size of micro-ring (e.g. radius of 2 μm), large FSR (>50nm) [63] can be achieved. To solve the problem for even dropping of energy for multiple ports, a partial-drop filter can be implemented with quite different couplings between bus waveguide to ring and ring to drop waveguide. In this way, both large FSR and energy distribution between different ports can be achieved.

5.2 Adiabatic Ring with Integrated Heater

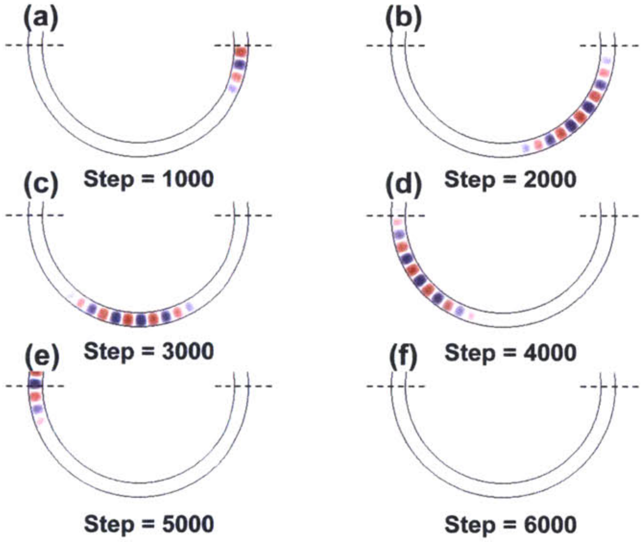

Figure 5-1: FDTD simulation of the mode propagation for a regular ring with uniform width of 400 nm and radius of 3μm.

To implement the optical bus system, an adiabatic ring resonator (ARR) [64] is used as the basic component of the system. The adiabatic ring starts with small width and gradually change its width to a larger number along the propagation. Since the change in the width along the ring is slow enough, when fundamental mode of the ring is excited, the mode will stay in the fundamental mode along the propagation of light. The FDTD propagation figures of a regular 3μm radius ring with 400 nm×220 nm in width and height and an adiabatic ring with 3 μm radius, initial width of 400

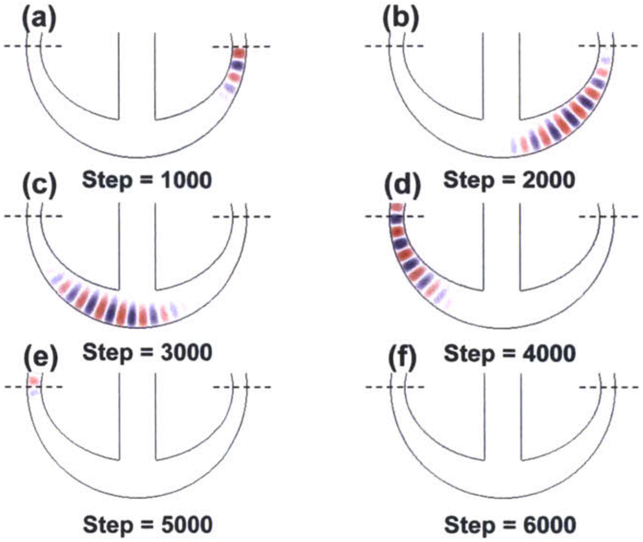

Figure 5-2: FDTD simulation of the mode propagation for an adiabatic ring with a start width of 400 nm and end width of 1000nm and outer radius of 3μm. The tether width assumed here is 1 μm.

nm and end width of 1000 nm are shown in Fig. 5-1 and Fig. 5-2 separately.

It can be easily seen from the figure that the loss introduced by the tether inserted into the adiabatic ring structure is quite small. Thus, by splitting the tether into two smaller tethers, doping the tether with large dose and doping the ring with small dose, an electric circuit loop can be formed which can act as an integrated heater. The full scheme of the tunable adiabatic resonator is shown in Fig. 5-3. Compared to traditional heater which put metals directly on top of the SiO_2, the integrated heater has the advantages of strong effect and less power consumption while introducing non-harmful loss.

The choice of 1 μm end width of the adiabatic ring comes from rigorous FDTD simulation. Assuming the tether width to be 1 μm, which is a reasonable number from fabrication point of view, by varying the end width size of the ring, different transmission level and loss number can be extracted.

The FDTD simulation for different sizes of end width of the adiabatic ring for both case (with/without tether) is shown in Fig. 5-4. The figures clearly show that 1 μm is around the optimal point of the adiabatic structure. For larger big width

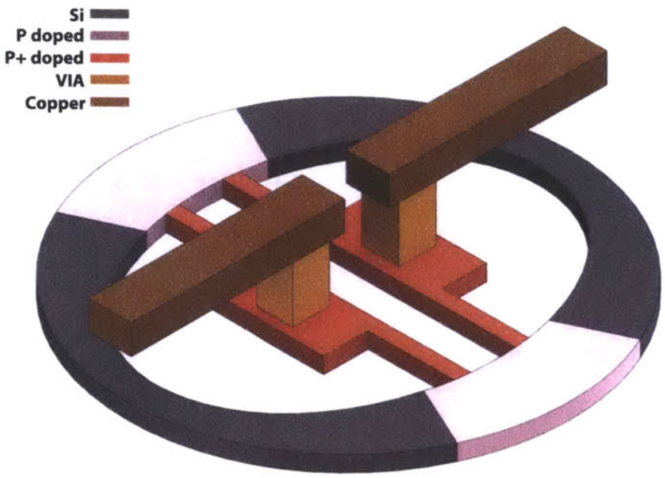

Figure 5-3: Schematic of a tunable adiabatic resonator. Different colors represent different region of materials. P represents p doping with doping level around 1e18/cm^3 while P+ represents p doping with doping level around 1e20/cm^3.

of the adiabatic rings, the FDTD figures looks similar for the cases of with and without tether, which indicates that the tether only has big effect on where the width is relatively small that the tether will touch the modes. For larger end width, the change from input width of 400 nm to that width will not meet the adiabatic condition which will cause a mutual coupling from fundamental mode to second order mode. Since the quality factor of second order mode is far lower than the first order mode, extra loss will be introduced to the adiabatic structure.

For detailed analysis, the propagation loss number of the simulations are shown in Fig. 5-5. It agrees with our observation on the FDTD simulation figures. The loss becomes identical to each other for with and without tether. The loss for that case is from the non-adiabatic transition since with the increase of speed of width change, the structures become less adiabatic which causes a cross coupling between the fundamental mode excited from the bus waveguide and the high order modes in the large width part of the adiabatic ring. Since the high order modes have relatively large areas and less confinement, the quality factor is lower than the fundamental, causing large loss for that case.

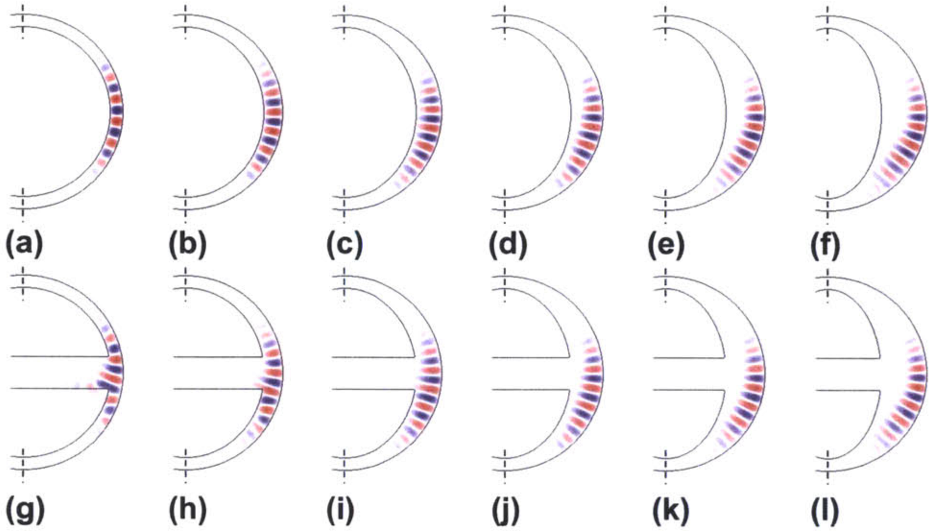

Figure 5-4: FDTD simulation of the adiabatic ring for different widths of the big part of the ring and for cases that tether exists or not. From (a)-(f), the end widths of the adiabatic ring are 400 nm, 600 nm, 800 nm, 1000 nm, 1200 nm, 1400 nm. From (g)-(f), the end widths of the adiabatic ring with tether are 400 nm, 600 nm, 800 nm, 1000 nm, 1200 nm, 1400 nm. The tether width used in the case of (g)-(f) is 1μm.

5.3 Partial Drop Filter

For traditional filter, the drop port will collect most of the power for the pass band. However, for an optical bus, this kind of filter is not useful since it can not distribute the energy into several destinations. A partial drop filter is utilized to distribute the energy. This kind of filter consists of a ring resonator coupled to bus and drop waveguide with different strengthes of coupling. In this way, along the bus waveguide, power sent in for the resonance of the ring resonator will be partially dropped to the drop port, leaving part of the power for that wavelength in the bus waveguide for further steps. The scheme for the partial drop filter is shown in Fig. 5-6(a). By changing the bus to ring coupling strength t_1 and drop to ring coupling strength t_2, various bandwidth and drop power (peak value) can be achieved. Fig. 5-6(b)-(e) list the filter response for different coupling number t_1 and t_2. Using this property of partial drop filter, by tuning the coupling number t_1 and t_2 and cascading multiple partial drop filters along the bus waveguide, equal power and bandwidth in the multiple drop

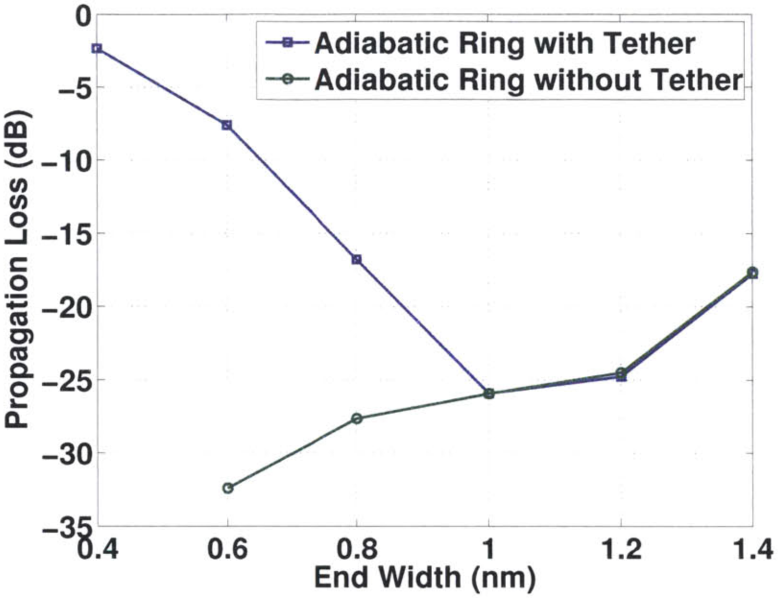

Figure 5-5: FDTD simulation on the propagation loss of adiabatic ring with tether size of 1μm versus different end width sizes. The data are normalized to regular ring propagation data with width of 400 nm.

ports can be achieved.

The notations used in this chapter are shown in Fig. 5-7. For each node, the thru port power coefficient is T_k and the drop port power coefficient is D_k. Since the partial drop filter is almost lossless, $T_k + D_k = 1$. The distance between each node can be quite large, making the propagation loss $a_T^{(k)}$ not negligible. But with the improvement on material property and fabrication technique, the loss of the silicon material is now 2.7dB/m [65]. Thus, $a_T^{(k)}$ is close to 1. It can be replaced by the average loss per node a_T as

$$a_T^k \simeq a_T \equiv \sqrt[N]{\prod_{k=0}^{N-1} a_T^k} \tag{5.1}$$

In between the drop port and the detector, the propagation loss is denoted as a_D which is identical for all of the drop ports. The power from each thru port is denoted as $P_N^{(T)}$. For the completeness of the notation, $P_0^{(T)}$ is used as the input power. To

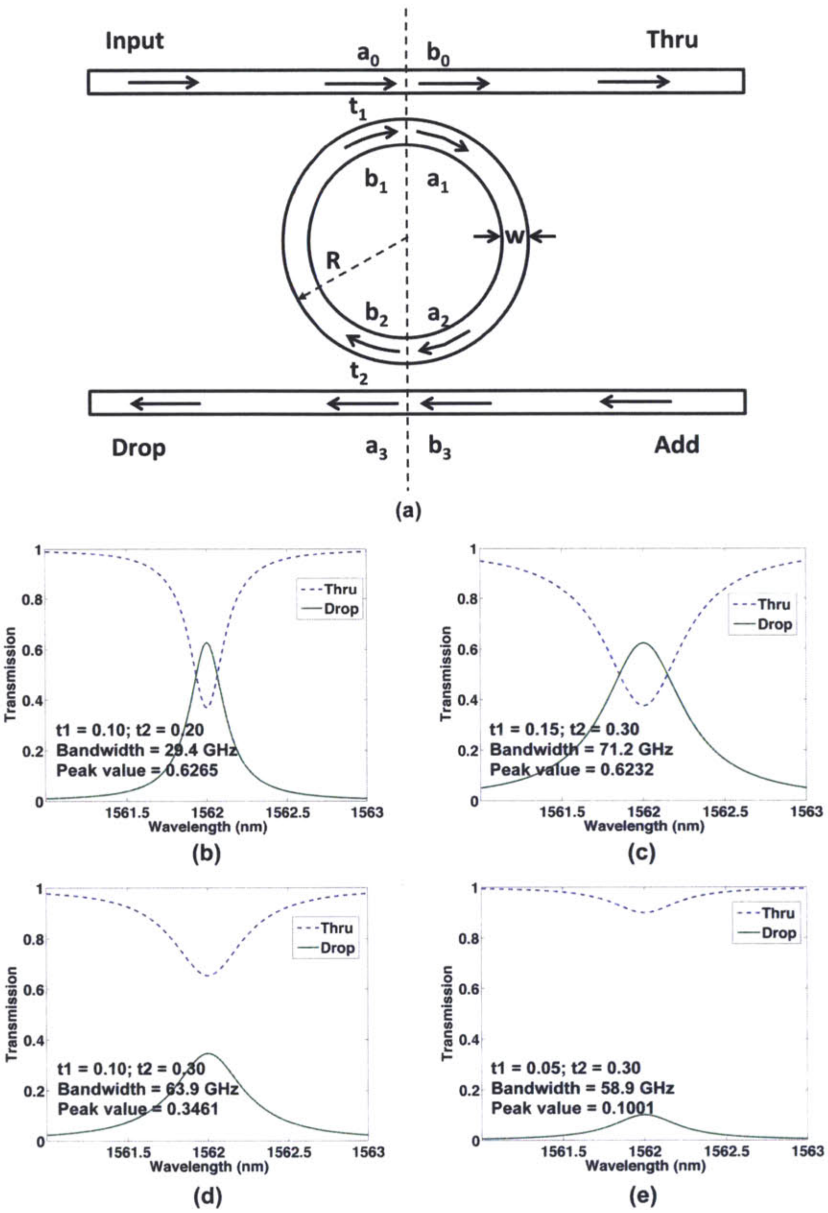

Figure 5-6: (a) Schematic of partial drop filter. (b)-(e) Partial drop filter for cases (b) $t_1 = 0.10$, $t_2 = 0.20$. (c) $t_1 = 0.15$, $t_2 = 0.30$. (d) $t_1 = 0.10$, $t_2 = 0.30$. (e) $t_1 = 0.05$, $t_2 = 0.30$.

analyze the response of the system in frequency domain, $P_0^{(T)}$ is set to 1 for all of the wavelengths. For complete dropping of the power, $P_N^{(T)}$ is 0 for the resonant wavelength of the filter. The power collected by the detector is denoted as $P_N^{(D)}$. The

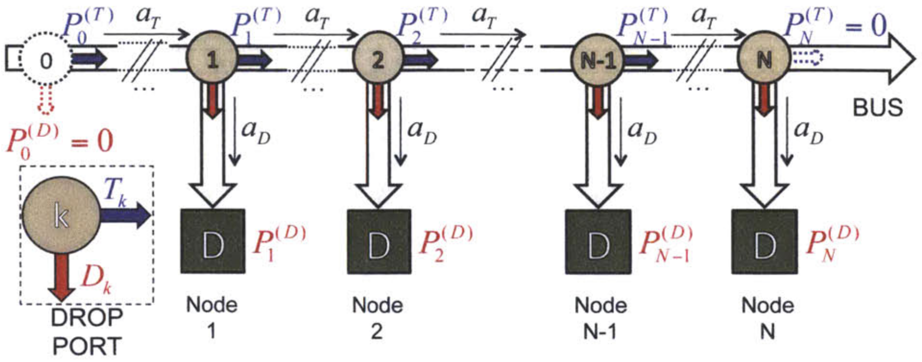

Figure 5-7: Schematic of the cascaded partial drop system. The input signal at a fixed wavelength is distributed to different detectors associated to different nodes. All shown drop ports select the same wavelength but, in general, with different drop coefficients D_k. Figure created by Dr. Matteo Cherchi.

relations between $P_k^{(T)}$, $P_k^{(D)}$ and $P_0^{(T)}$ can be written as

$$\begin{aligned} P_k^{(T)} &= P_0^{(T)} \cdot (a_T)^k \cdot \prod_{i=1}^{k} T_i \\ P_k^{(D)} &= P_{k-1}^{(T)} \cdot a_T \cdot a_D \cdot D_k = P_0^{(T)} \cdot a_D \cdot D_k \cdot (a_T)^k \cdot \prod_{i=1}^{k-1} T_{k-1} \end{aligned} \tag{5.2}$$

The total loss of the power of the system can be expressed as

$$P_{Loss}^{(T)} \equiv \sum_{k=0}^{N-1} (1 - a_T) P_k^{(T)} \tag{5.3}$$

So the power collected by each detector should be

$$P_k^{(D)} = \frac{a_D}{N}(P_0^{(T)} - \sum_{k=0}^{N-1} (1 - a_T) P_k^{(T)}) \tag{5.4}$$

By combining Eqn. 5.2 and Eqn. 5.4 together, D_k can be calculated by induction.

$$D_k = \frac{a_T^{N-k}(1 - a_T)}{1 - a_T^N - a_T^{N-k+1}(1 - a_T^{k-1})} \tag{5.5}$$

In the ideal case, $a_T = 1$, Eqn. 5.5 will be reduced to

$$D_k^{Ideal} \equiv \lim_{a_T \to 1} D_k = \frac{1}{N - k + 1} \tag{5.6}$$

For different loss number a_T, the values of D_k is quite different. Fig. 5-8 shows D_k values in the case of 64 drops with different loss numbers of 0 dB, 0.1 dB and 0.2 dB per node. The loss number has a significant lowering effect for the drop ports with smaller numbers associated.

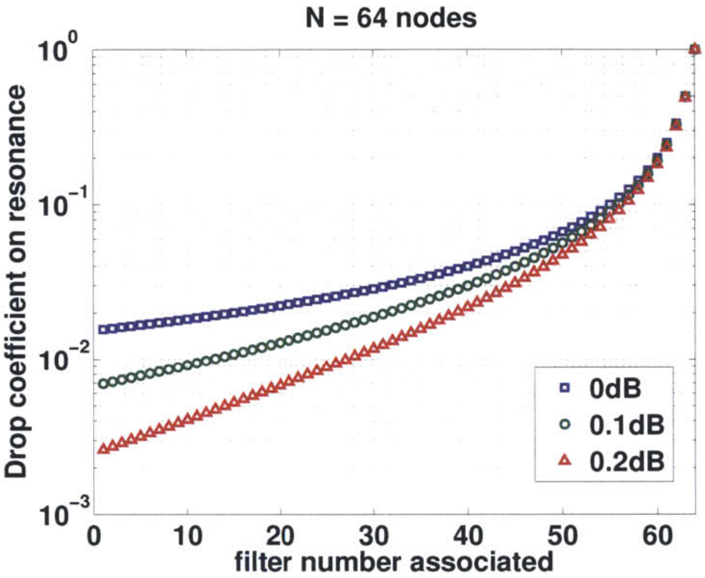

Figure 5-8: Drop coefficients D_k to evenly drop a given signal to 64 nodes for different loss numbers of 0 dB, 0.1 dB and 0.2 dB per node.

Besides, from Fig. 5-8, the drop coefficients increase slowly at first for partial drop filters with small numbers and increase dramatically for last few filters. Comparing the cases of 0 dB and 0.2 dB loss per node, it can be found that D_1s are different by almost an order of magnitude, which indicates that it is quite sensitive to propagation loss for large-node-number partial drop systems.

D_k only deals with the ratio of the power dropped for resonant wavelengths. For filter design, bandwidth of the filter is another issue to be considered. For a lossless case of the partial drop filter, D_k sets a constraint as

$$D_k = \frac{C_1 C_2}{(1 - \sqrt{1 - C_1}\sqrt{1 - C_2})^2} \tag{5.7}$$

where C_1 and C_2 are the power coupling coefficients from the bus waveguide to ring and ring to drop waveguide. For complete drop at the last stage, the condition is

$C_1 = C_2 \equiv C_0$.

The other constraint is given by the bandwidth requirement of the partial drop filter. Since it is a cascading system and all of the filters work for the same range of wavelengths, the previous stages will affect the following stages. Definite expressions for C_1s and C_2s for each stage are not provided here. This process can be easily implemented numerically by setting D_k and varying C_1 and C_2 accordingly. For the above calculation, coupling induced loss and loss inside of the ring (e.g. bending, roughness and absorption) are neglected. However, in real case, these losses do exist and can be modeled as a fraction of the power coupling coefficient C_1. In Eqn. 5.7, C_1 and C_2 are exchangeable to each other. Two solutions for C_1 are expected. To minimize the loss, a small value of C_1 and large value of C_2 is preferable.

Here, a four-drop-port evenly dropping optical bus is analyzed as an example. For normal use of filter, bandwidth of 50GHz is chosen as the bandwidth requirement. First, assuming lossless character for the optical bus system, the first partial drop filter will have a peak value of 0.25 and bandwidth of 50GHz. The search for the proper values of C_1 and C_2 to satisfy this requirement can be easily implemented numerically.

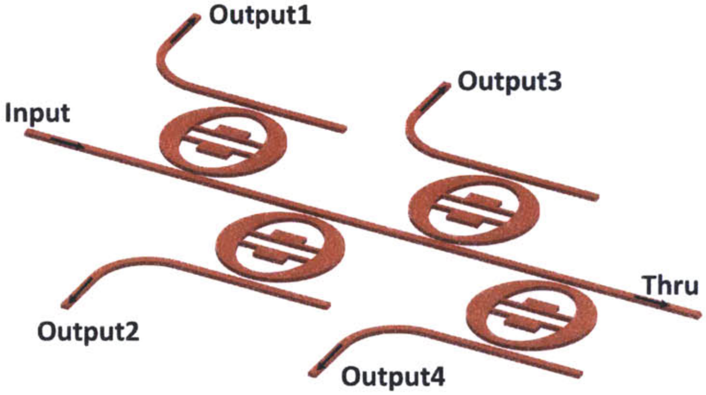

Figure 5-9: Four-drop-port evenly dropping optical bus structure.

The design structure of for optical bus is shown in Fig. 5-9. It consists of 4 cascaded partial drop filters implemented using adiabatic ring design discussed in the previous section. Based on experiment results from Dr. Hosseini, the parameters

Ring Propagation Loss (α)	2.5624/cm
Free Spectral Range (FSR)	34.16 nm
Ring Small Width	400 nm
Ring Big Width	1000 nm
Resonant Wavelength	1554.0 nm
Mode Order	27
Straight Waveguide Loss	2 dB/cm
Distance between Stages	20 μm

Table 5.1: Adiabatic ring parameters.

$C_1^{(1)}$	$C_1^{(2)}$	$C_1^{(3)}$	$C_1^{(4)}$
0.00444	0.00530	0.00697	0.0168
$C_2^{(1)}$	$C_2^{(2)}$	$C_2^{(3)}$	$C_2^{(4)}$
0.060	0.0512	0.0400	0.0168

Table 5.2: $C_1^{(k)}$ and $C_1^{(k)}$ values for a four-drop-port evenly dropping optical bus system of 50GHz using basic parameters from Table 5.1.

for the adiabatic ring are listed in Table 5.1. The search for the C_1 and C_2 for each stage is based on optimization. First, a wide-band signal of constant power is sent into the structure. The values for D_k, C_1s and C_2s can be roughly determined from the overall response of the structure. Those parameters can be used as guessing parameters. Then by setting a condition for reducing the output differences between 4 drop ports as an optimization parameter, C_1s and C_2s are optimized near the guess values. The $C_1^{(k)}$ and $C_2^{(k)}$ are listed in Table 5.2 and the overall responses for the four drop ports are shown in Fig. 5-10. The designed bandwidths for all of the filters are around 50GHz.

Design parameters for different numbers of drop port are listed in Table 5.3. All of the resonators used here have the same resonant frequency. Since the couplings between the bus waveguide to the ring and ring to drop waveguide are different for each stages, the resonant wavelengths will be different for each stage if the rings used are identical to each other. It is due to the coupling induced wavelength shift. This problem can be solved by slightly tuning the big width part of the adiabatic ring and active thermal tuning by doping the structure. From the FDTD simulation shown in Fig. 5-5, the quality factor of the adiabatic ring is not greatly affected by changing

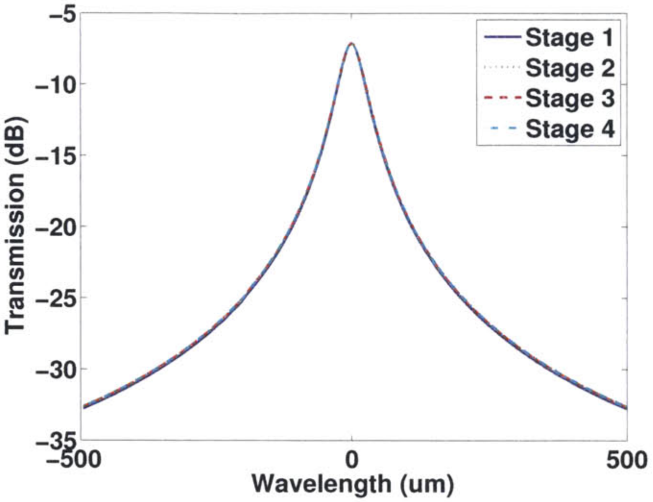

Figure 5-10: Overall response of the four-drop-port evenly dropping optical bus system of a bandwidth of 50GHz.

the big width from 1 μm to 1.1 μm. Besides, since the mode of the adiabatic ring does not see the highly doped region, the extra loss added into the structure due to thermal tuning will not harm the overall response.

(a) Eight-drop-port optical bus of 50 GHz

$C_1^{(1)}$	$C_1^{(2)}$	$C_1^{(3)}$	$C_1^{(4)}$	$C_1^{(5)}$	$C_1^{(6)}$	$C_1^{(7)}$	$C_1^{(8)}$
0.00213	0.00229	0.00250	0.00275	0.00312	0.00370	0.00483	0.01160
$C_2^{(1)}$	$C_2^{(2)}$	$C_2^{(3)}$	$C_2^{(4)}$	$C_2^{(5)}$	$C_2^{(6)}$	$C_2^{(7)}$	$C_2^{(8)}$
0.06200	0.05780	0.05350	0.04800	0.04260	0.03600	0.02780	0.01160

(b) Sixteen-drop-port optical bus of 50 GHz

$C_1^{(1)}$	$C_1^{(2)}$	$C_1^{(3)}$	$C_1^{(4)}$	$C_1^{(5)}$	$C_1^{(6)}$	$C_1^{(7)}$	$C_1^{(8)}$
0.001052	0.001089	0.001130	0.001174	0.001227	0.001285	0.001353	0.001433
$C_1^{(9)}$	$C_1^{(10)}$	$C_1^{(11)}$	$C_1^{(12)}$	$C_1^{(13)}$	$C_1^{(14)}$	$C_1^{(15)}$	$C_1^{(16)}$
0.001530	0.001646	0.001790	0.001985	0.002250	0.002680	0.003500	0.008380
$C_2^{(1)}$	$C_2^{(2)}$	$C_2^{(3)}$	$C_2^{(4)}$	$C_2^{(5)}$	$C_2^{(6)}$	$C_2^{(7)}$	$C_2^{(8)}$
0.06400	0.06198	0.05990	0.05760	0.05540	0.05300	0.05050	0.04782
$C_2^{(9)}$	$C_2^{(10)}$	$C_2^{(11)}$	$C_2^{(12)}$	$C_2^{(13)}$	$C_2^{(14)}$	$C_2^{(15)}$	$C_2^{(16)}$
0.04505	0.04200	0.03870	0.03510	0.03093	0.02613	0.02015	0.00838

Table 5.3: $C_1^{(k)}$ and $C_1^{(k)}$ values for a eight-drop-port and sixteen-drop-port evenly dropping optical bus system of 50GHz using basic parameters from Table 5.1.

5.4 Waveguide to Adiabatic Ring Coupling

With the help of Transfer Matrix (T-Matrix) method, the power coupling numbers $C_1^{(k)}$ and $C_2^{(k)}$ for each stage of the optical bus system are calculated in the previous section. To build a real system, the relation between coupling numbers and waveguide-to-ring gap sizes need to be established.

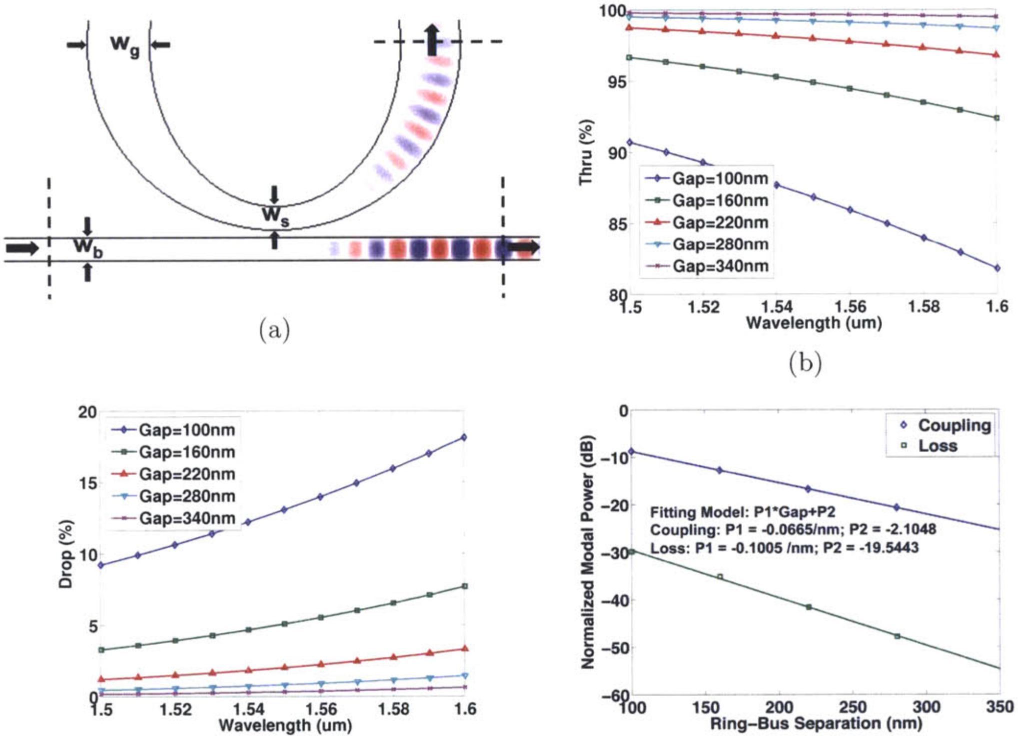

(a) (b) (c) (d)

Figure 5-11: FDTD simulation of the waveguide to adiabatic ring coupling. (a) Schematic of the simulated structure. (b) Thru port; (c) Drop port; (d) Coupling and loss with gap at the wavelength of 1554 nm. The dots are FDTD simulation results and the solid lines are fitting results.

By using FDTD simulation, the waveguide to adiabatic ring coupling is calculated (shown in Fig. 5-11). Since the waveguide to ring system is coupled through evanescent wave coupling, the power coupling coefficient and coupling induced loss are expected to decay exponentially with respect to the waveguide to ring separation. By fitting the calculated data to an exponential model, fitting parameters for calculating coupling and loss with the change of gap size can be extracted. The equation used for fitting is $10\log_{10}(\text{Coupling (or Loss)}) = P1 \times Gap + P2$. Parameters for waveguide to ring power coupling coefficient are $P1 = -0.0665/\text{nm}$ and $P2 = -2.1048$ and the parameters for coupling induced loss are $P1 = -0.1005/\text{nm}$ and $P2 = -19.5443$ for wavelength of 1.554 μm and bus waveguide width of 400 nm. From simulation, only response of wavelengths of 1.55 and 1.56 μm are calculated. The results of wavelength 1.554 μm is calculated through linear interpolation between them. With these parameters, the coupling numbers of the previous section can be converted to gap sizes.

5.5 Coupling Induced Phase Shift of Adiabatic Ring

Without the help of thermal tuning of the resonant wavelength, coupling induced phase shift (CIPS) will cause a drifting of it. A simple explanation of its origin is included in Appendix A.3.3. The relation between CIPS $\Delta\phi$ and wavelength shift $\Delta\lambda$ is

$$\Delta\lambda = \frac{\Delta\phi}{2\pi} FSR \tag{5.8}$$

where FSR is the free spectral range of the adiabatic ring resonator which is 34.16 nm. To get the relation between CIPS and ring-bus separation, FDTD simulation (shown in Fig. 5-12(a)) is used. The structure consists of an adiabatic ring coupled to a straight waveguide. The input mode is launched into the big width part of the adiabatic ring from the top part of the Fig. 5-12(a) and then coupled to the bus waveguide. Three flux monitors are placed on the positions indicated by the dotted lines. The flux monitors are used to collect the input, thru port and drop port flux. An adiabatic ring without bus waveguide is used to extract the phase gained without coupling. The non-coupling phase is subtracted from the overall phases in the coupling systems to extract the CIPS. Fig. 5-12(b) and (c) show the CIPS calculated from the FDTD simulation in linear and log scale separately. Exponential fitting is utilized to extract the fitting parameters. The fitting model is $10 \times \log_{10}(\text{CIPS}) = P1 \times \text{Gap} + P2$ and $P1 = -0.0603/\text{nm}$, $P2 = -5.7948$.

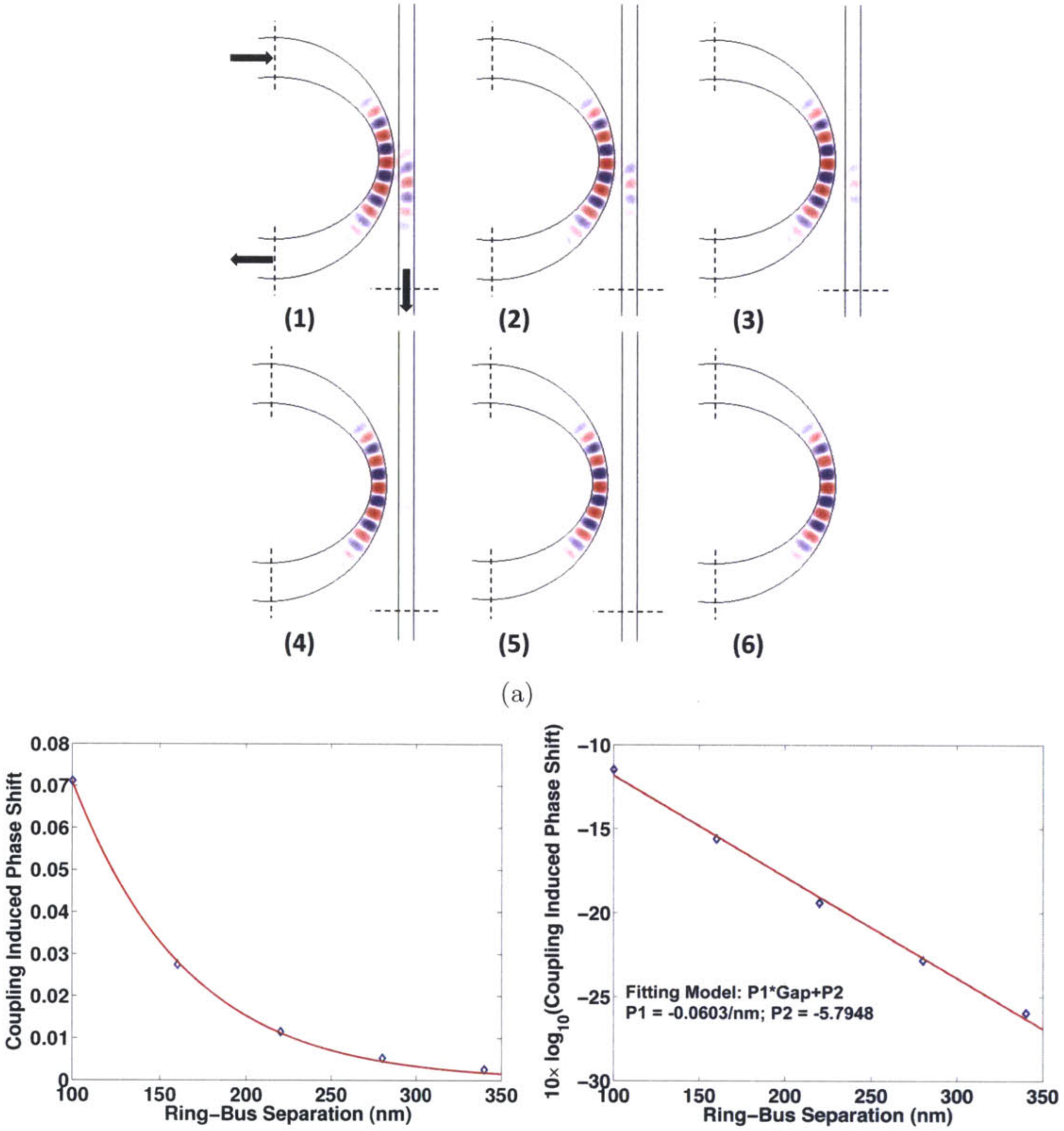

(a)

(b)

(c)

Figure 5-12: FDTD simulation results of the waveguide to adiabatic ring coupling. (a) Wave propagation in adiabatic ring to waveguide coupling FDTD simulation. From (a)-1-5, gap sizes used are 100 nm, 160 nm, 220 nm, 280 nm and 340 nm. (a)-6 is case where there is no bus waveguide. (b) Coupling induced phase shift plotted in linear scale for wavelength 1554 nm. (c) Coupling induced phase shift plotted in log scale for wavelength 1554 nm. The fitting parameters extracted are $P1 = -0.0603/\text{nm}$ and $P2 = -5.7948$.

The total CIPS of a partial drop filter is the sum of the bus-to-ring CIPS and ring-to-drop CIPS. Though the total CIPS differences of each stage are small, the effect of wavelength drifting is not negligible. Besides, wafer thickness non-uniformity and fabrication error can also be sources of wavelength shift. Thus, active thermal tuning is required for the functionality of the system. However, techniques such as phase compensation by changing the size of the big width part of the adiabatic ring can be used to reduce the tuning power. By extracting the phase information from the FDTD simulation performed in Fig. 5-2, the phase shifts for cases of different big width sizes of a half adiabatic ring are shown in Fig. 5-13. The phase for regular half ring with width of 400 nm is set to be zero for comparison. For phase compensation, width range of 1.0 μm to 1.1 μm is used. The expression for calculating the phase shift with the width change can be extracted by linear interpolation between the point 1.0 μm and 1.2 μm. By setting the phase accumulated ($\Delta\phi$) of width 1.0 μm as 0, the phase change expression for a whole adiabatic ring is

$$\Delta\phi = 5.6034/\mu m \times (bW - 1\mu m) \quad (bW \in [1.0\ 1.1]\ \mu m) \tag{5.9}$$

where bW stands for the big width size of the adiabatic ring.

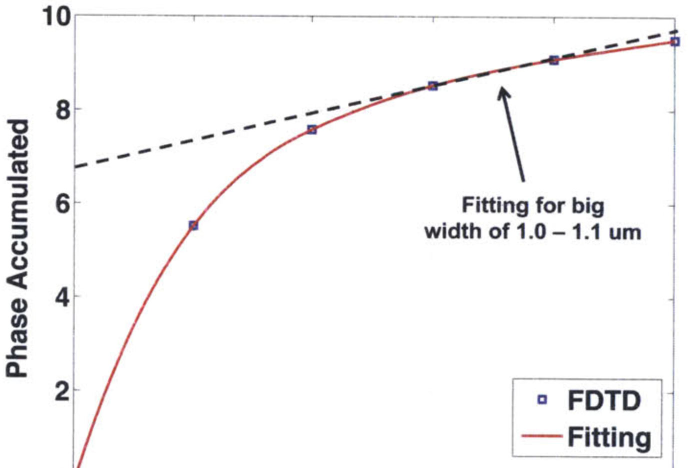

Figure 5-13: Phase shift for a half adiabatic ring of different sizes of big width. The dots are results from FDTD simulation and the solid line is the fitting of the data.

5.6 Experimental Results

This section shows the initial designs and measurement effort of the even dropping optical bus system. At the time of writing this thesis, the rigorous designs using the method talked in the previous sections are still under fabrication. The experimental results presented here all have their own flaws for not considering some of the factors. They are analyzed here for illustration of those factors.

5.6.1 Passive First Order Partial Drop Filter

The first few designs fabricated are multi-stage first order even dropping optical bus. Those structure used the same scheme as shown in Fig. 5-7. The basic ring filter structure has a width of 480 nm, a bus waveguide width of 400 nm and drop waveguide width of 320 nm. The radius of the ring is set to be 2.893 μm to have a resonant wavelength of 1550 nm. The bus-to-ring and drop-to-ring gap sizes of four-drop-port system and sixteen-drop-port system are listed in Table 5.4.

(a) Four-drop-port optical bus parameters

	$C_1^{(1)}$	$C_1^{(2)}$	$C_1^{(3)}$	$C_1^{(4)}$	$C_2^{(1)}$	$C_2^{(2)}$	$C_2^{(3)}$	$C_2^{(4)}$
Gap(nm)	260	230	200	120	115	120	125	120

(b) Sixteen-drop-port optical bus parameters

	$C_1^{(1)}$	$C_1^{(2)}$	$C_1^{(3)}$	$C_1^{(4)}$	$C_1^{(5)}$	$C_1^{(6)}$	$C_1^{(7)}$	$C_1^{(8)}$
Gap(nm)	345	340	335	330	325	320	310	305
	$C_1^{(9)}$	$C_1^{(10)}$	$C_1^{(11)}$	$C_1^{(12)}$	$C_1^{(13)}$	$C_1^{(14)}$	$C_1^{(15)}$	$C_1^{(16)}$
Gap(nm)	300	290	275	265	260	230	200	120
	$C_2^{(1)}$	$C_2^{(2)}$	$C_2^{(3)}$	$C_2^{(4)}$	$C_2^{(5)}$	$C_2^{(6)}$	$C_2^{(7)}$	$C_2^{(8)}$
Gap(nm)	115	115	115	115	115	115	115	115
	$C_2^{(9)}$	$C_2^{(10)}$	$C_2^{(11)}$	$C_2^{(12)}$	$C_2^{(13)}$	$C_2^{(14)}$	$C_2^{(15)}$	$C_2^{(16)}$
Gap(nm)	115	115	115	115	115	120	125	120

Table 5.4: $C_1^{(k)}$ and $C_1^{(k)}$ values for a eight-drop-port and sixteen-drop-port evenly dropping optical bus system of 50GHz using basic parameters from Table 5.1.

The passive optical bus systems responses are shown in Fig. 5-14. Fig. 5-14 (a) shows the response of the four-drop-port optical bus system. The four rings are identical to each other while the gap sizes for coupling to bus and drop are different.

In that case, coupling induced wavelength shift (CIWS) will play an important role for overall response of the system. The result shows that the resonant wavelength for the four drop ports are not identical to each other. The same thing also happens to the sixteen-drop-port optical bus system. The responses tended to be more uniform for drop ports with small numbers (shown in Fig. 5-14 (a)). However, the drifts of the wavelength are still not negligible. They are either due to thickness variations of the material or the CIWS. This, in another way, proved that micro-ring structures need thermal tuning for the accurate control of resonance position.

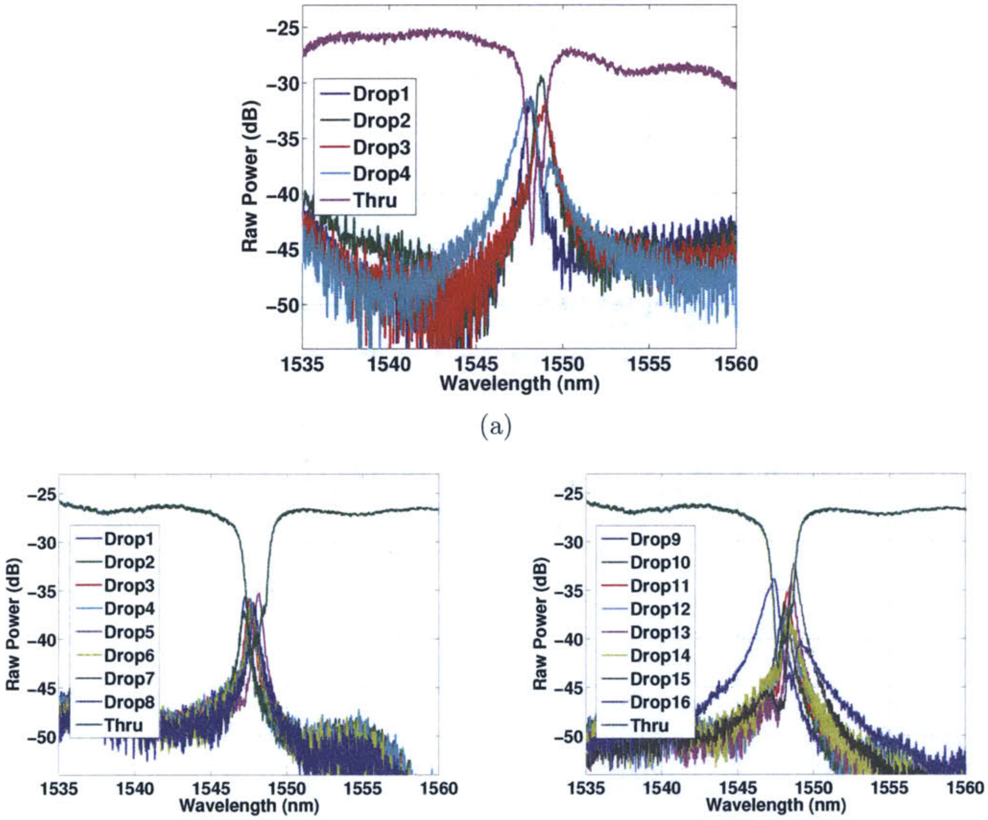

(a)

(b) (c)

Figure 5-14: (a) Insertion loss measurement of a four-drop-port optical bus system. (b) Insertion loss measurement of a sixteen-drop-port optical bus system of ports 1 to 8 and thru port. (c) Insertion loss measurement of a sixteen-drop-port optical bus system of ports 9 to 16 and thru port.

Apart from the wavelength shift of the response, another problem for the last few drop ports of the optical bus systems is also critical. For example, the last drop port (e.g. Drop4 of the four-drop case and Drop16 of the sixteen-drop case) of the system tends to have a larger bandwidth than other drop ports. This can be explained by two aspects of the design. The first is the gap size choice. The last few ports listed in Table 5.4 have smaller ring-to-drop gap sizes. Since the bandwidth of a partial drop filter is dependent on both the bus-to-ring coupling and the ring-to-drop coupling. Smaller ring-to-drop gap size will greatly increase the bandwidth of the partial drop filter. The other reason is related to the cascading scheme. The drop port response of stage N is directly related to the stages of 1 to N-1. For perfectly aligned case, the input signal into stage N is not an uniform signal in wavelength domain. Instead, it is a signal with dips near the resonant wavelengths. Thus, the response of stage N is broader than the uniform input case. But this effect is not obvious when the resonant wavelengths of each stages are not aligned properly.

5.6.2 Multi-Wavelength Broadcasting System

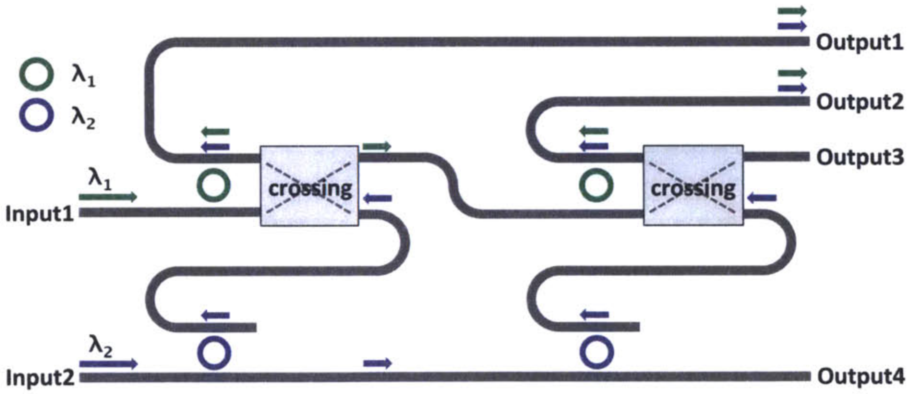

Figure 5-15: Schematic of multi-wavelength broadcasting system.

The structures discussed before are focusing on single wavelength application. By using structures similar to cross-bar switch matrix configuration, multi-wavelength application of the optical bus can be achieved. Here, we demonstrated a two-channel, two-destination broadcast system using two two-drop-port optical bus systems combined with cross-bar configuration.

The waveguide crossing structure used in this structure is the one designed in Chap. 4. The schematic of the designed structure is shown in Fig. 5-15. The input1 port is associated with wavelength λ_1 and input2 port is associated with wavelength λ_2. The signals sent in are evenly dropped by two two-drop-port optical bus systems. With the help of waveguide crossing, two signals with different wavelengths get combined and arrive at the same output ports. In this way, two sources with different wavelength channels will be divided equally and can arrive at two destinations (Output1 and Output2) at the same time. This is similar to traditional broadcasting system where different information sources will use separated frequency channels when they are created by their owners while the customer can get access to all of those frequency channels after their transmission. Additional filters can be added in the output ports to extract the information of certain wavelength channel.

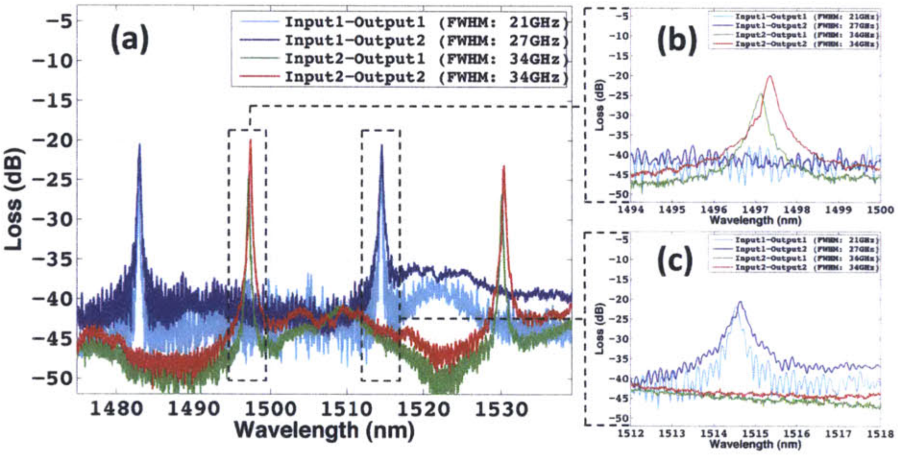

Figure 5-16: (a) Overall insertion loss measurement responses of the multi-wavelength broadcast system. (b) Zoom in of the dotted rectangle indicated on the (a) around wavelength 1497 nm. (c) Zoom in of the dotted rectangle indicated on the (a) around wavelength 1515 nm.

The fabricated device was coupled to fiber using lensed fibers. The insertion loss measurement of Input1 and Input2 to Output1 and Output2 are shown in Fig. 5-16. The figure shows clearly two-channel feature which matches the objective of the structure. However, for real test on data propagation, the wavelength alignment of the two-drop-port optical bus system is still not good enough. Further designs on broadcasting system are implemented using thermally tunable adiabatic ring resonator as the basic building block.

The primary advantage of the broadcasting system scheme is the seamless integration with ring-based cross-bar switches. This way, broadcasting and switching can be built together within a small structure which can manage the data traffic more efficiently.

5.7 Future Prospect

The structures talked in this chapter divide power equally among all those output ports. However, the power cannot be divided into infinite amount of pieces. The powers collected from the output ports need to be above the limit of the detector. To compensate the splitting reduction of the input power, an amplifier needs to be used. The erbium doped Al_2O_3 structure [12, 66] can be used as amplifier and integrated with this pure silicon structure in the state-of-art CMOS foundry.

5.8 Summary

In this chapter, a new implementation of the optical bus system has been rigorously analyzed and initial measurement results on the devices are presented, showing a promising application of the structure. In addition, designs such as thermally tunable adiabatic ring and partial drop filters were explained in detail. Several problems associated with the designs such as wavelength shifting and bandwidth broadening were discussed and solved.

Chapter 6

Conclusions

In this thesis, a system on adiabatic designs for the implementation of polarization manipulation in silicon photonics has been established. Several specific structures of different functions have been achieved such as thin-layer polarization rotator (PR), polarization splitter and rotator (PSR) and two-input two-output full-functional polarization beam splitter (PBS). In addition, original implementation of optical bus using partial drop filters and its application have been investigated and partially realized.

PR and PSR were analyzed in Chapter 2. The specific design of PR was implemented to solve the problem associated with thinner materials in order to be compatible with current CMOS foundry. PSR design was originated from index engineering from the ridged waveguide. This design eased the requirement of ultra small features by adding mask complexity. Both of them were designed using adiabatic method to ensure large operating bandwidth.

Two-input two-output PBS were presented in Chapter 3. The PBS demonstrated is the first two-input two-output PBS ever demonstrated. Though for traditional communication, this PBS can be replaced by its simplified version – polarization splitter. However, for high accurate system such as on-chip quantum computing, this PBS can be a critical component for both quantum state generation and manipulation.

Adiabatic waveguide crossing design was discussed in Chapter 4. Simple as it is, its performance is quite critical for the performance of large optical systems. The structure designed was further used in Chapter 5 for the implementation of an optical broadcasting system.

As the final part of this work, design techniques of a novel even dropping optical bus system have been established in Chapter 5. It includes a thorough analysis about partial drop filter design, adiabatic ring design and phase shifting compensation. The initial experimental results of the designed system were discussed which showed a promising functionality of the system.

Appendix A

FDTD Simulation on Basic Components

There are several different simulation tools on doing photonics designs. They are finite-difference-time-domain (FDTD) simulation, eigen mode expansion (EME) method. FDTD simulation starts with one mode profile of certain wavelength into the structure by a gaussian pulse of finite time. The mode then propagate along the structure and several flux monitors are used for collecting power and doing Fast Fourier Transform (FFT) to get the response in wavelength domain. EME simulation utilizes the transfer matrix (T-matrix) method by dividing a certain structure into several parts and calculate the overall T-matrix between finite modes. The EME has the advantage of fast speed and easier calculation for longer structures while FDTD offers better accuracy. In this appendix, the FDTD simulation tools used in our group and examples on basic components simulation are discussed. This chapter can be used as a manual for future reference in my PHD study.

A.1 Straight Waveguide

A.1.1 Input Modes

For all the simulations performed in this thesis, the refractive indices for materials are 3.48 for silicon and 1.445 for SiO_2. The straight waveguide TE mode shown in Fig. A-1 is solved in mode solver for a silicon waveguide of 400 nm in width and 220 nm in height. This selection is related to the single mode condition of the structure which suppresses the second order TE mode so that the structure maintains single mode to avoid mutual coupling.

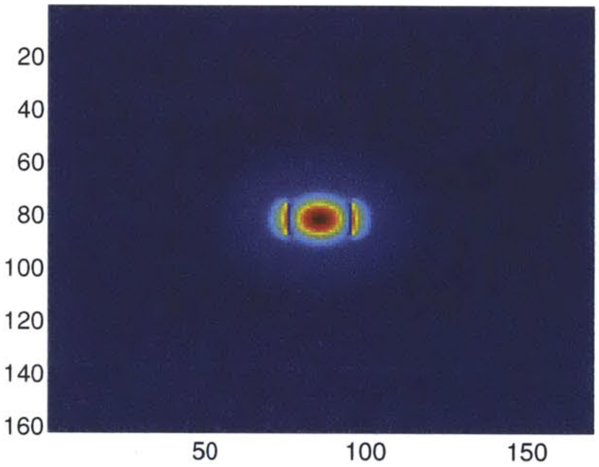

Figure A-1: TE mode of a 400nm×200nm silicon rectangular waveguide.

A.1.2 FDTD simulation

The simplest straight waveguide structure FDTD simulation is shown in Fig. A-2. The mode shown in Fig. A-1 is sent into the structure from left side at the Source Position marked on Fig. A-2(a). Two flux monitors (1 and 2) are used to collect the power for FFT. The propagation of the mode is shown in Fig. A-2(b). There is little power reflected back from the right side of the structure by using PML boundary conditions on all the boundaries of the simulation window.

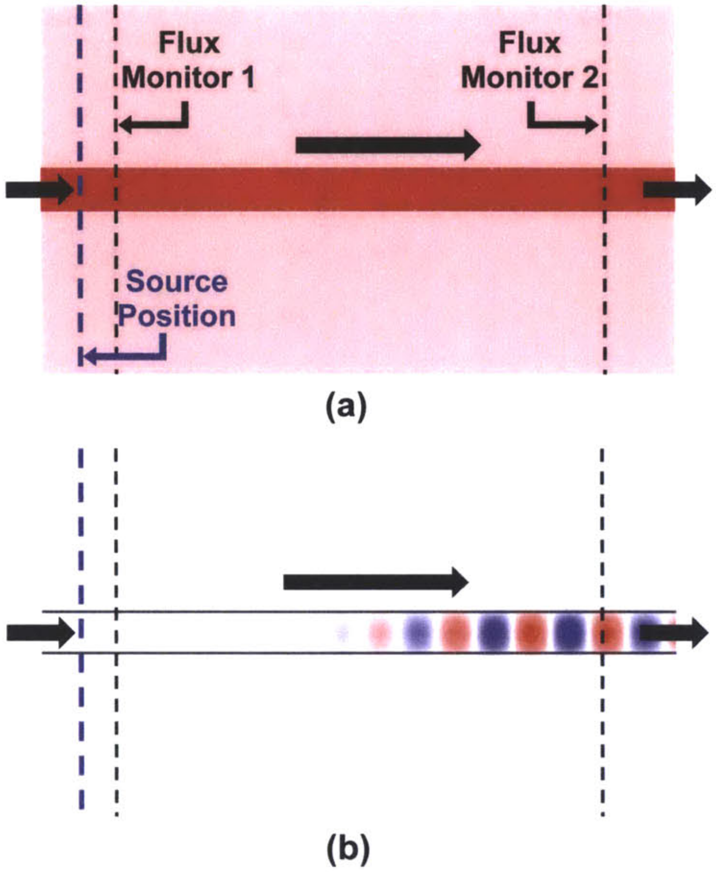

Figure A-2: (a) Simulation structure. The length of the waveguide is 10 μm. The red colored part is silicon while the light colored part is SiO_2. (b) Wave propagation in the waveguide. The right boundary is perfect matching layer (PML) which absorbs the power incident on it.

A.1.3 Mode Overlap Calculation

The data collected from the flux monitors is then converted to data in wavelength domain. By doing mode overlap instead of calculating the power and comparing data gathered from both of the flux monitors, the transmission percentage and phase gained from propagation inside the waveguide can be extracted. Though we only send in the mode of one wavelength into the structure, the finite time of the pulse excites a broad range of wavelengths. Thus, through FFT, information of other wavelengths can also be extracted. The transmission and phase responses of the straight waveguide structure are shown in Fig. A-3. From that, we can see the transmission of the straight

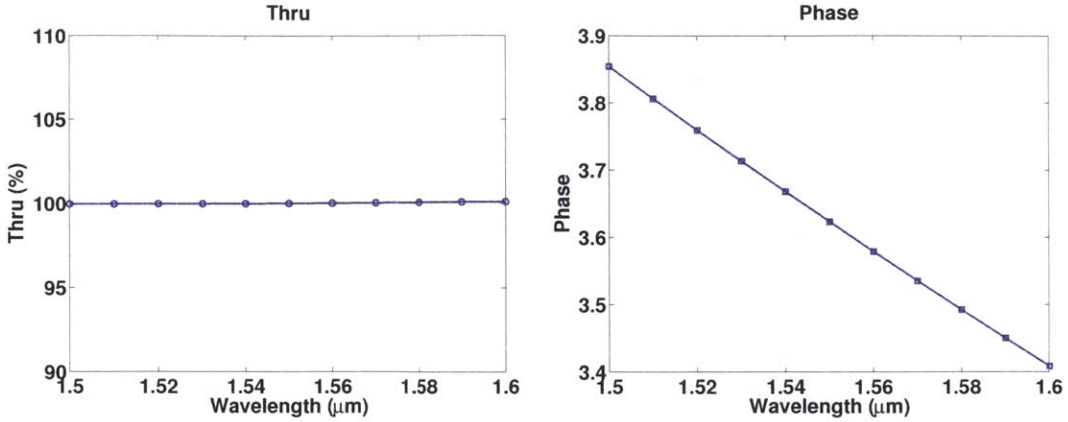

(a) Transmission power response. (b) Transmission phase response.

Figure A-3: (a) Transmission power response. (b) Transmission phase response.

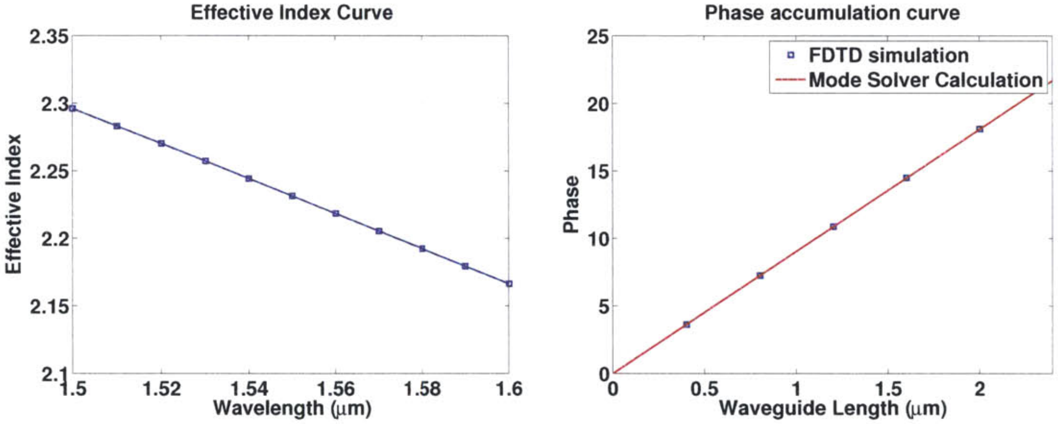

(a) (b)

Figure A-4: (a) Effective index curve of the rectangular waveguide with respect to wavelength. (b) Phase accumulation curve of both FDTD simulation (blue dots) and direct mode effective index calculation from mode solver (red line) for wavelength 1.55 μm.

waveguide is nearly 100% which indicates the reliability of the FDTD simulation code. The phase response is mostly linear with respect to wavelength. This can be explained by the effective index curve of a rectangular waveguide (shown in Fig. A-4(a)). The phase change and wavelength are related by Equation. A.1.

$$\phi = 2\pi \cdot \frac{L \times neff(\lambda)}{\lambda} \tag{A.1}$$

resonant wavelength	1562 nm
Q-factor	1.076×10^6
FSR	31.6 nm

Table A.1: Basic property of a 3 μm radius micro-ring with width of 400 nm and height of 220 nm.

Since the effective index of the TE mode of a rectangular waveguide decreases with the increase of the wavelength, it is expected that the phase accumulation along the propagation will decrease accordingly.

By varying the length of the straight waveguide structure, different accumulated phases are extracted. For certain wavelength, it will be linear with the propagation length. The results in Fig. A-4(b) show that the phase accumulated from calculation of FDTD matches well with the phase calculated directly from mode solver.

A.2 Ring Propagation

Micro-ring resonator is another important component for nano-photonics. For the explanation of FDTD simulation in this appendix, the ring outer-radius is chosen to be 3 μm and the width of the ring is 400 nm. The height is defined by the wafer we use which is 220 nm. The basic properties of the 3μm radius ring are listed in Table A.1. It includes resonant wavelength of 1562 nm, quality factor (Q-factor) of 1.076×10^6, free-spectral range (FSR) of 31.6 nm.

A.2.1 Input Modes

Fig. A-5 shows a typical TE bend mode of a 3 μm radius silicon ring structure for wavelength 1.55 μm. Compared to Fig. A-1, the mode shape is dragged out due to bending, causing extra loss to the bending mode. For 3 μm ring bend mode, the quality factor from bending is 1.076×10^6 which is pretty high compared to other loss mechanism such as material absorption and surface roughness. The FSR is directly related to radius. The smaller the radius, the larger the FSR. For now, the 3 μm ring

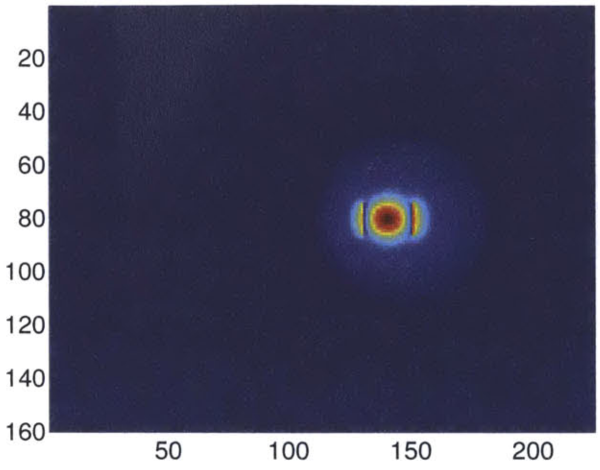

Figure A-5: TE bend mode of a 400nm×220nm rectangular waveguide with 3 μm radius for wavelength 1.55 μm.

has an FSR of 31.6 nm which large enough for supporting large number of channels.

A.2.2 FDTD simulation

The structure depicted in Fig. A-6(a) is a simple ring structure formed from rectangular waveguide of width 400 nm and height of 220 nm. The bending radius is 3 μm which ensures a large enough quality factor or negligible loss due to bending. The mode propagation in the ring is shown in Fig. A-6(b). Two flux monitors are put at the input and output of the ring structure.

A.2.3 Mode Overlap Calculation

Normally, for mode overlap calculation of ring structure, the input flux monitor data is not used. On contrary, the output flux monitor data is used as the normalization due to a little mismatch between the mode calculated from mode solver and the input mode used for FDTD simulation. For most analysis inside of this thesis, the input flux monitor is seldom used. A calibration or low loss pass structure is used first for characterization, such as straight waveguide or ring structure. For ring structure, the bending Q assumed here is 1.07×10^6 as a reference. In Chapter 5, analysis on

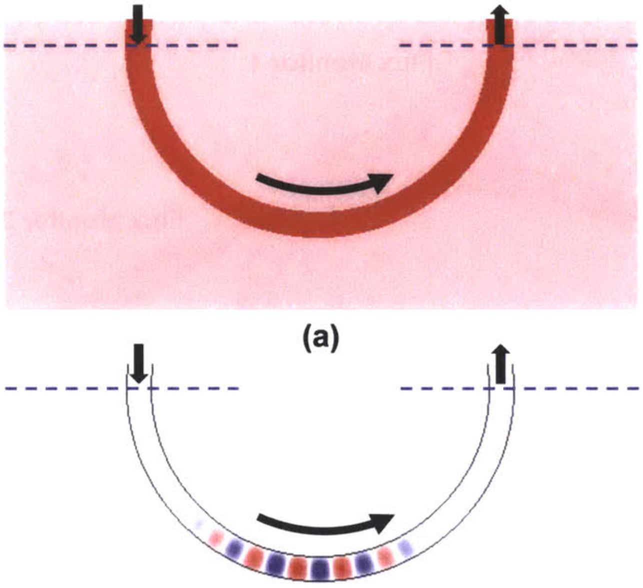

(a)

(b)

Figure A-6: (a) Simulation structure. The radius of the ring is 3μm. The red colored part is silicon while the light colored part is SiO_2. (b) Wave propagation in the ring. The top boundary is PML which absorbs the power incident on it.

adiabatic ring is performed where the normalization is based on perfect ring structure. The Q-factor of those structures can be extracted based on the normalized transmission values simulated.

A.3 Straight Waveguide to Ring Coupling

A.3.1 Waveguide to Ring Coupling Simulation Structure

The structure for FDTD simulation for waveguide-to-ring coupling is shown in Fig. A-7. The mode is sent into the straight waveguide and propagates along the waveguide. In the middle of the waveguide, the waveguide is coupled to a half micro-ring via evanescent wave coupling. Three flux monitors are set in the structure which are located at the beginning and end of the straight waveguide and the end of the half ring output. The bending of the ring will introduce some loss into the structure. But since the radius selected for the ring is 3 μm, the quality factor of the ring is large

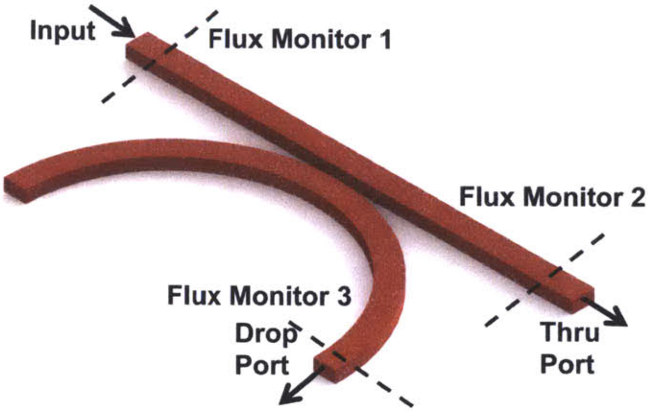

Figure A-7: Simulation structure of waveguide to ring coupling

enough that the bending loss becomes negligible. The boundary conditions are perfect matching layers (PMLs) which absorb the power incident on to the boundaries.

A.3.2 FDTD simulation

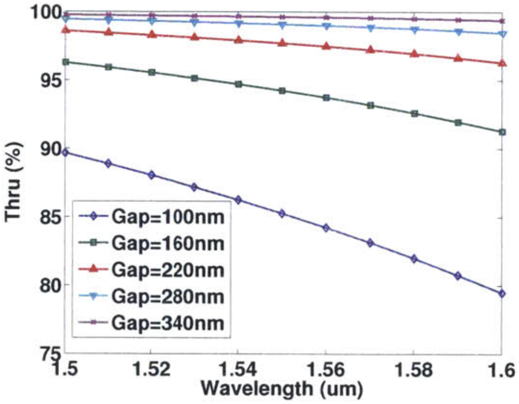

Figure A-8: 3D FDTD simulation results of the thru port response for different waveguide to ring gap sizes.

The data got from the flux monitor are then analyzed by the overlap calculation. Flux monitor 1 and 2 data are overlapped with straight waveguide mode while flux monitor 3 data are overlapped with bending mode of the ring structure. Fig. A-8 and A-9 shows the FDTD simulation results for waveguide to simple ring coupling for the thru port and drop port.

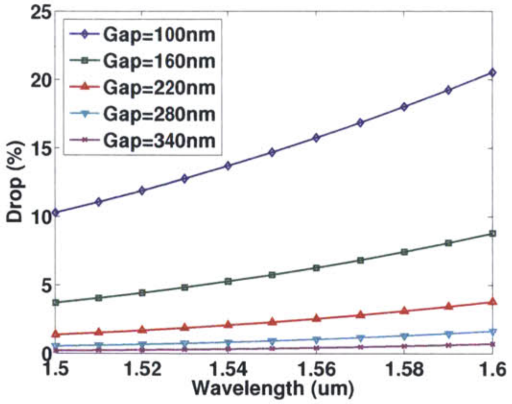

Figure A-9: 3D FDTD simulation results for the drop port response for different waveguide to ring gap sizes.

By picking a wavelength of 1550 nm, the coupling between the waveguide and ring and coupling induced loss can be extracted. Here, an exponential fitting for the data is used and the data match well with this model (shown in Fig. A-10). This can easily be explained in terms of coupled mode theory where the coupling coefficient in a coupled systems follows an exponential decay with respect to the distance between the components of the coupled system. The fitting equation used for is $10 \times \log_{10}(\text{Coupling(or Loss)}) = \text{P1} \times \text{Gap} + \text{P2}$. The fitting parameters for coupling are P1 = -0.0664/nm and P2 = -1.7418. The parameters for loss are P1 = -0.0675/nm and P2 = -27.6099.

A.3.3 Coupling Induced Phase Shift (CIPS)

Apart from the amplitude response from FDTD, there is another critical factor which matters to the resonator. The coupling between the waveguide to ring can induce a phase change to the normal propagation of the ring. From taylor expansion prospect, the resonance wavelength can be written as

$$\lambda(\phi) \approx \lambda(\phi_0) + (\phi - \phi_0)\frac{\partial \lambda}{\partial \phi}|_{\phi=\phi_0} \tag{A.2}$$

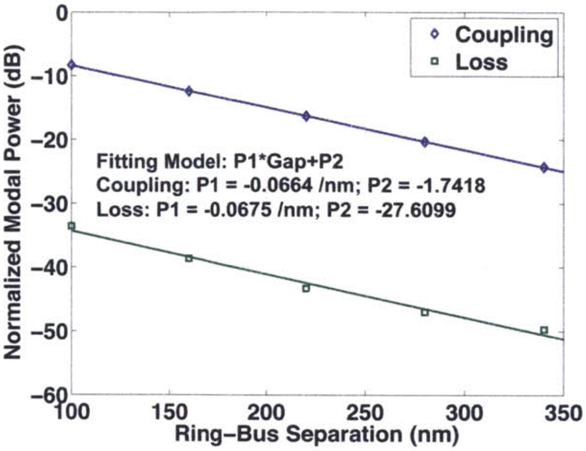

Figure A-10: The coupling strength and coupling loss from FDTD simulation. The dots are the simulation results and the solid lines are the exponential fitting of the results.

where ϕ represents the phase change when coupling between the waveguide and the ring exists while ϕ_0 is the value which stands for the phase change when no coupling is present. When ϕ is changed by 2π, which means another order of resonance, the resonant wavelength of the ring will be changed by a whole free spectral range (FSR). Thus, the resonant wavelength change can be approximated by

$$\Delta\lambda = \frac{\Delta\phi}{2\pi} FSR \tag{A.3}$$

The structure used for CIPS calculation and FDTD simulations are shown in Fig. A-11. By extracting the phase information of the mode propagating inside of the ring for the cases of with or without bus waveguide, the coupling induced phase shift can be calculated. The coupling induced phase shifts are plotted in Fig. A-12. Two kinds of CIPS are calculated. The Thru port response stands for the phase change of the mode propagating inside of the ring while the Drop port response stands for the phase change of the mode coupled to the straight waveguide. The Thru port is compared to normal propagation of the ring without bus waveguide. The Drop port is compared to the phase when the gap size is very large.

It is easy to go on calculating the coupling induced wavelength shift for this

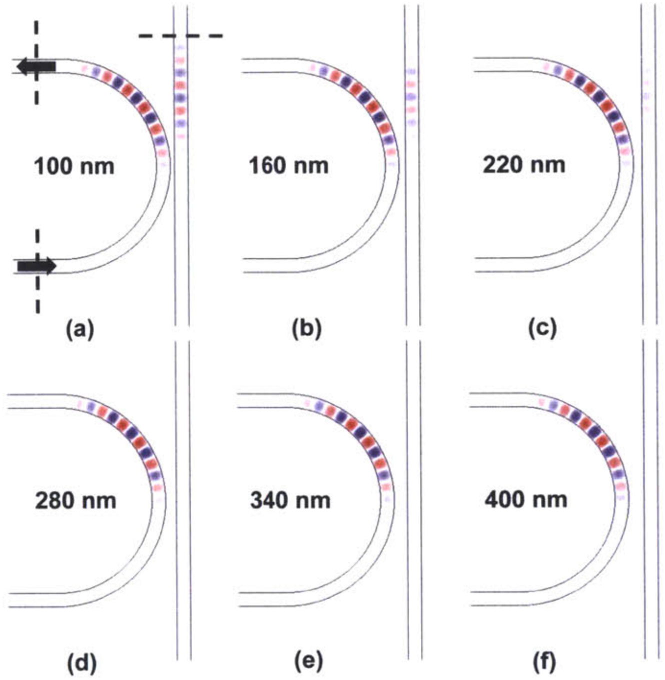

Figure A-11: FDTD simulation of a ring to waveguide coupled system.

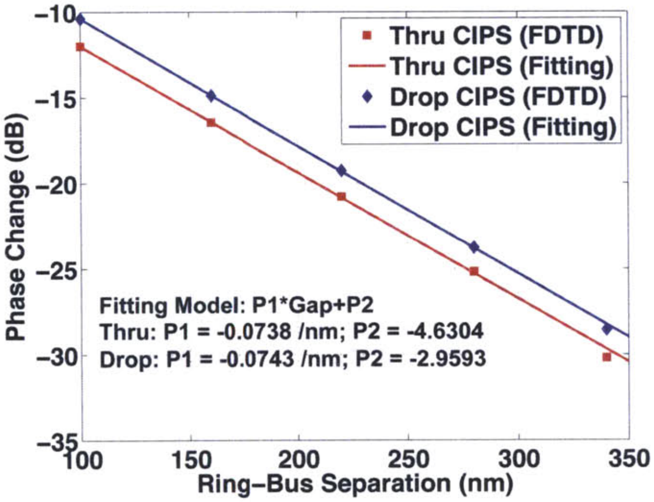

Figure A-12: Coupling induced phase shift FDTD simulation from a ring to waveguide coupling structure. The fitting parameters for Thru port are P1 = -0.0738/nm and P2 = -4.6304. The parameters for Drop port are P1 = -0.0743/nm and P2 = -2.9593. The wavelength used is 1550 nm.

situation. The FSR for a ring of 3μm radius and 0.4 μm width is 31.6 nm. In this sense, the coupling induced wavelength shift is displayed in Fig. A-13. Thus, the scale

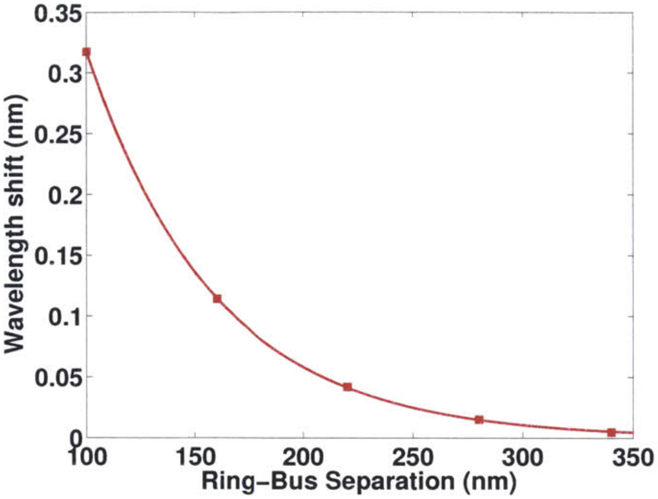

Figure A-13: Resonant wavelength shift due to ring and bus waveguide coupling for wavelength of 1550 nm.

of wavelength shift due to coupling is in the order of 0.1 nm.

A.4 Ring to Ring Coupling

A.4.1 Ring to Ring Coupling Simulation

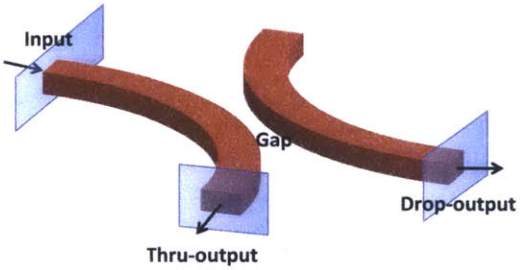

Figure A-14: Simulation structure of ring to ring coupling

The structure for micro-ring to micro-ring coupling simulation is shown in Fig. A-14. The input mode of the bending structure is sent in to the input port and two flux monitors are arrange at the thru-output port and drop-output port to measure the modes. The FDTD simulation for different ring to ring gap sizes are shown in

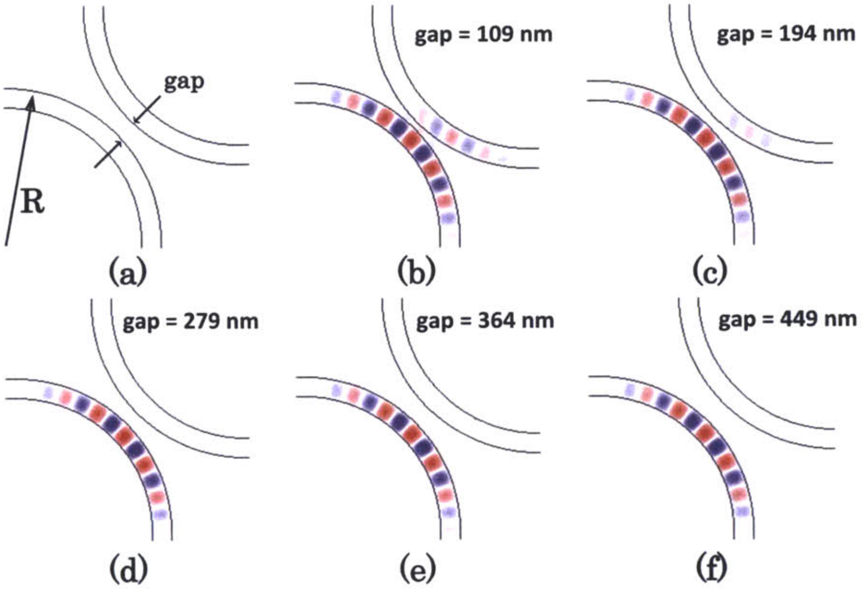

(a) (b) (c) (d) (e) (f)

Figure A-15: FDTD simulation figure of the ring to ring coupling for different gap values.

Fig. A-15.

A.4.2 Mode Overlap of Ring to Ring Coupling

By analyzing the mode overlap values of the ring-to-ring coupling, the couplings to the drop port and coupling induced losses are shown in Fig. A-16. The results are fitted with exponential model. The fitting parameters for coupling are P1 = -0.05543/nm and P2 = -3.204 and the parameters for loss are P1 = -0.0582/nm and P2 = -16.25. It shows a pretty linear curve which solidify the assumption that the coupling decreases exponentially with the gap between the waveguides. Compared with Fig. A-9 which is straight waveguide to ring coupling case, the coupling strength is similar and the coupling induced loss for ring-to-ring coupling case is relative higher than the waveguide-to-ring case.

Apart from that, the ring-to-ring CIPS (R-R) is plotted in the Fig. A-17 and the ring to straight waveguide CIPS (R-W) is also displayed in that figure as comparison. From the figure, it is clear that ring-to-ring CIPS is larger than the case for ring-

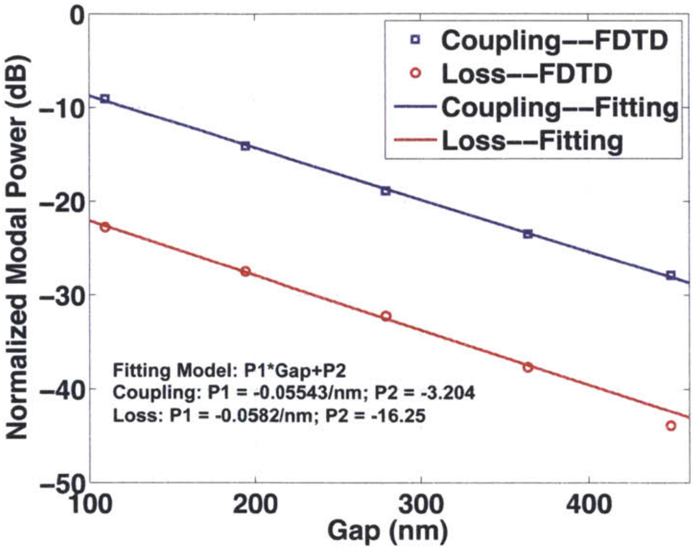

Figure A-16: Ring-to-ring coupling calculated from 3D FDTD simulation for wavelength 1.55 μm. The fitting model used is linear fitting.

to-waveguide for the same size gap and it has a relative small slope compared to ring-to-waveguide case.

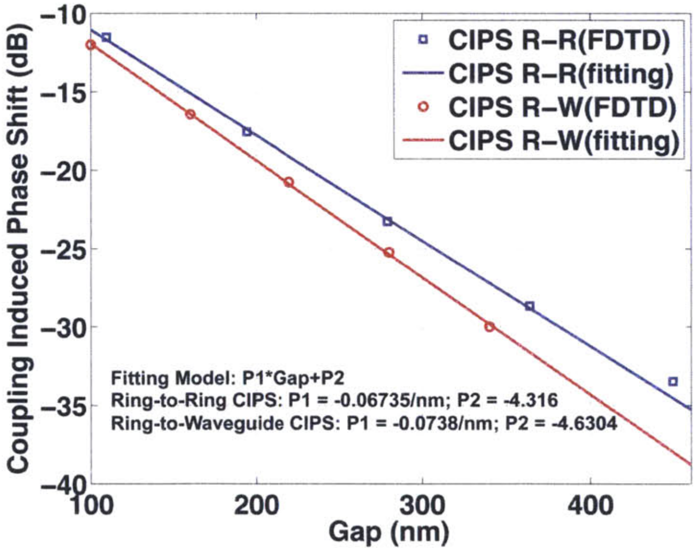

Figure A-17: Ring-to-ring CIPS and ring-to-waveguide CIPS comparison for wavelength of 1550 nm.

A.5 Summary

In this chapter, finite difference time domain (FDTD) method for photonic simulation is introduced and several examples on basic components FDTD simulations including straight waveguide propagation, waveguide-to-ring coupling, ring-to-waveguide coupling, and ring-to-ring coupling are analyzed. These examples can be used as a guidance for further simulations. By using these building blocks, complex structures can be easily built and simulated.

Appendix B

Microring Resonator Based Filter

For communication system, a high-quality filter plays a very important rule in maintaining the high quality of the signal in the channel. In this appendix, filter responses using the transfer matrix method are analyzed. The formalism of the method will be discussed in the first section. The model will further on be applied to different situations such as a notch filter with drop port and high order filters.

B.1 Formalism

As mentioned in ref. [68], the micro-ring resonator can be explained using time domain coupled mode equations. In this way, a lot of property of the resonator can be explained such as quality factor (Q), coupling strength from waveguide to ring, energy picture, power picture, mode order, group index picture of the ring resonator etc..

The basic filter structure is shown in Fig. B-1. Different from the resonant mode inside of grating structure or free space mirror structure, the resonant mode here is a traveling mode or so-called whispering-gallery mode. $A(t)$ denotes the traveling wave amplitude inside of the cavity. In this notation, $|A(t)|^2$ represents the power flowing through every cross-section of the cavity. Thus,

$$|a(t)|^2 = |A(t)|^2 \frac{2\pi R}{V_g} \qquad \text{(B.1)}$$

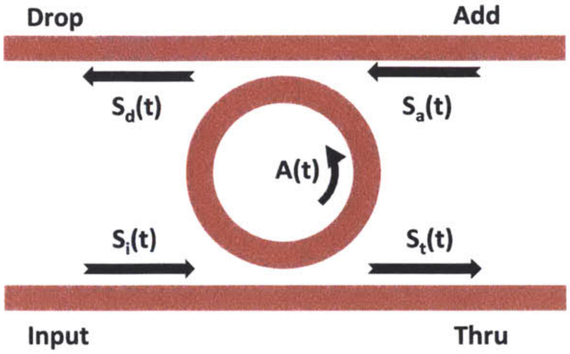

Figure B-1: The micro-ring structure for analysis.

stands for the energy inside the whole cavity where the R stands for the radius of the ring and V_g is the group index of the mode. The decay of the energy inside of the cavity consists of three part – intrinsic loss of the cavity, coupling to the bus waveguide and coupling to the drop waveguide. With improvement of the fabrication process, the intrinsic loss of the ring is becoming lower and lower. For normal application such as 50GHz or 100GHz bandwidth filter design, the intrinsic loss is already negligible compare to the coupling to outside waveguide. We can associate an decaying time to the loss process which is the time rate of the energy change, denoting it as τ_e, τ_d and τ_l separately for coupling to bus, coupling to drop and intrinsic loss inside of the cavity.

The ring is fed by the incident wave $S_i(t)$. Assuming the add port is zero, the time domain couple mode equation can be written as

$$\frac{\mathrm{d}a}{\mathrm{d}t} = (j\omega_0 - 1/\tau)a - j\mu S_i \tag{B.2}$$

$$S_t = S_i - j\mu a \tag{B.3}$$

The rate $1/\tau = 1/\tau_e + 1/\tau_d + 1/\tau_l$. The left problem is understand the mutual coupling coefficient μ. μ here is used to link the power picture and energy picture together. Thus, there should be a coefficient related to the structure to link μ to the coupling coefficient κ which is in the power picture.

To make the derivation easier, we start with exciting the resonator with initial energy $|a(0)|^2$ and removing the source $S_i(t)$ while assuming the coupling to the drop waveguide and loss in the cavity are negligible ($1/\tau_d = 0$ and $1/\tau_l = 0$). The complete picture will be discussed later.

Thus, the rate equation has the solution as

$$|a(t)|^2 = |a(0)|^2 \exp(\frac{2t}{\tau}) \tag{B.4}$$

$$|S(t)|^2 = \mu^2 |a(t)|^2 \tag{B.5}$$

The power coupling from waveguide to the ring (vise versa) is assume to be κ which can be calculated from FDTD simulation. Thus

$$|S(t)|^2 = \kappa^2 |A(t)|^2 = \kappa^2 \frac{V_g}{2\pi R} |a(t)|^2 \tag{B.6}$$

Combining equation B.5 and B.6 together, the relation of μ and κ can be shown as

$$\mu^2 = \kappa^2 \frac{V_g}{2\pi R} \tag{B.7}$$

Assuming the power conservation relation, in this scenario, the change of the energy ($\mathrm{d}|a(t)|^2/\mathrm{d}t$) inside of the cavity should equal to the power left from the thru port ($|S(t)|^2$). Thus the relation between μ, κ and τ is

$$\mu_e^2 = \kappa_e^2 \frac{V_g}{2\pi R} = \frac{2}{\tau_e} \tag{B.8}$$

Similar equation can be applied to the drop port.

$$\mu_d^2 = \kappa_d^2 \frac{V_g}{2\pi R} = \frac{2}{\tau_d} \tag{B.9}$$

B.2 Quality Factor

There are two common definitions of the Q factor of a resonator. One way is defined by 2π times the ratio of the stored energy to the energy dissipated per oscillation cycle. The other way is defined by the ratio of the resonance frequency ν_0 and the full width at half-maximum (FWHM) bandwidth of the cavity.

$$Q = \frac{\nu_0}{\delta\nu} \tag{B.10}$$

These two definitions are equivalent only in the limit of weakly damped resonator.

B.3 Transfer Matrix Method

Transfer matrix (T-matrix) is an useful method in calculating optical devices. The overall response of the system can be calculated by cascading the T-matrix of each component. Instead of calculating the response of structure in time domain such as Finite Difference Time Domain (FDTD) method, T-matrix calculates the response of the system in frequency domain. And the overall response of the structure in different frequencies can be calculated separately. This assumes no interference between different frequencies. If there exists frequency interferences such as laser structures, T-matrix is not suitable in doing the calculation.

In this section, I will talk about calculating micro-ring resonator response using T-matrix, covering the requirement for parameters, first order and second order filter designs. The example T-matrix code is attached in the last parts of this appendix.

Before doing designs using T-matrix, several properties such as reciprocity, power conservation, and time reversal condition need to be considered. Since the materials dealt in this thesis are silicon and SiO_2 which are all reciprocal materials, the reciprocity condition needs to be met. For waveguide to ring coupling, ring to ring coupling, the loss due to the coupling is relatively small compared to coupling number. Thus, the system can be approximated as a lossless system. Thus, the power conservation condition is also satisfied. For typical passive or heater based ring based filter, the optical mode will not be affected by the source such as current inside of the cavity. In that case, the time reversal condition is also satisfied. For a typical transfer matrix, the most important part is creating the matrix needed. For example, typical two-input two-output system will have a 2×2 matrix S linking input and output. The two inputs are a_1 and a_2 and two outputs are b_1 and b_2. Thus, the relation between them is

$$\begin{bmatrix} b_1 \\ b_2 \end{bmatrix} = S \cdot \begin{bmatrix} a_1 \\ a_2 \end{bmatrix} \tag{B.11}$$

$$S = \begin{bmatrix} S_{11} & S_{12} \\ S_{21} & S_{22} \end{bmatrix} \tag{B.12}$$

The three properties insert different conditions on the matrix S [69]. Reciprocity requires $S_{12} = S_{21}$. Power conservation requires $|S_{11}|^2 + |S_{21}|^2 = 1$, $|S_{22}|^2 + |S_{12}|^2 = 1$ and $S_{11}^* S_{12} + S_{21}^* S_{22} = 0$. Time reversal condition requires that $S^* = S^{-1}$.

With those conditions, the S matrix can be represented with two parameters, namely r and t which stand for reflection and transmission separately. And the matrix S can be written as

$$S = \begin{bmatrix} r & jt \\ jt & r \end{bmatrix} \tag{B.13}$$

To simulate the overall system of a micro-ring resonator with both thru port and drop port. The parameters required for the T-matrix are as follows: bus waveguide to ring coupling, ring propagation bending loss, free spectral range (FSR) of the ring, coupling induced phase shift (CIPS), resonant wavelength without bus waveguide, drop waveguide to ring coupling.

bus to ring coupling ($\|t_1\|^2$)	0.04
ring propagation loss (α)	8.175E-2/cm
FSR	31.6 nm
CIPS	0
resonant wavelength	1.562 μm
drop to ring coupling ($\|t_2\|^2$)	0.04
mode order	25

Table B.1: Typical parameters used for 3 μm silicon micro-ring resonator

A typical 3 μm micro-ring is used as an example for the demonstration. The parameters picked for a 3 μm ring is listed in the table B.1. The bus to ring coupling number is 0.04 and drop to ring coupling is also 0.04. For the ring propagation loss, two equations are used for extracting loss [67] number α

$$Q = \frac{\omega_0}{2\alpha V_g} \tag{B.14}$$

$$FSR = \frac{\lambda_0^2}{2\pi R n_g} \tag{B.15}$$

Where Q stands for quality factor of the resonator, V_g is the group velocity of light in the resonator, ω_0 stands for the angular frequency of the light, α is the loss per length number, n_g is the group index of the mode in the resonator which is linked to V_g by $V_g = c_0/n_g$ where c_0 is the speed of light in free space, λ_0 denotes the wavelength of the light and R is the outer radius of the ring.

Combining them together, the wave amplitude loss number is

$$\alpha = \frac{\lambda_0}{2Q \cdot FSR \cdot R} \tag{B.16}$$

Suppose $\lambda_0 = 1.55\mu$m, $FSR = 31.6$ nm (typical value for a 3μm silicon micro-ring and Q of 10^6, the α value will become 8.175E-2/cm. For now, I assume a zero coupling induced phase shift (CIPS).

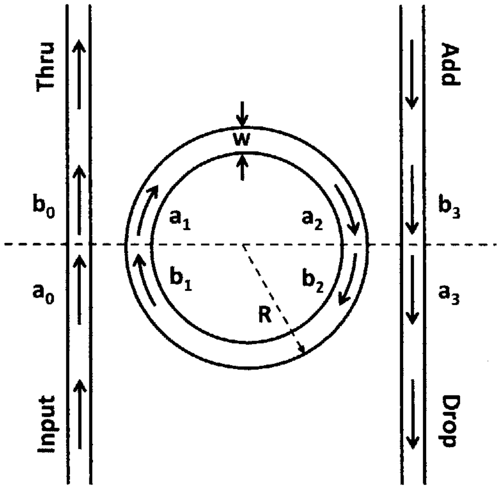

Figure B-2: Schematic of first order micro-ring filter. Thru represents through port while drop represents drop port. The labels on the figure represent the wave amplitude coefficients. The input for each stage is labelled as a while b is used for add port.

B.3.1 First Order Ring-Based Filter

The schematic for a first order micro-ring is shown in Fig. B-2. a_0, b_0, a_1, b_1, a_2, b_2, a_3, b_3 are marked on the figure. The relations between these variables are listed as follows:

$$\begin{bmatrix} b_0 \\ a_1 \end{bmatrix} = \begin{bmatrix} r_1 & jt_1 \\ jt_1 & r_1 \end{bmatrix} \begin{bmatrix} a_0 \\ b_1 \end{bmatrix} \tag{B.17}$$

$$\begin{bmatrix} b_2 \\ a_3 \end{bmatrix} = \begin{bmatrix} r_2 & jt_2 \\ jt_2 & r_2 \end{bmatrix} \begin{bmatrix} a_2 \\ b_3 \end{bmatrix} \tag{B.18}$$

$$\begin{bmatrix} a_2 \\ b_2 \end{bmatrix} = \begin{bmatrix} \exp(-j\phi) & 0 \\ 0 & \exp(j\phi) \end{bmatrix} \begin{bmatrix} a_1 \\ b_1 \end{bmatrix} \tag{B.19}$$

where r_1 and r_2 represent the reflection coefficients from the thru and drop ports while t_1 and t_2 represents the transmission coefficients from the thru and drop ports and $\phi = \beta_g L$ is the phase gained from the propagation. β_g is the group propagation constant which can be complex number and L is the propagation length of half ring. Since in most cases, the coupling loss is quite small that the coupling section can be thought as lossless, the relation between the coefficients $|r_i|^2 + |t_i|^2 = 1$, $i = 1, 2$ holds for most cases. The above equations can be rewritten in a compact way to be suitable for cascading as follows:

$$\begin{bmatrix} a_1 \\ b_1 \end{bmatrix} = \begin{bmatrix} jt_1 + j\frac{r_1^2}{t_1} & \frac{r_1}{jt_1} \\ -\frac{r_1}{jt_1} & \frac{1}{jt_1} \end{bmatrix} \begin{bmatrix} a_0 \\ b_0 \end{bmatrix} = M_{01} \begin{bmatrix} a_0 \\ b_0 \end{bmatrix} \tag{B.20}$$

$$\begin{bmatrix} a_2 \\ b_2 \end{bmatrix} = \begin{bmatrix} \exp(-j\phi) & 0 \\ 0 & \exp(j\phi) \end{bmatrix} \begin{bmatrix} a_1 \\ b_1 \end{bmatrix} = M_{12} \begin{bmatrix} a_1 \\ b_1 \end{bmatrix} \tag{B.21}$$

$$\begin{bmatrix} a_3 \\ b_3 \end{bmatrix} = \begin{bmatrix} jt_2 + j\frac{r_2^2}{t_2} & \frac{r_2}{jt_2} \\ -\frac{r_2}{jt_2} & \frac{1}{jt_2} \end{bmatrix} \begin{bmatrix} a_2 \\ b_2 \end{bmatrix} = M_{23} \begin{bmatrix} a_2 \\ b_2 \end{bmatrix} \tag{B.22}$$

Using this notation, the overall response can be easily calculated as

$$\begin{bmatrix} a_3 \\ b_3 \end{bmatrix} = M_{23} \cdot M_{12} \cdot M_{01} \begin{bmatrix} a_0 \\ b_0 \end{bmatrix} = \begin{bmatrix} G_{11} & G_{12} \\ G_{21} & G_{22} \end{bmatrix} \begin{bmatrix} a_0 \\ b_0 \end{bmatrix} = G \begin{bmatrix} a_0 \\ b_0 \end{bmatrix} \tag{B.23}$$

Normally, the add port b_3 is set to be zero since the power is sent in only through a_0. Thus,

$$\begin{aligned} a_3 &= G_{11}a_0 + G_{12}b_0 \\ 0 &= G_{21}a_0 + G_{22}b_0 \end{aligned} \tag{B.24}$$

By solving the equation, an overall expression linking a_3, a_0 and b_0 can be easily derived. The Thru port and Drop port responses are calculated as:

$$\begin{aligned} \text{Thru} &= |\tfrac{b_0}{a_0}|^2 &= |-\tfrac{G_{21}}{G_{22}}|^2 \\ \text{Drop} &= |\tfrac{a_3}{a_0}|^2 &= |G_{11} - \tfrac{G_{12}G_{21}}{G_{22}}|^2 \end{aligned} \tag{B.25}$$

Since the coupling coefficients and group propagation constants are dependent on wavelength, the overall T-Matrix G is wavelength dependent. By scanning the wavelength, the ring response to different wavelengths can be extracted. For optical filter, the bandwidth is less than 100GHz which corresponds to 0.8 nm. The coupling coefficient is not varying much within such small range of wavelength. In another word, the coupling coefficient can be regarded as constant within that range. For the parameters given in Table. B.1, the filter responses are shown in Fig. B-3. It has a 3dB bandwidth of 49.1GHz. The coupling induced frequency shift (CIFS) is not include in the calculation. Since it has only a small effect on the resonant wavelength, the overall effect is only an overall shift of the filter response. The MATLAB code for generating the first order filter response is attached in section B.4.1

B.3.2 Second Order Ring-Based Filter

With the formalism established before, second order filter can be easily implemented. Second filter design is a little bit different from the first order filter calculation. It includes the interaction between two rings. There are two ways on achieving second

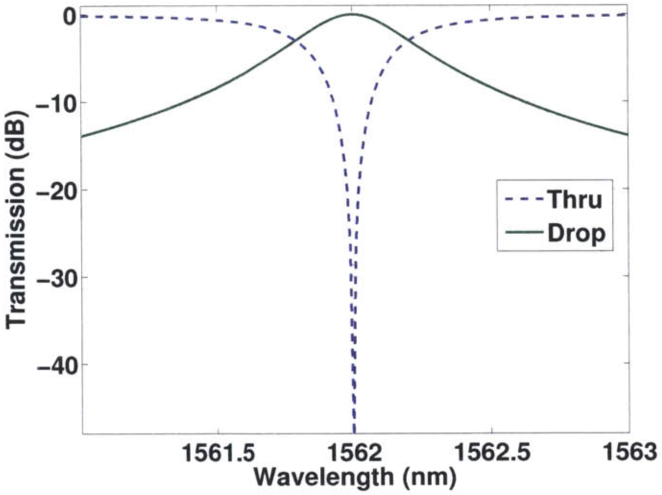

Figure B-3: First order filter with drop port using the parameters listed in Table B.1

order filter response, namely serial type configuration (shown in Fig. B-4(a)) and parallel type configuration (shown in Fig. B-4(b)). The serial type lacks the flexibility on tuning the mutual coupling between the rings. But for parallel case, it includes a $\pi/2$ phase shift in the path between two rings, which will need extra thermal tuning power for the structure.

Serial-Type Second Order Filter

The parameters used for the second order serial type filter are shown in Table B.2. The overall matrix G can be written as follows:

$$\begin{bmatrix} a_5 \\ b_5 \end{bmatrix} = M_{45} \cdot M_{34} \cdot M_{23} \cdot M_{12} \cdot M_{01} \begin{bmatrix} a_0 \\ b_0 \end{bmatrix} = \begin{bmatrix} G_{11} & G_{12} \\ G_{21} & G_{22} \end{bmatrix} \begin{bmatrix} a_0 \\ b_0 \end{bmatrix} = G \begin{bmatrix} a_0 \\ b_0 \end{bmatrix} \tag{B.26}$$

where

$$M_{01} = \begin{bmatrix} jt_1 + j\frac{r_1^2}{t_1} & \frac{r_1}{jt_1} \\ -\frac{r_1}{jt_1} & \frac{1}{jt_1} \end{bmatrix} \tag{B.27}$$

$$M_{12} = \begin{bmatrix} \exp(-j\phi) & 0 \\ 0 & \exp(j\phi) \end{bmatrix} \tag{B.28}$$

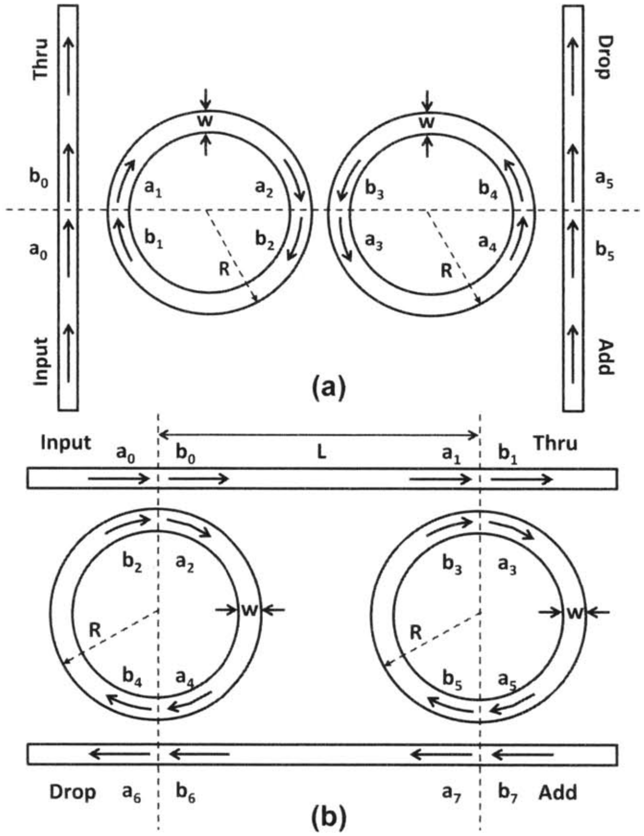

Figure B-4: Second order filter based on micro-ring resonator. (a) Two rings in serial. (b) Two rings in parallel.

$$M_{23} = \begin{bmatrix} jt_2 + j\frac{r_2^2}{t_2} & \frac{r_2}{jt_2} \\ -\frac{r_2}{jt_2} & \frac{1}{jt_2} \end{bmatrix} \tag{B.29}$$

$$M_{34} = \begin{bmatrix} \exp(-j\phi) & 0 \\ 0 & \exp(j\phi) \end{bmatrix} \tag{B.30}$$

$$M_{45} = \begin{bmatrix} jt_3 + j\frac{r_3^2}{t_3} & \frac{r_3}{jt_3} \\ -\frac{r_3}{jt_3} & \frac{1}{jt_3} \end{bmatrix} \tag{B.31}$$

This way, by assuming zero input of the Add port, the Thru port and Drop port

bus to ring coupling ($\|t_1\|^2$)	0.04
ring to ring coupling ($\|t_2\|^2$)	0.00045
ring propagation loss (α)	8.175E-2/cm
FSR	31.6 nm
CIPS	0
resonant wavelength	1.562 μm
drop to ring coupling ($\|t_3\|^2$)	0.04
mode order	25

Table B.2: Parameters for serial type second order ring-based filter.

can be similarly expressed as:

$$\begin{aligned} \text{Thru} &= |\tfrac{b_0}{a_0}|^2 &&= |-\tfrac{G_{21}}{G_{22}}|^2 \\ \text{Drop} &= |\tfrac{a_5}{a_0}|^2 &&= |G_{11} - \tfrac{G_{12}G_{21}}{G_{22}}|^2 \end{aligned} \qquad \text{(B.32)}$$

The responses of the second order filter using the parameters listed in Table B.2 are shown in Fig. B-5. It has a 3dB bandwidth of 36.8 GHz. It is noticed that the Drop port response is flatter than that of first order filter. Besides, power level outside of the passband is more suppressed which makes it easier to have denser channel distributions. The MATLAB code for generating the serial second order response is attached in section B.4.2.

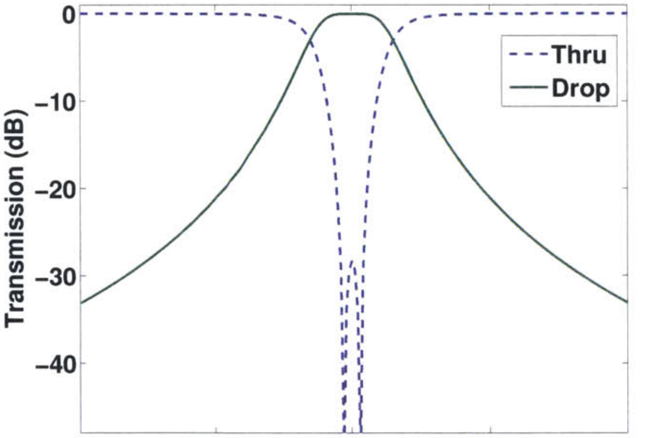

Figure B-5: Second order serial type ring-based filter using parameters listed in Table B.2.

Parallel-Type Second Order Filter

In the parallel-type second order filter, two rings are coupled to each other by a path of length L. For center wavelength of λ_0, the length L needs to satisfy relation as:

$$L = \frac{(m+1/2)\lambda_0}{2 \cdot n_{eff}} \tag{B.33}$$

where n_{eff} is the effective index of the waveguide for wavelength of λ_0 and m is an integer number.

In this way, for the center wavelength, b_0, a_1 and b_6, a_7 shown in Fig. B-4 are linked by a $\pi/2$ or $3\pi/2$ phase shifter. The relations between them are expressed as:

$$\begin{aligned} a_1 &= b_0 \cdot \exp(-jk(\lambda)L) \\ b_6 &= a_7 \cdot \exp(-jk(\lambda)L) \end{aligned} \tag{B.34}$$

where $k(\lambda)$ is the effective propagation constant for wavelength λ. For certain wavelength λ_0, $k(\lambda)$ can be expanded near it which gives:

$$k(\lambda) = k(\lambda_0) + (\frac{2\pi}{\lambda_0}\frac{\partial n_{eff}}{\partial \lambda}|_{\lambda=\lambda_0} - \frac{2\pi n_{eff}}{\lambda_0^2}) \cdot (\lambda - \lambda_0) \tag{B.35}$$

To simplify the calculation, assuming $\partial n_{eff}/\partial\lambda \ll n_{eff}/\lambda_0$, the equation is simplified to be:

$$k(\lambda) = k(\lambda_0) - \frac{2\pi n_{eff}}{\lambda_0^2} \cdot (\lambda - \lambda_0) \tag{B.36}$$

The n_{eff} for wavelength of 1.562 μm is 2.2158.

The relation for the two first order relation can be easily derived as:

$$\begin{bmatrix} a_6 \\ b_6 \end{bmatrix} = T \begin{bmatrix} a_0 \\ b_0 \end{bmatrix} \tag{B.37}$$

$$\begin{bmatrix} a_7 \\ b_7 \end{bmatrix} = S \begin{bmatrix} a_1 \\ b_1 \end{bmatrix} \tag{B.38}$$

Combining the phase relation shown in Eqn. B.34, the overall response can expressed as:

$$\begin{bmatrix} a_0 \\ a_6 \end{bmatrix} = M \cdot N \begin{bmatrix} b_1 \\ b_7 \end{bmatrix} = G \begin{bmatrix} b_1 \\ b_7 \end{bmatrix} \tag{B.39}$$

$$M = \begin{bmatrix} -\frac{T_{22}}{T_{21}} \exp(jkL) & \frac{\exp(-jkL)}{T_{21}} \\ (-\frac{T_{11}T_{22}}{T_{21}} + T_{12}) \exp(jkL) & \frac{T_{11}}{T_{21}} \exp(-jkL) \end{bmatrix} \tag{B.40}$$

$$N = \begin{bmatrix} -\frac{S_{22}}{S21} & \frac{1}{S_{21}} \\ (-\frac{S_{11}S_{22}}{S_{21}} + S_{12}) & \frac{S_{11}}{S_{21}} \end{bmatrix} \tag{B.41}$$

Thus, the Thru port and Drop port responses can be expressed as:

$$\begin{aligned} \text{Thru} &= |\tfrac{b_1}{a_0}|^2 & = |\tfrac{1}{G_{11}}|^2 \\ \text{Drop} &= |\tfrac{a_6}{a_0}|^2 & - |\tfrac{G_{21}}{G_{11}}|^2 \end{aligned} \tag{B.42}$$

The parameters used for the parallel second order filter are shown in Table B.3 and the overall responses of the parallel second order filter are shown in Fig. B-6. It also has the flat top feature for the Drop port which is different from the first order filter. The MATLAB code for generating the second order response is attached in section B.4.3.

bus to ring coupling ($\|t_1\|^2$)	0.028
ring propagation loss (α)	8.175E-2/cm
FSR	31.6 nm
CIPS	0
resonant wavelength	1.562 μm
drop to ring coupling ($\|t_3\|^2$)	0.04
mode order	25
L	8.9880 μm
n_{eff}	2.2158

Table B.3: Parameters for parallel type second order ring-based filter.

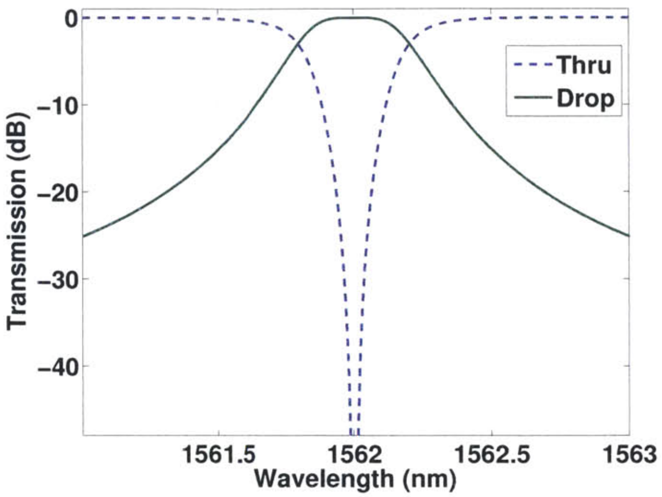

Figure B-6: Second order parallel type ring-based filter using parameters listed in Table B.3.

B.4 T-Matrix Code

B.4.1 First Order Filter with Drop Port

```
% % Transfer Matrix Code for Micro-Ring Filter with Drop Port

clear all; close all;

Coupling = 0.04; % bus to ring coupling

t1 = sqrt(Coupling);

t2 = t1;

r1 = sqrt(1-t1^2);

r2 = r1;

R = 3.0; % radius (um)

FSR = 31.6e-3; % free spectral range (um)

lam0 = 1.562; % resonant wavelength (um)

c0 = 299792458e6; % speed of light (um/s)


alpha = 8.175e-6; % imaginary part of propagation constant (/um)

jImg = -1i; % stands for j in expression
```

```
lamRange = (lam0-0.0010:0.00001:lam0+0.0010)'; % scan range of the wavelength (um)
phi = pi*(lamRange-lam0)/FSR-jImg*alpha*pi*R; % expression for Bg*L
Thru = zeros(size(lamRange));
Drop = zeros(size(lamRange));

for ii = 1:size(lamRange,1)
    M01 = [jImg*t1+jImg*r1^2/t1   r1/(jImg*t1);
           -r1/(jImg*t1)          1/(jImg*t1)];
    M12 = [exp(-jImg*phi(ii))         0;
           0                      exp(jImg*phi(ii))];
    M23 = [jImg*t2+jImg*r2^2/t2   r2/(jImg*t2);
           -r2/(jImg*t2)          1/(jImg*t2)];
    G = M23*M12*M01;
    Thru(ii) = abs(-G(2,1)/G(2,2))^2; % Thru Port response
    Drop(ii) = abs(G(1,1)-G(1,2)*G(2,1)/G(2,2))^2; % Drop Port response
end

X1 = [lamRange lamRange]*1000; % nm
Y1 = 10*log10([Thru Drop]);

% plot the figure
figure1 = figure('Color',[1 1 1]);
axes1 = axes('Parent',figure1,'FontWeight','bold','FontSize',20);
box(axes1,'on');
grid(axes1,'on');
hold(axes1,'all');

plot1 = plot(X1,Y1,'LineWidth',2);
set(plot1(1),'LineStyle','--');
```

```
legend('Thru','Drop');
xlim([lam0-0.0010 lam0+0.0010]*1000);
ylim([-48 1]);
xlabel('Wavelength (nm)');
ylabel('Transmission (dB)');

% % calculate 3dB bandwidth
for ii = 1:size(lamRange,1)
    if 10*log10(Thru(ii))< -3
        bandWidth = 2*(lam0-lamRange(ii))*1000; % bandwidth (nm)
        bandWidthF = 2*(c0/lamRange(ii)-c0/lam0)/1e9; % bandWidth (GHz)
        fprintf(1,'3dB bandWidth in wavelength is %.6f nm. \n',bandWidth);
        fprintf(1,'3dB bandWidth in frequency is %.6f GHz. \n',bandWidthF);
        break;
    end
end
```

B.4.2 Second Order Serial Type Filter with Drop Port

```
% % Transfer Matrix Code for Serial Type Second-Order
% % Micro-Ring Filter with Drop Port
clear all; close all;
wrCoupling = 0.04; % bus to ring coupling
rrCoupling = 0.00045; % ring to ring coupling
t1 = sqrt(wrCoupling);
r1 = sqrt(1-t1^2);
t2 = sqrt(rrCoupling);
r2 = sqrt(1-t2^2);
t3 = t1;
r3 = r1;
```

```
R = 3.0; % radius (um)
FSR = 31.6e-3; % free spectral range (um)
lam0 = 1.562; % resonant wavelength (um)
c0 = 299792458e6; % speed of light (um/s)

alpha = 8.175e-6; % imaginary part of propagation constant (/um)
jImg = -1i; % stands for j in expression

lamRange = (lam0-0.0010:0.00001:lam0+0.0010)'; % scan range of the wavelength (um)
phi = pi*(lamRange-lam0)/FSR-jImg*alpha*pi*R; % expression for Bg*L
Thru = zeros(size(lamRange));
Drop = zeros(size(lamRange));

for ii = 1:size(lamRange,1)
    M01 = [jImg*t1+jImg*r1^2/t1   r1/(jImg*t1);
           -r1/(jImg*t1)          1/(jImg*t1)];
    M12 = [exp(-jImg*phi(ii))         0;
           0                      exp(jImg*phi(ii))];
    M23 = [jImg*t2+jImg*r2^2/t2   r2/(jImg*t2);
           -r2/(jImg*t2)          1/(jImg*t2)];
    M34 = [exp(-jImg*phi(ii))         0;
           0                      exp(jImg*phi(ii))];
    M45 = [jImg*t3+jImg*r3^2/t3   r3/(jImg*t3);
           -r3/(jImg*t3)          1/(jImg*t3)];
    G = M45*M34*M23*M12*M01;
    Thru(ii) = abs(-G(2,1)/G(2,2))^2; % Thru Port response
    Drop(ii) = abs(G(1,1)-G(1,2)*G(2,1)/G(2,2))^2; % Drop Port response
end
```

```
X1 = [lamRange lamRange]*1000; % nm
Y1 = 10*log10([Thru Drop]);

% plot the figure
figure1 = figure('Color',[1 1 1]);
axes1 = axes('Parent',figure1,'FontWeight','bold','FontSize',20);
box(axes1,'on');
grid(axes1,'on');
hold(axes1,'all');

plot1 = plot(X1,Y1,'LineWidth',2);
set(plot1(1),'LineStyle','--');
legend('Thru','Drop');
xlim([lam0-0.0010 lam0+0.0010]*1000);
ylim([-48 1]);
xlabel('Wavelength (nm)');
ylabel('Transmission (dB)');

% % calculate 3dB bandwidth
for ii = 1:size(lamRange,1)
    if 10*log10(Thru(ii))< -3
        bandWidth = 2*(lam0-lamRange(ii))*1000; % bandwidth (nm)
        bandWidthF = 2*(c0/lamRange(ii)-c0/lam0)/1e9; % bandWidth (GHz)
        fprintf(1,'3dB bandWidth in wavelength is %.6f nm. \n',bandWidth);
        fprintf(1,'3dB bandWidth in frequency is %.6f GHz. \n',bandWidthF);
        break;
    end
end
```

B.4.3 Second Order Parallel Type Filter with Drop Port

```
% % Transfer Matrix Code for Parallel Type Second-Order
% % Micro-Ring Filter with Drop Port
clear all; close all;
wrCoupling = 0.028; % bus to ring coupling
t1 = sqrt(wrCoupling); % t1,r1 related to a0,a2
r1 = sqrt(1-t1^2);
t2 = t1; % t2,r2 related to a4,a6
r2 = r1;
t3 = t1; % t3,r3 related to a1,a3
r3 = r1;
t4 = t1; % t4,r4 related to a5,a7
r4 = r1;

R = 3.0; % radius (um)
FSR = 31.6e-3; % free spectral range (um)
lam0 = 1.562; % resonant wavelength (um)
c0 = 299792458e6; % speed of light (um/s)
neff = 2.2158; % effective index of rectangular waveguide

alpha = 8.175e-6; % imaginary part of propagation constant (/um)
jImg = -1i; % stands for j in expression

lamRange = (lam0-0.0010:0.00001:lam0+0.0010)'; % scan range of the wavelength (um)
phi = pi*(lamRange-lam0)/FSR-jImg*alpha*pi*R; % expression for Bg*L
L = (25+1/2)*lam0/(2*neff); % the length in between the ring (needs to be > 6 um);

Thru = zeros(size(lamRange));
Drop = zeros(size(lamRange));
```

```
for ii = 1:size(lamRange,1)
    k = 2*pi/lam0*neff-2*pi*neff/(lam0^2)*(lamRange(ii)-lam0); % propagation constant
    M02 = [jImg*t1+jImg*r1^2/t1   r1/(jImg*t1);
           -r1/(jImg*t1)          1/(jImg*t1)];
    M24 = [exp(-jImg*phi(ii))         0;
           0                      exp(jImg*phi(ii))];
    M46 = [jImg*t2+jImg*r2^2/t2   r2/(jImg*t2);
           -r2/(jImg*t2)          1/(jImg*t2)];
    T = M46*M24*M02;

    M13 = [jImg*t3+jImg*r3^2/t3   r3/(jImg*t3);
           -r3/(jImg*t3)          1/(jImg*t3)];
    M35 = [exp(-jImg*phi(ii))         0;
           0                      exp(jImg*phi(ii))];
    M57 = [jImg*t4+jImg*r4^2/t4   r4/(jImg*t4);
           -r4/(jImg*t4)          1/(jImg*t4)];
    S = M57*M35*M13;

    M = [-T(2,2)/T(2,1)*exp(jImg*k*L)                       exp(-jImg*k*L)/T(2,1);
         (-T(1,1)*T(2,2)/T(2,1)+T(1,2))*exp(jImg*k*L)       T(1,1)/T(2,1)*exp(-jImg*k
    N = [-S(2,2)/S(2,1)                 1/S(2,1);
         -S(1,1)*S(2,2)/S(2,1)+S(1,2)   S(1,1)/S(2,1)];
    G = M*N;
    Thru(ii) = abs(1/G(1,1))^2; % Thru Port response
    Drop(ii) = abs(G(2,1)/G(1,1))^2; % Drop Port response
end

X1 = [lamRange lamRange]*1000; % nm
Y1 = 10*log10([Thru Drop]); % dB
```

```
% plot the figure
figure1 = figure('Color',[1 1 1]);
axes1 = axes('Parent',figure1,'FontWeight','bold','FontSize',20);
box(axes1,'on');
grid(axes1,'on');
hold(axes1,'all');

plot1 = plot(X1,Y1,'LineWidth',2);
set(plot1(1),'LineStyle','--');
legend('Thru','Drop');
xlim([lam0-0.0010 lam0+0.0010]*1000);
ylim([-48 1]);
xlabel('Wavelength (nm)');
ylabel('Transmission (dB)');

% % calculate 3dB bandwidth
for ii = 1:size(lamRange,1)
    if 10*log10(Thru(ii))< -3
        bandWidth = 2*(lam0-lamRange(ii))*1000; % bandwidth (nm)
        bandWidthF = 2*(c0/lamRange(ii)-c0/lam0)/1e9; % bandWidth (GHz)
        fprintf(1,'3dB bandWidth in wavelength is %.6f nm. \n',bandWidth);
        fprintf(1,'3dB bandWidth in frequency is %.6f GHz. \n',bandWidthF);
        break;
    end
end
```

B.5 Summary

In this appendix, the theory on micro-ring resonator is illustrated. Both time domain coupled mode theory and T-matrix are covered. The designs techniques of common first order and second order filters based on micro-ring are analyzed. MATLAB implementations of the filter response are also attached.

Bibliography

[1] Aaron G Filler. The history, development and impact of computed imaging in neurological diagnosis and neurosurgery: Ct, mri, and dti. *Nature Procedings Web site.*, 2011.

[2] Wolfgang Drexler, Uwe Morgner, Ravi K Ghanta, Franz X Kärtner, Joel S Schuman, and James G Fujimoto. Ultrahigh-resolution ophthalmic optical coherence tomography. *Nature medicine*, 7(4):502–507, 2001.

[3] Emmanuel Desurvire, Jay R Simpson, and P C Becker. High-gain erbium-doped traveling-wave fiber amplifier. *Optics letters*, 12(11):888–890, 1987.

[4] Leonid G Kazovsky, Wei-Tao Shaw, David Gutierrez, Ning Cheng, and Shing-Wa Wong. Next-generation optical access networks. *Journal of lightwave technology*, 25(11):3428–3442, 2007.

[5] Gordon E Moore. Cramming more components onto integrated circuits. *Proceedings of the IEEE*, 86(1):82–85, 1998.

[6] Wm A Wulf and Sally A McKee. Hitting the memory wall: implications of the obvious. *ACM SIGARCH computer architecture news*, 23(1):20–24, 1995.

[7] Benjamin G Lee, Xiaogang Chen, Aleksandr Biberman, Xiaoping Liu, I-Wei Hsieh, Cheng-Yun Chou, Jerry I Dadap, Fengnian Xia, William M J Green, Lidija Sekaric, Yurii A Vlasov, Richard M Osgood, and Keren Bergman. Ultrahigh-Bandwidth Silicon Photonic Nanowire Waveguides for On-Chip Networks. *Photonics Technology Letters, IEEE*, 20(6):398–400, July 2008.

[8] Haisheng Rong, Ansheng Liu, Richard Jones, Oded Cohen, Dani Hak, Remus Nicolaescu, Alexander Fang, and Mario Paniccia. An all-silicon Raman laser. *Nature*, 433(7023):292–294, 2005.

[9] Haisheng Rong, Richard Jones, Ansheng Liu, Oded Cohen, Dani Hak, Alexander Fang, and Mario Paniccia. A continuous-wave Raman silicon laser. *Nature*, 433(7027):725–728, 2005.

[10] Rodolfo E Camacho-Aguilera, Yan Cai, Neil Patel, Jonathan T Bessette, Marco Romagnoli, Lionel C Kimerling, and Jurgen Michel. An electrically pumped germanium laser. *Optics Express*, 20(10):11316–11320, 2012.

[11] E H Bernhardi, HAGM van Wolferen, L Agazzi, MRH Khan, CGH Roeloffzen, K Wörhoff, M Pollnau, and R M De Ridder. Ultra-narrow-linewidth, single-frequency distributed feedback waveguide laser in Al_2O_3:Er^3+ on silicon. *Optics letters*, 35(14):2394–2396, 2010.

[12] Purnawirman, J Sun, T N Adam, G Leake, D Coolbaugh, J D B Bradley, E Shah Hosseini, and M R Watts. C- and L-band erbium-doped waveguide lasers with wafer-scale silicon nitride cavities. *Optics letters*, 38(11):1760, 2013.

[13] W A Zortman, D C Trotter, and M R Watts. Silicon photonics manufacturing. *Optics Express*, 18(23):23598–23607, October 2010.

[14] E Timurdogan. Automated Wavelength Recovery for Silicon Photonics. 2013.

[15] M R Watts, W A Zortman, D C Trotter, R W Young, and A L Lentine. Low-Voltage, Compact, Depletion-Mode, Silicon Mach–Zehnder Modulator. *IEEE Journal of Selected Topics in Quantum Electronics*, 16(1):159–164, 2010.

[16] Lei Bi, Juejun Hu, Peng Jiang, Dong Hun Kim, Gerald F Dionne, Lionel C Kimerling, and C A Ross. On-chip optical isolation in monolithically integrated non-reciprocal optical resonators. pages 1–5, November 2011.

[17] C T DeRose, D C Trotter, W A Zortman, A L Starbuck, M Fisher, M R Watts, and P S Davids. Ultra compact 45 GHz CMOS compatible Germanium waveguide photodiode with low dark current. *Optics Express*, 19(25):24897–24904, November 2011.

[18] Fengnian Xia, Lidija Sekaric, and Yurii Vlasov. Ultracompact optical buffers on a silicon chip. *Nature*, 1(1):65–71, January 2007.

[19] Milo A. Popovic, Tymon Barwicz, Marcus S. Dahlem, Fuwan Gan, Charles W. Holzwarth, Peter T. Rakich, Henry I. Smith, Erich P. Ippen, and Franz X. Krtner. Tunable, fourth-order silicon microring-resonator add-drop filters. In *Optical Communication (ECOC), 2007 33rd European Conference and Ehxibition of*, pages 1–2, 2007.

[20] M R Watts and H A Haus. Integrated mode-evolution-based polarization rotators. *Optics letters*, 30(2):138–140, 2005.

[21] M R Watts, H A Haus, and E P Ippen. Integrated mode-evolution-based polarization splitter. *Optics letters*, 30(9):967–969, 2005.

[22] Dazeng Feng, Ning-Ning Feng, Hong Liang, Wei Qian, Cheng-Chih Kung, Joan Fong, and Mehdi Asghari. Monolithic WDM Filter in Silicon-on-Insulator for Diplexer/Triplexer Application. 2008.

[23] Jared F Bauters, Martijn Heck, Daoxin Dai, Demis D John, Jonathon Barton, Daniel Blumenthal, and John E Bowers. High Extinction, Broadband, and Low Loss Planar Waveguide Polarizers. 2012.

[24] Zhe Xiao, Xianshu Luo, Peng Huei Lim, Patinharekandy Prabhathan, Samson T H Silalahi, Tsung-Yang Liow, Jing Zhang, and Feng Luan. Ultra-compact low loss polarization insensitive silicon waveguide splitter. *Optics Express*, 21(14):16331, 2013.

[25] M R Watts, W A Zortman, D C Trotter, R W Young, and A L Lentine. Vertical junction silicon microdisk modulators and switches. *Optics Express*, 19(22):21989–22003, October 2011.

[26] M A Popović, T Barwicz, M R Watts, P T Rakich, L Socci, E P Ippen, F X Kärtner, and H I Smith. Multistage high-order microring-resonator add-drop filters. *Optics letters*, 31(17):2571–2573, July 2006.

[27] L Chen, C R Doerr, and Y K Chen. Compact polarization rotator on silicon for polarization-diversified circuits. *Optics letters*, 36(4):469–471, 2011.

[28] Huijuan Zhang, Suchandrima Das, Ying Huang, Chao Li, Shiyi Chen, Haifeng Zhou, Mingbin Yu, Patrick Guo-Qiang Lo, and John TL Thong. Efficient and broadband polarization rotator using horizontal slot waveguide for silicon photonics. *Applied Physics Letters*, 101(2):021105–021105–4, 2012.

[29] N N Feng, R Sun, J Michel, and L C Kimerling. Low-loss compact-size slotted waveguide polarization rotator and transformer. *Optics letters*, 32(15):2131–2133, 2007.

[30] L Liu, Y Ding, K Yvind, and J M Hvam. Efficient and compact TE–TM polarization converter built on silicon-on-insulator platform with a simple fabrication process. *Optics letters*, 36(7):1059–1061, 2011.

[31] Yang Yue, Lin Zhang, Muping Song, Raymond G Beausoleil, and Alan E Willner. Higher-order-mode assisted silicon-on-insulator 90 degree polarization rotator. *Optics Express*, 17(23):20694–20699, 2009.

[32] Hiroshi Fukuda, Koji Yamada, Tai Tsuchizawa, Toshifumi Watanabe, Hiroyuki Shinojima, and Sei-ichi Itabashi. Silicon photonic circuit with polarization diversity. *Optics Express*, 16(7):4872–4880, 2008.

[33] Diedrik Vermeulen, Shankar Selvaraja, Peter Verheyen, Philippe Absil, Wim Bogaerts, Dries Van Thourhout, and Gunther Roelkens. Silicon-on-insulator polarization rotator based on a symmetry breaking silicon overlay. *Photonics Technology Letters, IEEE*, 24(6):482–484, 2012.

[34] Yunhong Ding, Haiyan Ou, C Optical Fiber Communication Conference Peucheret, Exposition, and the National Fiber Optic Engineers Conference OFC/NFOEC 2013. Wide-band polarization splitter and rotator with large fabrication tolerance and simple fabrication process. *Optics letters*, 38:1227–1230, 2013.

[35] L Liu, Y Ding, K Yvind, and J M Hvam. Silicon-on-insulator polarization splitting and rotating device for polarization diversity circuits. *Optics Express*, 19(13):12646–12651, 2011.

[36] Wesley D Sacher, Tymon Barwicz, and Joyce K S Poon. Silicon-on-Insulator Polarization Splitter-Rotator Based on TM0-TE1 Mode Conversion in a Bi-level Taper. *CLEO*, pages 1–2, January 2013.

[37] D Dai and J E Bowers. Novel concept for ultracompact polarization splitter-rotator based on silicon nanowires. *Optics Express*, 19(11):10940–10949, May 2011.

[38] Yunhong Ding, Liu Liu, Christophe Peucheret, and Haiyan Ou. Fabrication tolerant polarization splitter and rotator based on a tapered directional coupler. *Optics Express*, 20(18):20021–20027, August 2012.

[39] Tymon Barwicz, Michael R Watts, Miloš A Popović, Peter T Rakich, Luciano Socci, Franz X Kärtner, Erich P Ippen, and Henry I Smith. Polarization-transparent microphotonic devices in the strong confinement limit. *Nature Photonics*, 1(1):57–60, January 2007.

[40] V R Almeida, Q Xu, C A Barrios, and M Lipson. Guiding and confining light in void nanostructure. *Optics letters*, 29(11):1209–1211, 2004.

[41] Mehdi Asghari and Ashok V Krishnamoorthy. Silicon photonics: Energy-efficient communication. *Nature Photonics*, 5:268–270, May 2011.

[42] Shekhar Borkar and Andrew A Chien. The future of microprocessors. *Communications of the ACM*, 54(5):67, May 2011.

[43] J Wang, D Liang, Y Tang, D Dai, and J E Bowers. Realization of an ultra-short silicon polarization beam splitter with an asymmetrical bent directional coupler. *Optics letters*, 38:4–6, 2013.

[44] Jian Wang and Daoxin Dai. Ultra-small silicon polarization beam splitter based on cascaded asymmetry directional couplers. *in Optical Fiber Communication Conference/National Fiber Optic Engineers Conference 2013, OSA Technical Digest (online) (Optical Society of America, 2013), paper OTh4I.1*, 2013.

[45] Xianyu Ao, Liu Liu, Lech Wosinski, and Sailing He. Polarization beam splitter based on a two-dimensional photonic crystal of pillar type. *Applied Physics Letters*, 89(17):171115, 2006.

[46] J Feng and Z Zhou. Polarization beam splitter using a binary blazed grating coupler. *Optics letters*, 32(12):1662–1664, 2007.

[47] Winnie N Ye, Dan-Xia Xu, Siegfried Janz, Philip Waldron, Pavel Cheben, and N Garry Tarr. Passive broadband silicon-on-insulator polarization splitter. *Optics letters*, 32(11):1492–1494, 2007.

[48] Po Dong, Chongjin Xie, Long Chen, Larry L Buhl, and Young-Kai Chen. 112-Gb/s monolithic PDM-QPSK modulator in silicon. *Optics Express*, 20:B624–B629, 2012.

[49] Xing-Can Yao, Tian-Xiong Wang, Hao-Ze Chen, Wei-Bo Gao, Austin G Fowler, Robert Raussendorf, Zeng-Bing Chen, Nai-Le Liu, Chao-Yang Lu, You-Jin Deng, Yu-Ao Chen, and Jian-Wei Pan. Experimental demonstration of topological error correction. *Nature*, 482(7386):489–494, April 2013.

[50] S Slussarenko, V D'Ambrosio, B Piccirillo, L Marrucci, and E Santamato. The Polarizing Sagnac Interferometer: a tool for light orbital angular momentum sorting and spin-orbit photon processing. *Optics Express*, 18(26):27205–27216, October 2010.

[51] Shengmei Zheng, Hui Chen, and Andrew W Poon. Microring-resonator cross-connect filters in silicon nitride: rib waveguide dimensions dependence. *Selected Topics in Quantum Electronics, IEEE Journal of*, 12(6):1380–1387, 2006.

[52] A V Tsarev. Efficient silicon wire waveguide crossing with negligible loss and crosstalk. *Optics Express*, 19(15):13732–13737, 2011.

[53] Y Hatakeyama, T Hanai, S Suzuki, and Y Kokubun. Loss-Less Multilevel Crossing of Busline Waveguide in Vertically Coupled Microring Resonator Filter. *Photonics Technology Letters, IEEE*, 16(2):473–475, February 2004.

[54] P Sanchis, P Villalba, F Cuesta, A Håkansson, A Griol, J V Galán, A Brimont, and J Martí. Highly efficient crossing structure for silicon-on-insulator waveguides. *Optics letters*, 34(18):2760–2762, 2009.

[55] W Bogaerts, P Dumon, D V Thourhout, and R Baets. Low-loss, low-cross-talk crossings for silicon-on-insulator nanophotonic waveguides. *Optics letters*, 32(19):2801–2803, September 2007.

[56] Tarek A Ramadan, Robert Scarmozzino, and Richard M Osgood. Adiabatic couplers: design rules and optimization. *Journal of lightwave technology*, 16(2):277, 1998.

[57] Massimo Olivero. UV-written integrated optical 1xN splitters. *Optics Express*, 14:162–170, 2006.

[58] S H Tao, Q Fang, J F Song, M B Yu, G Q Lo, and D L Kwong. Cascade wide-angle Y-junction 1 x 16 optical power splitter based on silicon wire waveguides on silicon-on-insulator. *Opt. Express*, 16(26):21456–21461, October 2008.

[59] Amir Hosseini, David N Kwong, Yang Zhang, Harish Subbaraman, Xiaochuan Xu, and Ray T Chen. 1? N Multimode interference beam splitter design techniques for on-chip optical interconnections. *Selected Topics in Quantum Electronics, IEEE Journal of*, 17(3):510–515, 2011.

[60] M R Watts, J Sun, C DeRose, and D C Trotter. Adiabatic thermo-optic Mach–Zehnder switch. *Optics letters*, 38:733–735, 2013.

[61] D Spencer, Daoxin Dai, Yongbo Tang, M Heck, and J Bowers. Realization of a Novel 1? N Power Splitter with Uniformly Excited Ports. *Photonics Technology Letters, IEEE*, 25:36–39, 2013.

[62] Daoxin Dai and Sailing He. Proposal of a Coupled-Microring-Based Wavelength-Selective 1xN Power Splitter. *Photonics Technology Letters, IEEE*, 21(21):1630–1632, 2009.

[63] A Biberman, E Timurdogan, M R Watts, W A Zortman, and D C Trotter. Adiabatic microring modulators. *Optics Express*, 20(28):29223–29236, 2012.

[64] M R Watts. Adiabatic microring resonators. *Optics letters*, 35(19):3231–3233, September 2010.

[65] Aleksandr Biberman, Michael J Shaw, Erman Timurdogan, Jeremy B Wright, and Michael R Watts. Ultralow-loss silicon ring resonators. *Optics letters*, 37:4236–4238, October 2012.

[66] K. Worhoff, J.D.B. Bradley, Feridun Ay, D. Geskus, T.P. Blauwendraat, and M. Pollnau. Reliable low-cost fabrication of low-loss al_2o_3:er^{3+} waveguides with 5.4-db optical gain. *Quantum Electronics, IEEE Journal of*, 45(5):454–461, 2009.

[67] M R Watts. Polarization independent microphotonic circuits. 2005.

[68] B E Little, S T Chu, H A Haus, J Foresi, and J P Laine. Microring resonator channel dropping filters. *Lightwave Technology, Journal of*, 15(6):998–1005, 1997.

[69] Hermann A Haus. *Waves and fields in optoelectronics*. Prentice Hall Ptr, 1984.